UC Berkeley
UC Berkeley Electronic Theses and Dissertations

Title
Cavity Optomechanics in the Quantum Regime

Permalink
https://escholarship.org/uc/item/9jk7t3qw

Author
Botter, Thierry Claude Marc

Publication Date
2013

Peer reviewed|Thesis/dissertation

Cavity Optomechanics in the Quantum Regime

by

Thierry Claude Marc Botter

A dissertation submitted in partial satisfaction of the

requirements for the degree of

Doctor of Philosophy

in

Physics

in the

Graduate Division

of the

University of California, Berkeley

Committee in charge:

Professor Dan M. Stamper-Kurn, Chair
Professor Holger Müller
Professor Ming Wu

Spring 2013

Cavity Optomechanics in the Quantum Regime

Copyright 2013

by

Thierry Claude Marc Botter

Abstract

Cavity Optomechanics in the Quantum Regime

by

Thierry Claude Marc Botter

Doctor of Philosophy in Physics

University of California, Berkeley

Professor Dan M. Stamper-Kurn, Chair

An exciting scientific goal, common to many fields of research, is the development of ever-larger physical systems operating in the quantum regime. Relevant to this dissertation is the objective of preparing and observing a mechanical object in its motional quantum ground state. In order to sense the object's zero-point motion, the probe itself must have quantum-limited sensitivity. Cavity optomechanics, the interactions between light and a mechanical object inside an optical cavity, provides an elegant means to achieve the quantum regime. In this dissertation, I provide context to the successful cavity-based optical detection of the quantum-ground-state motion of atoms-based mechanical elements; mechanical elements, consisting of the collective center-of-mass (CM) motion of ultracold atomic ensembles and prepared inside a high-finesse Fabry-Pérot cavity, were dispersively probed with an average intracavity photon number as small as 0.1. I first show that cavity optomechanics emerges from the theory of cavity quantum electrodynamics when one takes into account the CM motion of one or many atoms within the cavity, and provide a simple theoretical framework to model optomechanical interactions. I then outline details regarding the apparatus and the experimental methods employed, highlighting certain fundamental aspects of optical detection along the way. Finally, I describe background information, both theoretical and experimental, to two published results on quantum cavity optomechanics that form the backbone of this dissertation. The first publication shows the observation of zero-point collective motion of several thousand atoms and quantum-limited measurement backaction on that observed motion. The second publication demonstrates that an array of near-ground-state collective atomic oscillators can be simultaneously prepared and probed, and that the motional state of one oscillator can be selectively addressed while preserving the near-zero-point motion of neighboring oscillators.

To the two grandparents I lost during my doctoral studies:

Fernande Bergheaud, André Manseau

Contents

List of Figures

List of Tables

Acknowledgments

Many people have positively impacted my experience as a doctoral student, both in the laboratory and outside of work. To these people, I offer you my sincere thanks.

Thank you, first of all, to my advisor, Dan Stamper-Kurn, for giving me the opportunity to join his talented research team and develop my scientific skill sets, and for his guidance along the way. Dan's scientific passion, his ability to identify important near-term objectives and his constantly accurate understanding of the science at play has allowed our cavity optomechanics team to achieve great success.

Thank you, secondly, to Tom Purdy. Tom was a fourth-year graduate student on the cavity optomechanics experiment when I joined the Stamper-Kurn group. He is arguably the person that most influenced my first three years at Berkeley. Not only did he provide me with much needed in-lab guidance, his experimental resourcefulness, his ability to frame in simple terms complicated physical processes and his relentless work ethic made him a role model for the latter half of my graduate studies. He and Dan Brooks also deserve thanks for putting together the core of the experimental apparatus before I joined the Stamper-Kurn group.

My most successful scientific years involved important contributions from two fellow group members, Nathan Brahms and Dan Brooks, to whom I give thanks. Having a trio of experienced group members helped quickly overcome hurdles during challenging experiments, and promote our apparatus to a leading contributor in cavity optomechanics. These successful experimental undertakings were also achieved with the aid of Sydney Schreppler, at the time the newest member of the Stamper-Kurn cavity optomechanics crew. I thank Sydney for her valuable participation to long, arduous data-taking sessions, and her contributions to the data analyses.

Through meetings, discussions and presentations, the Stamper-Kurn group at large also had an impact on my scientific development. For that, I thank Kater Murch, Mukund Vengalattore, Anton Öttl, Enrico Voigt, Zhao-Yuan Ma, André Wenz, Friedhelm Serwane, Jennie Guzman, Gyu-boong Jo, Claire Thomas, Tom Barter, Sean Lourette, and two group members that started the physics graduate program with me: Ed Marti and Ryan Olf.

Many friends have helped balance my work life with some fun times and good laughs, all of whom I thank. My thoughts go out to four fellow physics graduate students in particular who have been close friends since my first day at Berkeley: Steve Anton, Jon Blazek, Jonas Kjäll, and Sebastian ("Seabass") Wickenburg. Sports played a big role in keeping me leveled, and for that I wish to acknowledge the two organized sports teams I played with most while at Berkeley: Field Theory (the physics department's intramural soccer team) and Mavericks (men's hockey team).

Lastly, I would like to thank my relatives for their love and support throughout my years at Berkeley, in particular my mother, Francine Manseau, my sister, Sandrine Botter, and my grandparents, André Manseau, Rita Glazer, René Botter, and Fernande Bergheaud.

Chapter 1

Introduction

1.1 The history of optomechanics

Optomechanics broadly refers to interactions between light and a moving object. It stems from the idea that light can exert a force on a material object, an idea first postulated by Kepler in 1619 who believed that comets' tails were caused by the outward pressure of sunlight. Light-induced force was placed on firm theoretical ground in the 1870s by both Maxwell and Bartoli, based on electromagnetic theory and on the Second Law of Thermodynamics, respectively, and was experimentally demonstrated for the first time in 1901 [1, 2]. Over half a century later, a seminal investigation found that light-induced pressure could alter the mechanical properties of a moving object. This astonishing result paved the way for what is today a dynamic field of experimental physics, with important implications for both fundamental and applied science. In this section, I provide a brief overview of the recent history of optomechanics, thereby setting the context for the work described in this dissertation. My take on the evolution of optomechanics is, of course, not exhaustive; only a fraction of the panoply of key research works is presented.

In 1967, at the height of the cold war, Vladimir Braginsky and Anatolii Manukin co-authored a paper on the action of light reflecting off a harmonically bound mirror [3]. Their results indicated that the momentum imparted by the reflection of photons on a moveable mirror could alter that mirror's mechanical properties. In particular, when the moveable mirror was integrated as part of a Fabry-Pérot cavity, its motion could be damped or amplified by tuning the inserted light's frequency to the red or to the blue, respectively, of cavity resonance. Three years later, the duo experimentally verified this electromagnetically induced mechanical damping and amplification in an ultra-high frequency (UHF) resonator of quality factor $Q \sim$20,000 [4], nearly a hundred times smaller Q than the best UHF resonators today.

This idea of cavity optomechanics received much attention through the 1970s and early 1980s as it applied to the then novel idea of detecting gravitational waves us-
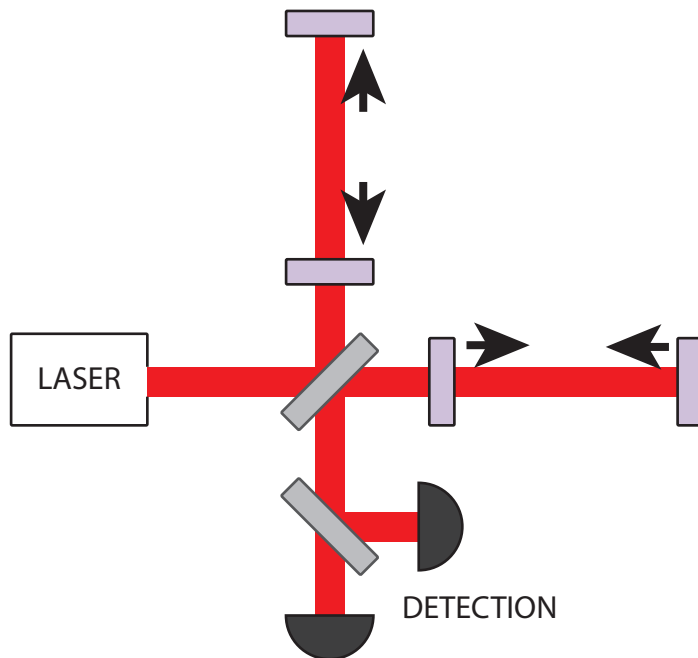
Figure 1.1: Schematic of a gravitational wave detector. Arrows highlight the differential impact of a passing gravitational waves. Interferometer arms typically range from hundreds of meters to kilometers.

ing Michelson-type laser interferometers. Gravity waves passing through the Earth would push apart the mirrors in one interferometer arm, while bringing the mirrors in the orthogonal interferometer arm closer together [5], thereby producing a differential phase shift that could be detected on the interferometer's recombined optical signal (Fig.1.1). This new scheme launched extensive studies of the quantum limits in cavity-optomechanics-based measurements. Quantum mechanics dictates that conjugate quadratures, such as position and momentum, cannot be simultaneously known arbitrarily precisely; their respective uncertainties are bounded by the Heisenberg uncertainty relation, leading to a base measurement limit known as the "standard quantum limit" (SQL) [6, 7]. Different ideas were proposed to surpass the SQL. The first idea, proposed and coined by Braginsky [6], centered on quantum nondemolition measurements (QND): if one could engineer a method to projectively measure one quadrature, say the moving mirror's position, without impacting its evolution, *i.e.* by having the measurement operation commute with the freely moving mirror's hamiltonian, then that quadrature could be known with arbitrary precision by repeating the measurement an infinite number of times. One example is the stroboscopic measurement of the mirror's position every half cycles of motion (*i.e.* every time the mirror crosses the position axis in its phase-space trajectory). The simple premise of QND detection was extensively studied by, among others, Kip Thorne [8], Vladimir
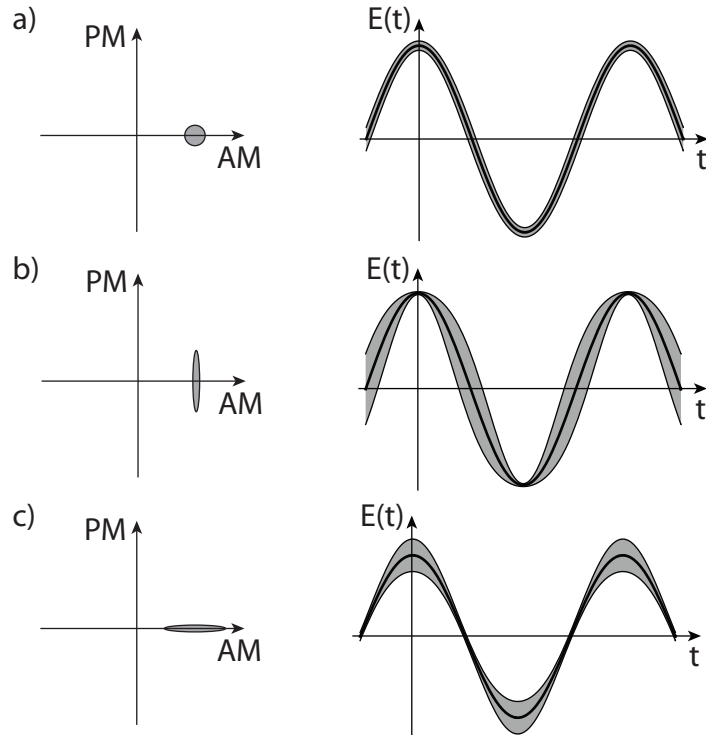
Figure 1.2: Representation of a coherent (a), amplitude squeezed (b), and phase squeezed (c) state of light. The left column shows the quantum uncertainty distribution between amplitude (AM) and phase (PM) quadratures of each state of light at time t=0. The right column shows the time-dependence of each state of light's electric field, with the gray shaded area representing the quantum uncertainty.

Braginsky [9], William Unruh [10] and Carlton Caves [11]. In 1981, Carlton Caves proposed an alternative method to surpass the SQL when measuring the differential displacement of mirrors in the two arms of an interferometer, $\Delta z = z_1 - z_2$ [12]. By injecting squeezed light, that is light with an unevenly shared uncertainty between its conjugate amplitude and phase quadratures (Fig. 1.2), both the *backaction* of the light on the motion of the harmonically bound mirrors and the random fluctuations in the arrival time of photons could be reduced, yielding measurement uncertainties below the SQL. Thanks to wide-spread scientific enthusiasm, as exemplified by these quantum investigations, laser-based interferometers became the norm for attempting to detect gravitational waves, surpassing the widely popular Weber bar [13]. Today, three large-scale laser-based gravitational wave detectors, with interferometric arms spanning hundreds of meters to a few kilometers, are in operation around the world: LIGO, GEO 600, and VIRGO.

Throughout the 1980s, optomechanics became relevant to many fields of physics, but took on different, specialized forms in each area of research. In optical physics,
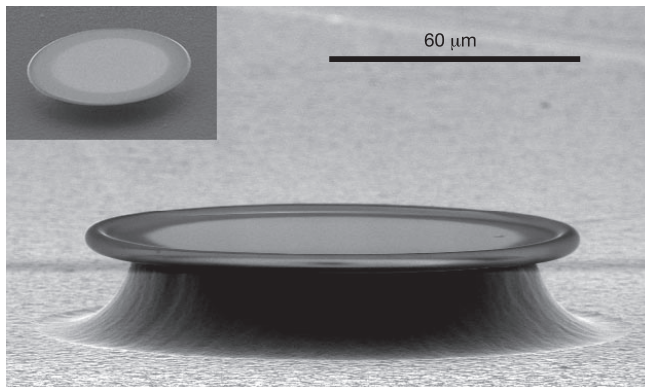
Figure 1.3: Scanning electron micrograph of the first ultra-high-Q silica toroidal microcavity, produced by the group of Prof. Kerry Vahala in 2003. Image taken from Ref.[21].

table-top experiments derived from the idea of applying cavity optomechanics towards gravitational wave detectors were designed. They produced the first observation of radiation-pressure-induced mirror confinements and optical bistability in a Fabry-Pérot cavity [14]. In atomic physics, the interaction of light with the mechanical degree of freedom of atoms led to the first experimental realizations of laser-based deceleration of atoms [15], optical molasses [16] and the accidental discovery of polarization-gradient cooling (also known as Sisyphus cooling) [17]. The use of light to cool and trap atoms evolved independently of Braginsky and Manukin's earlier work. In solid state physics, the development of the first atomic force microscopes (AFMs) [18] also called upon optomechanics. Light reflecting off the backside of a miniature cantilever was used to monitor cantilever deflections caused by short-range forces exerted by a nearby sample.

The independent evolution of various sub-fields of optomechanics continued through the 1990s. A notable experimental achievement during that decade was the demonstration of motional cooling by applying an electronically controlled radiation pressure on a moveable cavity mirror [19]. Additionally, in 1994, Fabre and colleagues [20] showed that optomechanical interactions could in theory produce optical squeezing, that is the reduction of optical quantum noise in one quadrature below the SQL. Due to challenging experimental requirements, this prediction on the quantum nature of optomechanical interactions remained unverified experimentally for over 15 years.

By the beginning of the current millenium, microfabrication techniques had matured to the point of producing very high-quality-factor (high-Q) optical microcavities, such as toroidal microcavities (Fig. 1.3), and high-Q nanomechanical resonators. Light transmitted through high-Q toroidal microcavities exhibited strong amplitude modulation at narrow, distinct frequencies. Tobias Kippenberg and Kerry Vahala demonstrated that these were caused by optical excitation of mechanical eigenmodes

of the entire microcavity [22]. In parallel, Andrew Cleland [23] and Keith Schwab [24] showed that the position of high-Q nanomechanical resonators could be electrically read out with unprecedented sensitivity. These results provided a first bridge between optomechanics research in solid-state physics and optical physics. It also marked the beginning of the extremely rapid progress in experimental investigations of optomechanics over the last few years.

In 2005-2006, experimental demonstrations of dynamical backaction, the amplification [22, 25] and cooling [25, 26, 27] of a mechanical element's motion by injecting an optical signal to the blue and red of cavity resonance, respectively, were made. In 2007-2008, experiments on cavity quantum electrodynamics found that ultracold atoms interacting with an optical standing wave inside a Fabry-Pérot cavity constitutes a unique paradigm of cavity optomechanics [28, 29], where the center-of-mass motion of atoms forms the mechanical element. While solid-state experiments were battling thermal effects that masked the underlying, fundamental optomechanical interactions, atoms-based experiments entered the optomechanical playground with extremely cold mechanical oscillators, enabling the observation of the first quantum optomechanical effect: quantum-measurement backaction [30]. This was the state of research in optomechanics when I started my graduate work in August 2007.

In 2009, optical measurements of the motional spectrum of a mechanical resonator demonstrated sub-SQL imprecision at frequencies far from the mechanical resonance frequency [31, 32], a first step towards quantum-limited position measurements. That same year, the first dual-mechanical-element optomechanical system was experimentally investigated. The setup consisted of two evanescently coupled high-Q microcavities and demonstrated synchronized motion under specific probing conditions [33]. A major milestone was reached in 2010 with the first experimental observation of a quantum-ground-state mechanical resonator [34]. The resonator was cooled to its motional ground state through cryogenic refrigeration and observed optomechanically via a microwave-frequency quantum bit (qbit). A year later, the quantum motional ground state of a solid-state mechanical oscillator was again achieved, this time using the original backation-induced optomechanical cooling method proposed by Braginsky nearly 45 years earlier [35, 36]. Finally, optomechanically induced squeezing of light, discussed by Fabre *et al.* in 1994, was observed experimentally in the Stamper-Kurn group in 2011 [37].

The remainder of my dissertation essentially starts at this point in the history of optomechanics. I consider myself very fortunate to have entered the world of optomechanics at such an effervescent stage of its evolution and to have been able to contribute to some of the key advances in the field.

1.2 What is this dissertation about?

At the core of this dissertation are two experimental realizations pertaining to the interactions between the quantum fluctuations of light and the quantum collective motion of atoms. In the first realization, the zero-point collective motion of an atomic ensemble and the quantum backaction from light on this collective motion were both observed [38]. In the second, the construction of an array of distinguishable quantum-ground-state collective atomic oscillators and the ability to selectively address one targeted oscillator's motion was demonstrated [39]. Both works were important in exposing fundamental properties of cavity optomechanics in the quantum regime and extending the bounds of experimental capabilities. Material presented in this dissertation aims at complementing the already published results.

Chapter 2 is dedicated to setting the theoretical framework relevant for the experimental studies. The chapter first shows how dispersive interactions between atoms and photons inside an optical cavity, captured by the Tavis-Cummings hamiltonian, can be understood as a cavity optomechanical system, where the collective motion of atoms forms an effective mechanical element. The general properties of cavity optomechanical systems are then presented. For this second part, readers are referred to an extensive study authored by the Stamper-Kurn group, Ref. [40], which is included in Appendix A. The final section introduces dimensional operators to translate bosonic operators, used in Ref. [40], into experimentally relevant units.

The principles of photodetection are described in a stand-alone chapter, Chapter 3. The chapter covers both the detection of a single laser beam and the balanced interferometric detection of a pair of beams. It also links the power spectral density (PSD) of optical signals to that of generated photocurrents in both cases. This link is particularly important since every experimental observation reported in this dissertation hinges on a correct mapping of the photon field inside the cavity to detected PSD.

Chapter 4 presents many details concerning the experimental setup, with focus primarily placed on the complicated network of feedback loops used throughout experiments. This naturally leads to Chapters 5–6, which discuss the two core experimental realizations: Chapter 5 pertains to experiments with a single effective atomic oscillator, while Chapter 6 expands to experiments with several atomic oscillators arrayed within an optical cavity. In both of these chapters, the discussion mainly focuses on the theory behind published results and on unpublished experimental methods; the salient features of Refs. [38]–[39] are only mentioned in passing. A final chapter, Chapter 7, summarizes the contents of the dissertation and proposes several research topics for future experiments related to atoms-based cavity optomechanics.

Chapter 2

The theory behind cavity optomechanics

2.1 From cavity quantum electrodynamics to cavity optomechanics

The quantized interactions between atoms and photons inside an optical cavity, such as a Fabry-Pérot cavity, are the subject of study in cavity quantum electrodynamics (CQED). The particular case of one two-level atom interacting with photons is captured by the Jaynes-Cummings model [41]. The extension to an ensemble of two-level atoms interacting with photons is described by the Tavis-Cummings model [42]. These models have been studied at length and are today commonly found in many textbooks ([43, 44, 45, 46, 47, 48] to name a few). Beautifully simple, step-by-step derivations of how to reformulate these models in a manner that highlights optomechanical interactions have been included in the dissertations of two former fellow graduate students, Kater Murch [49] and Tom Purdy [50], as well as in recent work by the Vuletić group [51] and a review article by Dan Stamper-Kurn [52]. In this section, the key steps of these derivations are succinctly presented and the results, adapted to the experiments discussed later in this dissertation.

The hamiltonian describing interactions between N two-level atoms and n photons in an optical cavity, $\hat{H}_{\text{tot}}$, is given by the sum of four energy terms:

$$\hat{H}_{\text{tot}} = \hat{H}_{\text{A,int}} + \hat{H}_{\text{A,ext}} + \hat{H}_{\text{F}} + \hat{H}_{\text{I}}, \tag{2.1}$$

where $\hat{H}_{\text{A,int}}$ and $\hat{H}_{\text{A,ext}}$ represent the energy contained within the internal and motional degrees of freedom of the atomic ensemble, respectively, $\hat{H}_{\text{F}}$ encapsulates the quantized energy of the electromagnetic radiation, and $\hat{H}_{\text{I}}$ captures the atom-photon interactions. Eq. 2.1 treats the optical cavity as a closed system, neglecting any form of communication with the outside world. The open-system case, where light can

enter and exit the cavity, and where atoms are connected to external excitations, will be treated in Section 2.2.

The Tavis-Cummings hamiltonian, $\hat{H}_{\mathrm{TC}}$, corresponds to a subset of $\hat{H}_{\mathrm{tot}}$:

$$\hat{H}_{\mathrm{TC}} = \hat{H}_{\mathrm{A,int}} + \hat{H}_{\mathrm{F}} + \hat{H}_{\mathrm{I}}, \tag{2.2}$$

$$\hat{H}_{\mathrm{A,int}} = \frac{1}{2}\hbar\omega_a \left(\sum_{i=1}^{N} \hat{\sigma}_i^{(3)} + 1 \right), \tag{2.3}$$

$$\hat{H}_{\mathrm{F}} = \hbar\omega_c \hat{a}^\dagger \hat{a}, \tag{2.4}$$

$$\hat{H}_{\mathrm{I}} = \sum_{i=1}^{N} \hbar g(x_i, y_i, z_i) \left(\hat{a}_i^\dagger \hat{\sigma}^{(-)} + \hat{a}_i \hat{\sigma}^{(+)} \right), \tag{2.5}$$

where the rotating-wave approximation (RWA) [43, 53] was applied in Eq. 2.5. Operators $\hat{a}^\dagger$ and $\hat{a}$ are the creation and annihilation operators of the cavity photon field, respectively ($\langle \hat{a}^\dagger \hat{a} \rangle = n$). The Pauli operators act on the the ground, $|g\rangle$, and excited, $|e\rangle$, internal states of each atom as follows: $\hat{\sigma}^{(+)} = |e\rangle \langle g|$, $\hat{\sigma}^{(-)} = |g\rangle \langle e|$, and $\hat{\sigma}^{(3)} = |e\rangle \langle e| - |g\rangle \langle g|$. Frequencies ω_a and ω_c refer to the two-level atomic resonance frequency and the cavity resonance frequency, respectively. The position-dependent frequency g corresponds to the system's Rabi frequency [43, 53]; it captures the per-atom strength of CQED interactions at atom i's location inside the cavity axis, (x_i, y_i, z_i). Its maximum value, $g_o = d \cdot E/\hbar$, is set by both the atomic transition's dipole moment, d, and the single-photon electric field amplitude, $E = \sqrt{\frac{\hbar\omega_c}{\epsilon_o V}}$. Here, ϵ_o is the permittivity of free space and V refers to the light field's effective, round-trip-through-the-cavity volume (*i.e.* twice the optical mode volume inside the cavity, V_{m}).

The Hilbert space for this system spans all possible excitations that can be shared between the N atoms and n photons. This space can be significantly reduced by applying two conditions relevant to the experiments discussed in this dissertation:

- all atoms are initially in their ground internal state,

- the system operates in the "dispersive limit," where the light field is far detuned from the atomic transition, such that at most one photon-induced atomic excitation can exist at any one time (*i.e.* the number of intracavity photons can vary between n and $n - 1$).

Under these conditions, $\hat{H}_{\mathrm{TC}}$ contains $N{+}1$ eigenstates: two bright states, where the collective atomic wavefunction is symmetric, and N-1 dark (*i.e.* sub-radiant) states, where the collective atomic wavefunction is anti-symmetric. The two relevant, bright energy eigenvalues of $\hat{H}_{\mathrm{TC}}$ are

$$E_{\mathrm{TC},\pm} = \hbar\omega_c n - \frac{\hbar\Delta_{\mathrm{ca}}}{2} \pm \hbar\sqrt{\frac{\Delta_{\mathrm{ca}}^2}{4} + n\sum_{i=1}^{N} g^2(x_i, y_i, z_i)}, \tag{2.6}$$

where $\Delta_{\mathrm{ca}} = \omega_c - \omega_a$ is the cavity detuning from atomic resonance. These eigenvalues can be further simplified by applying the dispersive-limit approximation $\Delta_{\mathrm{ca}} \gg \sqrt{N} g_o$:

$$E_{\mathrm{TC},+} = \hbar\omega_c n + \hbar n \frac{\sum_{i=1}^{N} g^2(x_i, y_i, z_i)}{\Delta_{\mathrm{ca}}}, \tag{2.7}$$

$$E_{\mathrm{TC},-} = \hbar\omega_c (n-1) + \hbar\omega_a - \hbar n \frac{\sum_{i=1}^{N} g^2(x_i, y_i, z_i)}{\Delta_{\mathrm{ca}}}. \tag{2.8}$$

Eqs. 2.7–2.8 show that the two bright eigenstates of the system become increasingly distinct as the light field is further detuned from the atomic transition: one approaches the stated initial condition of having n photons and no atomic excitation ("+" state), while the other approaches the case of having one steady excitation within the atomic ensemble and $n-1$ photons ("−" state). From this point forward, only the experimentally relevant "+" state will considered.

Optomechanics enters the discussion by introducing the atoms' motional degree of freedom and making the position dependence of $g(x_i, y_i, z_i)$ explicit. To do so, three specifics about the experiment must be stated, all of which will be further described in Chapter 4. First, the photons with which atoms dispersively interact, the "probe" photons, are contained in a $\mathrm{TEM}_{0,0}$ mode of a near-planar Fabry-Pérot cavity. Second, the atoms are trapped along the cavity axis by a far off-resonance optical dipole trap (FORT). The trap is formed by one or two other $\mathrm{TEM}_{0,0}$ optical modes of the cavity that are red-detuned by several million transition linewidths from the two-level transition, and hence have negligible CQED interactions with atoms. Third, atoms are cooled to ultracold temperatures. The trapped atomic ensemble's spatial extent in directions transverse to the cavity axis is therefore much smaller than the widths of the $\mathrm{TEM}_{0,0}$ modes (see Fig. 2.1), meaning that each atom's transverse motion negligibly contributes to the light-atom dynamics; the cavity-atom system can be effectively treated as a one-dimensional system along the cavity axis [49, 50] ($g(x_i, y_i, z_i) \rightarrow g(z_i)$). As a side note, "radial" optomechanics, *i.e.* optomechanical coupling to the transverse motion of atoms, has often been suspected to contribute to reduced trap lifetimes and odd features in the optomechanical responses observed in our experiments, but we have performed no detailed experimental examinations to confirm these suspicions.

In this context, trapped atoms oscillate quantum mechanically about minimum points of the FORT standing-wave potential, which varies sinusoidally along the cavity axis. However, by virtue of their ultracold temperatures, atoms explore only a small fraction of this sinusoidal potential, meaning their motion can be well approximated by that of a quantum harmonic oscillator (Fig. 2.1):

$$\hat{H}_{\mathrm{A,ext}} = \sum_{i=1}^{N} \hbar\omega_{m,i} \, \hat{b}_i^\dagger \hat{b}_i, \tag{2.9}$$
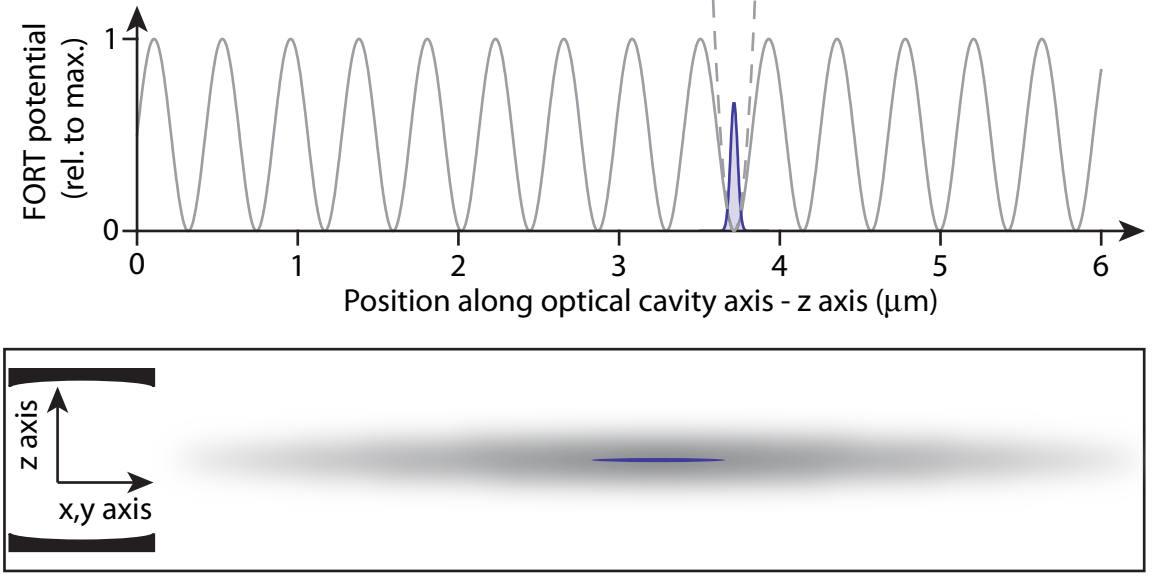
Figure 2.1: Schematic of a single-color FORT (grey) holding a distribution of atoms (blue) in one potential minimum. The top panel shows the gaussian envelop of the atomic distribution within the FORT's standing-wave potential distribution along the cavity axis, as well as the harmonic potential approximation (dashed grey) at the atoms' trap location. The lower panel highlights the much smaller size of the atomic distribution relative to FORT's optical intensity profile. The inset shows the corresponding, vertical orientation of the optical cavity for reference. Note that the cavity, atom and FORT orientation in the lower panel is rotated relative to their orientation in the the top panel for clarity. Cartesian directions: z points along the cavity axis, while x and y are transverse to the cavity axis.

where $\hat{b}_i^\dagger$ and $\hat{b}_i$ are the motional creation and annihilation operators, and $\omega_{m,i}$ the mechanical oscillation frequency of atom i. Oscillating atoms also only sweep across a small fraction of the probe's standing-wave potential because of their ultracold temperatures. The spatial dependence of atom i's interaction frequency with the probe can therefore be approximated by a low-order expansion of its quantum mechanical motion, $\hat{z}_i = z_{\mathrm{HO}}(\hat{b}_i + \hat{b}_i^\dagger)$, about its equilibrium point z_i:

$$
\begin{aligned}
g^2(z_i + \hat{z}_i) &= g_o^2 \sin^2\left(k_p(z_i + \hat{z}_i)\right), &\quad (2.10)\\
&\simeq g_o^2 \left(\sin^2(k_p z_i) + k_p \hat{z}_i \, \sin(2k_p z_i) + (k_p \hat{z}_i)^2 \cos(2k_p z_i)\right) &\quad (2.11)
\end{aligned}
$$

where k_p is the probe wavenumber. The term

$$
z_{\mathrm{HO}} = \sqrt{\frac{\hbar}{2m\omega_{m,i}}} \qquad (2.12)
$$

refers to the single-atom harmonic oscillator length, with m the atomic mass.

Grouping together the energy eigenstates of the Tavis-Cummings model in the specific dispersive regime relevant to experiments discussed in this dissertation with the harmonic-oscillator-like motion of atoms, the complete closed-system hamiltonian, $\hat{H}_{\rm tot}$, can be expressed as:

$$
\hat{H}_{\rm tot} = \sum_{i=1}^{N} \hbar \omega_{m,i}\, \hat{b}_i^\dagger \hat{b}_i + \hbar \omega_c \hat{a}^\dagger \hat{a} +
$$
$$
\hbar \frac{\hat{a}^\dagger \hat{a} g_o^2}{\Delta_{\rm ca}} \sum_{i=1}^{N} \left(\sin^2(k_p \hat{z}_i) + k_p \hat{z}_i \, \sin(2k_p \hat{z}_i) + (k_p \hat{z}_i)^2 \cos(2k_p \hat{z}_i) \right). \quad (2.13)
$$

Three position-dependent atom-photon interactions terms are included in Eq. 2.13. Each term has a distinct significance. The first corresponds to a static shift in the cavity's effective resonance frequency due to the presence of atoms:

$$
\omega_c' = \omega_c + \frac{g_o^2}{\Delta_{\rm ca}} \sum_{i=1}^{N} \sin^2(k_p z_i). \quad (2.14)
$$

In the dispersive regime, atoms act as a medium of index of refraction, which explains this additive shift in cavity resonance. The second term, which I will label $\hat{H}_{\rm dyn}$, is responsible for "linear" optomechanics, where the interaction strength is linearly dependent on each atom's displacement. It is the CQED analog of Braginsky's original proposal for optomechanics [3] and has been studied by three different research groups [29, 30, 51]. The last term corresponds to a coupling between each atom's displacement squared, or equivalently its *mechanical energy*, and the probe photon field. This type of optomechanical interaction is commonly termed "quadratic" optomechanics and has been explored by only two large size mechanical systems, one involving thousands of atoms [54] and one involving a thin silicon membrane [55]; several earlier single-atom CQED experiments also effectively studied quadratic optomechanics [56, 57, 58] even though their results were not framed in those terms. Since experiments described in this dissertation are based exclusively on linear optomechanical interactions, I will drop the quadratic and higher-order coupling terms.

The final ingredient needed as part of this atoms-based optomechanics recipe is the concept of collective mechanical variable. Suppose all N atoms are trapped at the same spatial location, and hence have the same linear coupling ($k_p z_i = \phi$) and the same mechanical oscillation frequency ($\omega_{m,i} = \omega_m$). The linear-optomechanics hamiltonian term in Eq. 2.13 is then dependent on a sum of equally weighted displacement operators:

$$
\hat{H}_{\rm dyn} = \hbar \frac{\hat{a}^\dagger \hat{a} g_o^2}{\Delta_{\rm ca}} k_p \sin(2\phi) \sum_{i=1}^{N} \hat{z}_i. \quad (2.15)
$$

This sum is related to the center-of-mass (CM) mode of motion of the entire atomic

ensemble:

$$\hat{b}_{\mathrm{CM}} \;\; = \;\; \frac{1}{\sqrt{N}} \sum_{i=1}^{N} \hat{b}_i, \tag{2.16}$$

$$\hat{Z}_{\mathrm{CM}} \;\; = \;\; Z_{\mathrm{HO}} \left(\hat{b}_{\mathrm{CM}} + \hat{b}_{\mathrm{CM}}^\dagger \right) = \frac{1}{N} \sum_{i=1}^{N} \hat{z}_i, \tag{2.17}$$

where $Z_{\mathrm{HO}} = z_{\mathrm{HO}}/\sqrt{N}$ is the harmonic oscillator length of the CM mode. In this scenario, then, probe photons effectively interact with a single atomic oscillator of mass $m_{\mathrm{CM}} = Nm$:

$$\hat{H}_{\mathrm{dyn}} = \hbar g_{\mathrm{OM}} \hat{a}^\dagger \hat{a} \frac{\hat{Z}_{\mathrm{CM}}}{Z_{\mathrm{HO}}}, \tag{2.18}$$

where

$$g_{\mathrm{OM}} = \frac{N g_o^2}{\Delta_{\mathrm{ca}}} \sin(2\phi) k_p Z_{\mathrm{HO}} \tag{2.19}$$

is the linear optomechanical coupling rate.

This result can be generalized to instances where not all atoms are situated at the same trap location. If atoms are dispersed among several potential minima, labeled by parameter j, then each populated minimum can be attributed a CM displacement operator, $\hat{Z}_{\mathrm{CM},j}$, with a particular collective harmonic oscillator length, $Z_{\mathrm{HO,j}}$, and optomechanical coupling rate, $g_{\mathrm{OM,j}}$:

$$\hat{Z}_{\mathrm{CM},j} \;\; = \;\; \frac{1}{N_j} \sum_{i=1}^{N_j} \hat{z}_i, \tag{2.20}$$

$$Z_{\mathrm{HO,j}} \;\; = \;\; \sqrt{\frac{\hbar}{2 N_j m \omega_{m,j}}}, \tag{2.21}$$

$$g_{\mathrm{OM,j}} \;\; = \;\; \frac{N_j g_o^2}{\Delta_{\mathrm{ca}}} \sin(2\phi_j) k_p Z_{\mathrm{HO,j}}, \tag{2.22}$$

$$\hat{H}_{\mathrm{dyn}} \;\; = \;\; \sum_j \hbar g_{\mathrm{OM,j}} \hat{a}^\dagger \hat{a} \frac{\hat{Z}_{\mathrm{CM},j}}{Z_{\mathrm{HO,j}}}, \tag{2.23}$$

where N_j, $\omega_{m,j}$ and $\phi_j = k_p z_j$ are the number of atoms, mechanical oscillation frequency and local linear coupling phase at location j, respectively. Optomechanics in this more general case takes place between cavity probe photons and an array of collective motional modes, one from each populated site. When each member of the array has a distinct mechanical frequency, $\omega_{m,j}$, each member's contribution to the overall optomechanical interactions can be individually identified. This idea lays the foundations on which the multi-oscillator experiments, detailed in Chapter 6, were constructed.

In the more specific case where each populated trap minimum has the same mechanical oscillation frequency, ω_m, Eqs. 2.20–2.23 can be reformulated as

$$\hat{Z}_{\mathrm{CM,eff}} = \frac{1}{N_{\mathrm{eff}}} \sum_j N_j \hat{Z}_{\mathrm{CM},j} \sin(2\phi_j) = \frac{1}{N_{\mathrm{eff}}} \sum_{i=1}^{N} \hat{z}_i \sin(2\phi_i), \qquad (2.24)$$

$$Z_{\mathrm{HO,eff}} = \sqrt{\frac{\hbar}{2N_{\mathrm{eff}}m\omega_m}}, \qquad (2.25)$$

$$g_{\mathrm{OM,eff}} = \frac{N_{\mathrm{eff}}g_o^2}{\Delta_{\mathrm{ca}}} k_p Z_{\mathrm{HO,eff}}, \qquad (2.26)$$

$$\hat{H}_{\mathrm{dyn}} = \hbar g_{\mathrm{OM,eff}} \hat{a}^\dagger \hat{a} \frac{\hat{Z}_{\mathrm{CM,eff}}}{Z_{\mathrm{HO,eff}}}, \qquad (2.27)$$

where

$$N_{\mathrm{eff}} = \sum_{i=1}^{N_j} \sin^2(2\phi_i). \qquad (2.28)$$

Despite the spatial distribution of atoms over multiple FORT sites, optomechanics in this particular case takes place between the photon field and a single *effective* CM mode, where each atom's contribution to the effective collective mode is weighted by its coupling to the light field, $\sin(2\phi_i)$. The mass of this effective atomic oscillator is mN_{eff}. In the limit of all atoms being placed in the same potential minimum ($\phi_i \to \phi$ for all i), the effective mechanical mode coupling to the light field becomes the atomic ensemble's CM mode, and Eqs. 2.18–2.19 are recovered.

2.2 Linear cavity optomechanics

This previous section details how CQED can be adapted as a cavity optomechanical system. Cavity optomechanics also comes in many other forms, as highlighted in Chapter 1. Each form has its own strengths and weaknesses, allowing it to study a certain subset of cavity-optomechanics properties. As these subfields become evermore specialized, translation from one experimental realization to another becomes lost. And yet the fundamental optomechanical interactions at play remain the same across applications. In this section, I introduce an amplifier model to represent and understand cavity optomechanics in general. The point of this model is to serve as a common language in the multi-lingual world of optomechanics.

One of the scientific products of my graduate work was the development of an optomechanical amplifier model, published in Ref. [40]. The model begins by considering linear cavity optomechanics in the Heisenberg picture, where the optical and mechanical fields evolve in time and frequency. The evolution of these fields is represented as a feedback circuit, with an input and output channel for each field. Just

Properties	Definition in published amplifier model	Definition in dissertation
Fourier transforms	$\tilde{f}(\omega) = \int f(t)e^{i\omega t}dt$ $f(t) = \int \tilde{f}(\omega)e^{-i\omega t}d\omega$	$\tilde{f}(\omega) = \frac{1}{\sqrt{2\pi}} \int f(t)e^{i\omega t}dt$ $f(t) = \frac{1}{\sqrt{2\pi}} \int \tilde{f}(\omega)e^{-i\omega t}d\omega$
Quadrature operators		
amplitude	$\hat{f}_+ = \hat{f} + \hat{f}^\dagger$	$\hat{f}_+ = \left(\hat{f} + \hat{f}^\dagger\right)/\sqrt{2}$
phase	$\hat{f}_- = i\left(\hat{f} - \hat{f}^\dagger\right)$	$\hat{f}_- = i\left(\hat{f} - \hat{f}^\dagger\right)/\sqrt{2}$

Table 2.1: Definitions of Fourier transforms and quadrature operators. The table outlines the unconventional definitions used in the linear optomechanical amplifier model (see Appendix A), and the more conventional definitions used throughout this dissertation.

as with any feedback circuits, the optomechanical outputs are shown to be related to the inputs by way of a transfer matrix. What then distinguishes one experimental realization from another are the entries to this matrix. The model accurately predicts two well-known optomechanical phenomena: ponderomotive squeezing [20, 37] (*i.e.* optical squeezing caused by the mechanical motion) and electromagnetically induced transparency [59, 60]. Moreover, thanks to its general, transfer-matrix-based language, the model also shows that these two phenomena are intimately related. The published theoretical results are adapted to account for experimental realities, in particular limited detection efficiency.

A copy of the publication is included in Appendix A. Readers are referred to the publication for details regarding this optomechanical amplifier model and to learn more about some of the salient features of optomechanics. Some of the results, particularly the constituents of input-to-output transfer matrices, will be used in later chapters of this dissertation. Readers are warned that the definitions used for Fourier transforms and quadrature operators in the publication are *not* normalized. These definitions will *not* be employed as part of this dissertation to avoid introducing factors of 2 and $\sqrt{2}$ when relating theory to experimental results. Instead, more conventional, properly normalized definitions will be used. Both series of definitions are explicitly stated side-by-side in Table 4.1 to help readers visualize the differences.

2.3   The units of an experimentalist

Readers having carefully scoped through the published linear optomechanical amplifier model (see Appendix A) will note that quoted results are normalized by the inputs, sweeping away any need for units. In addition, both mechanical and optical operators are bosonic operators, with experimentally inadequate units. For instance, optical inputs and outputs have powers in units of "quanta/second," not "watts." In this section, I complement the work outlined in the publication by introducing operators with experimentally relevant units for both the mechanical and optical fields.

In Section 2.1, the position operator, $\hat{z}$, was subtly introduced with units of distance by including the harmonic oscillator length, z_{HO}. This was not the case in the optomechanical amplifier model, where a dimensionless position operator was instead defined. Converting from bosonic position (momentum) operators to dimensional operators thus only requires factoring in the harmonic oscillator length (momentum, $p_{\text{HO}} = \sqrt{\hbar m \omega_m / 2}$):

$$\hat{z} = z_{\text{HO}} \left(\hat{b} + \hat{b}^\dagger \right), \tag{2.29}$$

$$\hat{p} = i p_{\text{HO}} \left(\hat{b} - \hat{b}^\dagger \right). \tag{2.30}$$

A similar approach can be taken for the intracavity optical field operators, since photons can also be represented as particles in a quantum harmonic oscillator. However, instead of a length or a momentum, the photon energy *inside* the cavity, $\hbar \omega_c$, must be used to convert from bosonic operators to dimensional operators:

$$\hat{c}^\dagger = \sqrt{\hbar \omega_c} \hat{a}^\dagger, \tag{2.31}$$

$$\hat{c} = \sqrt{\hbar \omega_c} \hat{a}, \tag{2.32}$$

$$\hat{c}_+ = \sqrt{\frac{\hbar \omega_c}{2}} \left(\hat{a} + \hat{a}^\dagger \right), \tag{2.33}$$

$$\hat{c}_- = i \sqrt{\frac{\hbar \omega_c}{2}} \left(\hat{a} - \hat{a}^\dagger \right). \tag{2.34}$$

I stress the word "inside" because of a subtlety: an incoming photon with frequency ω_p, *i.e.* detuned from cavity resonance by $\omega_p - \omega_c$, will be perceived as a particle with energy $\hbar \omega_c$ if it enters the cavity. Why? Because a cavity cannot distinguish frequencies; it can only filter based on its lorentzian linewidth. This subtle point is, for all intent and purpose, irrelevant for high-quality-factor (high-Q) optical cavities, since photons that enter the cavity satisfy $\omega_p \sim \omega_c$.

Dimensional operators for the optical fields outside the cavity can also be defined. Recalling that operator $\hat{\alpha}$ used in the optomechanical amplifier model has units of $\sqrt{\text{photons/second}}$, its dimensional analog requires the energy of traveling photons,

$\hbar\omega_p$:

$$\hat{\zeta} = \sqrt{\hbar\omega_p}\hat{\alpha}, \tag{2.35}$$

$$\hat{\zeta}^\dagger = \sqrt{\hbar\omega_p}\hat{\alpha}^\dagger, \tag{2.36}$$

$$\hat{\zeta}_+ = \sqrt{\frac{\hbar\omega_p}{2}}(\hat{\alpha} + \hat{\alpha}^\dagger), \tag{2.37}$$

$$\hat{\zeta}_- = i\sqrt{\frac{\hbar\omega_p}{2}}(\hat{\alpha} - \hat{\alpha}^\dagger). \tag{2.38}$$

The mechanical degree of freedom also has input and output field operators. These traveling fields capture energy exchanges between the mechanical element and its environment, much like the traveling optical fields represents photons entering and exiting the cavity from the outside world. The optomechanical amplifier model made use of operator $\hat{\eta}$, defined with units of $\sqrt{\text{phonons/second}}$, to represent traveling phonons. This operator can be used to define dimensional quadrature operators of traveling phonons, $\hat{\xi}_+$ and $\hat{\xi}_-$, which bridges the position and momentum of the mechanical element, respectively, with the element's surroundings:

$$\hat{\xi}_+ = z_{\text{HO}}\left(\hat{\eta} + \hat{\eta}^\dagger\right), \tag{2.39}$$

$$\hat{\xi}_- = ip_{\text{HO}}\left(\hat{\eta} - \hat{\eta}^\dagger\right). \tag{2.40}$$

What is the physical meaning of both dimensional quadrature operators? From Eq. (6) in Appendix A, $\hat{\xi}_+$ and $\hat{\xi}_-$ are known to couple to the mechanical element's velocity and acceleration, respectively. $\hat{\xi}_-$ is therefore related to classical and quantum-level forces acting on the element: $F = \sqrt{\Gamma_m}\left\langle\hat{\xi}_-\right\rangle$ (see Eq.(35) in Appendix A). $\hat{\xi}_+$, however, has a much more obscure meaning. Perhaps it represents a classical and quantum-level impulse imparted on the element: $J = m\sqrt{\Gamma_m}\left\langle\hat{\xi}_+\right\rangle$. An impulse and a force are not sharply distinct, so this proposed definition is somewhat weak. Regardless, $\hat{\xi}_+$ does capture the quantum fluctuations that the mechanical element's position inherits from the outside world, which contributes to the position's Heisenberg uncertainty.

The bosonic and dimensional operators quoted above apply in the time-domain. Their respective frequency-domain counterpart carry an additional $(\text{rad/second})^{-1}$. Unless otherwise specified, all frequencies stated in both the optomechanical amplifier model and this dissertation are in radial units, not cyclical units.

Chapter 3

Optical Detection

In plain terms, photodetection operates by converting traveling photons (i.e. optical power) into traveling electrons (i.e. electrical current) through absorption in a semiconductor material. Although the premise is quite simple, the quantum mechanical description of this process is much more complicated. Roy Glauber was first to provide a mathematical description of photodetection in a Nobel-prize-winning article, Ref. [61]. The theory has since been treated in a number of books, including [47, 62, 63, 64] to cite a few. In this chapter, I introduce a few important concepts regarding photodetection, and apply these concepts to model balanced detection.

3.1 The basics of photodetection

The time and frequency-domain evolution of light can be studied in the Heisenberg picture using the quantized optical field operators $\hat{\zeta}$ and $\hat{\alpha}$ introduced in Chapter 2. These operators respect the following commutation relations in each Fourier-conjugate domain:

$$\left[\hat{\zeta}(t), \hat{\zeta}^{\dagger}(t')\right] = \hbar\omega_L \left[\hat{\alpha}(t), \hat{\alpha}^{\dagger}(t')\right] = \hbar\omega_L \delta(t - t'), \tag{3.1}$$

$$\left[\hat{\tilde{\zeta}}(\omega), \hat{\tilde{\zeta}}(\omega')\right] = \hbar\omega_L \left[\hat{\tilde{\alpha}}(\omega), \hat{\tilde{\alpha}}^{\dagger}(\omega')\right] = \hbar\omega_L \tilde{\delta}(\omega - \omega'), \tag{3.2}$$

where ω_L is optical frequency of the traveling light field.

An ideal laser emits a coherent state of light, that is a stream of identical photons, each having an optical frequency ω_L. The coherence of the emitted light is captured by the corresponding expectation values of the optical field operators:

$$\left\langle \hat{\zeta}_L(t) \right\rangle = \sqrt{\hbar\omega_L} \left\langle \hat{\alpha}_L(t) \right\rangle = \sqrt{\hbar\omega_L} \left\langle \hat{\alpha}_L(0) \times e^{-i\omega_L t} \right\rangle = \sqrt{P_L} e^{-i\omega_L t}, \tag{3.3}$$

$$\left\langle \hat{\tilde{\zeta}}_L(\omega) \right\rangle = \sqrt{\hbar\omega_L} \left\langle \hat{\tilde{\alpha}}_L(\omega) \right\rangle = \sqrt{\hbar\omega_L} \left\langle \hat{\alpha}_L(0) \times \sqrt{2\pi}\tilde{\delta}(\omega - \omega_L) \right\rangle, \tag{3.4}$$

$$= \sqrt{P_L} \times \sqrt{2\pi}\tilde{\delta}(\omega - \omega_L), \tag{3.5}$$

where $P_L = \hbar\omega_L \left\langle |\hat{\alpha}_L(0)|^2 \right\rangle = \hbar\omega_L \left\langle \hat{\alpha}_L(0) \right\rangle^2$ is the laser beam's optical power.

If a weak amplitude or phase modulation, at frequency $\omega_{\text{mod}} \ll \omega_L$, is applied to the laser emission, a pair of small sidebands, at frequencies $\omega_L + \omega_{\text{mod}}$ and $\omega_L - \omega_{\text{mod}}$, respectively, will be added to the traveling field:

$$\left\langle \hat{\zeta}_L(t) \right\rangle = \sqrt{P_L} \left(e^{-i\omega_L t} + \sqrt{\frac{\eta}{2}} \left[e^{-i(\omega_L + \omega_{\text{mod}})t} + e^{-i(\omega_L - \omega_{\text{mod}})t + i\theta} \right] \right), \quad (3.6)$$

$$\left\langle \hat{\tilde{\zeta}}_L(\omega) \right\rangle = \sqrt{2\pi P_L} \times \quad\quad\quad\quad\quad\quad\quad\quad\quad\quad\quad\quad\quad\quad\quad\quad (3.7)$$

$$\left(\tilde{\delta}(\omega - \omega_L) + \sqrt{\frac{\eta}{2}} \left[\tilde{\delta}(\omega - \omega_L - \omega_{\text{mod}}) + e^{i\theta} \tilde{\delta}(\omega - \omega_L + \omega_{\text{mod}}) \right] \right),$$

where the total power contained in the sidebands, $P_{\text{mod}} = \eta P_L$, is set by the modulation depth, $\eta \ll 1$. The phase θ specifies the quadrature of the applied modulation, *i.e.* whether the modulation is applied to the laser beam's amplitude ($\theta = 0$), phase ($\theta = \pi$) or a combination thereof.

A photodetector records optical power, or equivalently electric-field beats. Consequently, a detector exposed to a single light beam will measure the mean power and amplitude modulations of that beam, but will carry no information about its phase modulation. As a demonstration, consider the photodetection of the laser beam defined in Eqs. 3.6–3.7, with again $\eta \ll 1$:

$$\left\langle \hat{I}(t) \right\rangle = \sqrt{\epsilon} G \left\langle \hat{\zeta}_L^\dagger(t) \hat{\zeta}_L(t) \right\rangle = \sqrt{\epsilon} G \left\langle \hat{\zeta}_L^\dagger(t) \right\rangle \left\langle \hat{\zeta}_L(t) \right\rangle, \quad\quad\quad (3.8)$$

$$= \sqrt{\epsilon} G \left(P_L + \sqrt{2 P_L P_{\text{mod}}} \left[\cos(\omega_{\text{mod}} t) + \cos(\omega_{\text{mod}} t + \theta) \right] \right), \quad (3.9)$$

where $\left\langle \hat{I}(t) \right\rangle$ is the resulting photocurrent, and G and ϵ refer to the optical-to-electrical conversion gain and the overall photodetection efficiency, respectively. Indeed, the right-hand side of Eq. 3.9 is identically zero when $\theta = \pi$, but can have a non-zero value when $\theta = 0$. In order to sense phase modulations, a more intricate detection method must be employed. One approach is to expose the photodetector to two distinct and overlapping laser beams, and record optical beats between both beams. This is the premise of balanced homodyne and heterodyne detection discussed in Section 3.2.

Additionally, notice that from Eqs. 3.8 and 3.9 the photodetector appears not to have a record of the light's quantum fluctuations. Indeed, the photocurrent's expectation value does not show signs quantum optical fluctuations, since $\hat{\zeta}^\dagger(t)$ and $\hat{\zeta}(t)$ are normally ordered, but the photocurrent's squared magnitude, $\left\langle |\hat{I}(t)|^2 \right\rangle$, does. Quantum optical fluctuations can therefore be experimentally observed by monitoring the detected photocurrent's electrical power across a resistor, a trivial measurement to realize. However, expressing $\left\langle |\hat{I}(t)|^2 \right\rangle$ analytically requires the "two time time-ordered

correlation function." I will not pretend to be an expert on this complicated quantum correlation function, but I will say that its Fourier transform yields the power spectral density (PSD) of the detected photocurrent by virtue of the Wiener-Khintchine theorem. PSDs can be straightforwardly calculated from *normalized* Fourier transforms, which have the form:

$$\tilde{f}(\omega) = \lim_{T \to \infty} \frac{1}{\sqrt{T}} \int_{-T}^{T} f(t)e^{i\omega t}dt. \tag{3.10}$$

PSDs are not, strictly speaking, related to standard Fourier transforms, such as those defined in Section 2.2, since powers are not square integrable functions. Following the example of certain authors [65], I will overlook this strict definition and nonetheless formulate the PSD of the photocurrent considered in Eq. 3.9, $S_{\text{II}}(\omega)$, in terms of its standard Fourier transform, $\hat{\tilde{I}}(\omega)$:

$$S_{\text{II}}(\omega) = \frac{\left\langle \hat{\tilde{I}}^\dagger(\omega')\hat{\tilde{I}}(\omega) \right\rangle}{2\pi\tilde{\delta}(\omega' - \omega)} = \frac{\epsilon G^2 \left\langle \hat{\tilde{\zeta}}_L^\dagger(\omega')\hat{\tilde{\zeta}}_L(\omega')\hat{\tilde{\zeta}}_L^\dagger(\omega)\hat{\tilde{\zeta}}_L(\omega) \right\rangle}{2\pi\tilde{\delta}(\omega' - \omega)}, \tag{3.11}$$

$$\begin{aligned}
\frac{S_{\text{II}}(\omega)}{\epsilon G^2} = {} & P_L^2\tilde{\delta}(\omega) + P_L\sqrt{2P_L P_{\text{mod}}}\left(1 + \cos(\theta)\right)\left[\tilde{\delta}(\omega + \omega_{\text{mod}}) + \tilde{\delta}(\omega - \omega_{\text{mod}})\right] \\
& + P_L P_{\text{mod}}\left(1 + \cos(\theta)\right)\left[\tilde{\delta}(\omega + 2\omega_{\text{mod}}) + \tilde{\delta}(\omega - 2\omega_{\text{mod}})\right] \\
& + \frac{P_L \hbar \omega_L}{2\pi}.
\end{aligned} \tag{3.12}$$

The final term in Eq. 3.12 represents the light's spectrally uniform quantum fluctuations. Mathematically, the term comes from normally ordering the field operators in Eq. 3.11 using the commutation relation in Eq. 3.2. Physically, this term is due to the random emission times of laser photons, which leads to random detection times at the photodetector, hence the name "shot noise" often attributed to quantum fluctuations. Shot noise can also be understood as beats between the laser's carrier tone, at frequency ω_L, and the quantum mechanical fluctuations of the vacuum, which in free-space are flat across frequency.

Lastly, I note that $S_{\text{II}}(\omega)$ has units of $\text{W}^2/(\text{rad/s})$. Its analog in units of W^2/Hz is related by a factor of 2π: $S_{\text{II}}(f) = 2\pi \times S_{\text{II}}(\omega)$. Eq. 3.12 therefore translates to the following expression in cyclical units:

$$\begin{aligned}
\frac{S_{\text{II}}(f)}{\epsilon G^2} = {} & P_L^2\tilde{\delta}(f) + P_L\sqrt{2P_L P_{\text{mod}}}\left(1 + \cos(\theta)\right)\left[\tilde{\delta}(f + f_{\text{mod}}) + \tilde{\delta}(f - f_{\text{mod}})\right] \\
& + P_L P_{\text{mod}}\left(1 + \cos(\theta)\right)\left[\tilde{\delta}(f + 2f_{\text{mod}}) + \tilde{\delta}(f - 2f_{\text{mod}})\right] \\
& + P_L(\hbar \cdot 2\pi\, f_L).
\end{aligned} \tag{3.13}$$
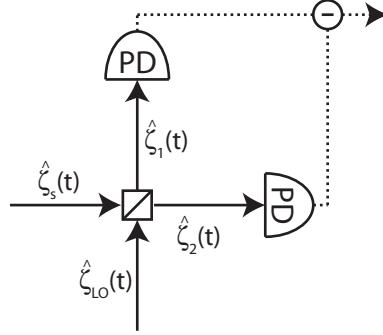
Figure 3.1: Schematic of a balanced photodetector setup. The LO and signal beams are evenly split and overlapped using a beamsplitter. The beamsplitter's two output ports are separately detected, and the two resulting photocurrents are subtracted.

3.2 Balanced homodyne / heterodyne detection

A general balanced detector is shown in Fig. 3.1. A reference optical beam, the "local oscillator" (LO), assumed to be a pure coherent tone, is overlapped with another optical beam, the signal, carrying some modulation of interest at frequency ω_{mod} and relative phase θ, on a 50:50 beamsplitter. In the context of experiments discussed in this dissertation, probe light exiting the science cavity forms the signal beam. The LO and signal beams are separately expressed as follows:

$$\left\langle \hat{\zeta}_{\mathrm{LO}}(t) \right\rangle = \sqrt{P_{\mathrm{LO}}} e^{-i\omega_{\mathrm{LO}} t + i\theta_{\mathrm{LO}}}, \tag{3.14}$$

$$\left\langle \hat{\zeta}_s(t) \right\rangle = \sqrt{P_s} \left(e^{-i\omega_s t} + \sqrt{\frac{\eta}{2}} \left(e^{-i(\omega_s+\omega_{\mathrm{mod}}) t} + e^{-i(\omega_s-\omega_{\mathrm{mod}}) t + i\theta} \right) \right), \tag{3.15}$$

where ω_{LO} (ω_s) and P_{LO} (P_s) are the LO's (signal's) carrier frequency and power, respectively, and θ_{LO} is the LO's phase relative to the signal beam at time t $= 0$. The signal's modulation depth, $\eta = P_{\mathrm{mod}}/P_s$, is assumed to be much smaller than unity. Notice that the signal field (Eq. 3.15) is effectively identical to the laser field studied in the previous section (Eq. 3.6).

The beamsplitter's output ports can be expressed in terms of the input operators, defined in Eqs. 3.14–3.15:

$$\hat{\zeta}_1(t) = \hat{\zeta}_{\mathrm{LO}}(t)/\sqrt{2} + i\hat{\zeta}_s(t)/\sqrt{2}, \tag{3.16}$$

$$\hat{\zeta}_2(t) = i\hat{\zeta}_{\mathrm{LO}}(t)/\sqrt{2} + \hat{\zeta}_s(t)/\sqrt{2}. \tag{3.17}$$

Both of the output ports of the beamsplitter are separately detected. The photocur-

rent produced by each detector is given by

$$\left\langle \hat{I}_1(t) \right\rangle = \sqrt{\epsilon_1} G_1 \left\langle \hat{\zeta}_1^\dagger(t) \hat{\zeta}_1(t) \right\rangle, \tag{3.18}$$

$$\left\langle \hat{\zeta}_1^\dagger(t) \hat{\zeta}_1(t) \right\rangle = \frac{P_{\mathrm{LO}}}{2} + \frac{\left\langle \hat{\zeta}_s^\dagger(t) \hat{\zeta}_s(t) \right\rangle}{2}$$
$$+ i \frac{\sqrt{P_{\mathrm{LO}}}}{2} \left\langle \hat{\zeta}_s(t) e^{i\omega_{\mathrm{LO}} t - i\theta_{\mathrm{LO}}} - \hat{\zeta}_s^\dagger(t) e^{-i\omega_{\mathrm{LO}} t + i\theta_{\mathrm{LO}}} \right\rangle, \tag{3.19}$$

and

$$\left\langle \hat{I}_2(t) \right\rangle = \sqrt{\epsilon_2} G_2 \left\langle \hat{\zeta}_2^\dagger(t) \hat{\zeta}_2(t) \right\rangle, \tag{3.20}$$

$$\left\langle \hat{\zeta}_2^\dagger(t) \hat{\zeta}_2(t) \right\rangle = \frac{P_{\mathrm{LO}}}{2} + \frac{\left\langle \hat{\zeta}_s^\dagger(t) \hat{\zeta}_s(t) \right\rangle}{2}$$
$$- i \frac{\sqrt{P_{\mathrm{LO}}}}{2} \left\langle \hat{\zeta}_s(t) e^{i\omega_{\mathrm{LO}} t - i\theta_{\mathrm{LO}}} - \hat{\zeta}_s^\dagger(t) e^{-i\omega_{\mathrm{LO}} t + i\theta_{\mathrm{LO}}} \right\rangle. \tag{3.21}$$

Both detectors record half of the LO and signal powers entering the beamsplitter, as well as half the total power contained LO-signal beats. However, the detectors measure the LO-signal beats with opposite phases. These optical beats, which carry the relevant amplitude and/or phase information, can be isolated from the LO and signal powers by taking the difference between $\hat{I}_1$ and $\hat{I}_2$, assuming each detector has the same overall detection efficiency ($\epsilon_1 = \epsilon_2 = \epsilon$) and gain ($G_1 = G_2 = G$):

$$\langle I_{\mathrm{bal}}(t) \rangle = \left\langle \hat{I}_1(t) - \hat{I}_2(t) \right\rangle, \tag{3.22}$$

$$= i\sqrt{\epsilon} G \sqrt{P_{\mathrm{LO}}} \left\langle \hat{\zeta}_s(t) e^{i\omega_{\mathrm{LO}} t - i\theta_{\mathrm{LO}}} - \hat{\zeta}_s^\dagger(t) e^{-i\omega_{\mathrm{LO}} t + i\theta_{\mathrm{LO}}} \right\rangle, \tag{3.23}$$

$$= \sqrt{\epsilon} G \sqrt{P_{\mathrm{LO}}} \cdot \left[2\sqrt{P_s} \sin\left(\Delta_{\mathrm{LO},s} t + \theta_{\mathrm{LO}}\right) \right. \tag{3.24}$$

$$\left. + \sqrt{2P_{\mathrm{mod}}} \{ \sin((\Delta_{\mathrm{LO},s} + \omega_{\mathrm{mod}})t + \theta_{\mathrm{LO}}) + \sin((\Delta_{\mathrm{LO},s} - \omega_{\mathrm{mod}})t + \theta_{\mathrm{LO}} - \theta) \} \right],$$

where $\Delta_{\mathrm{LO},s} = \omega_s - \omega_{\mathrm{LO}}$. This difference measurement is part of the fundamental premise of balanced detection, with homodyne and heterodyne types corresponding to $\Delta_{\mathrm{LO},s} = 0$ and $\Delta_{\mathrm{LO},s} \neq 0$, respectively.

Pertinent signal information is magnified by a factor of $\sqrt{P_{\mathrm{LO}}}$ on the balanced-detection photocurrent, I_{bal}. One therefore does best by using as intense of a LO as possible. If the beamsplitter outputs are sensed by two independently powered photodetectors, each detector is susceptible to saturation from the static photocurrent generated by a strong LO ($P_{\mathrm{LO}}/2$ in Eqs. 3.19–3.21). If instead the photoreceivers are powered in series, as in Fig. 3.2, their static photocurrents offset, making them immune to saturation in balanced detection. The LO power can then, in principle, be arbitrarily large.
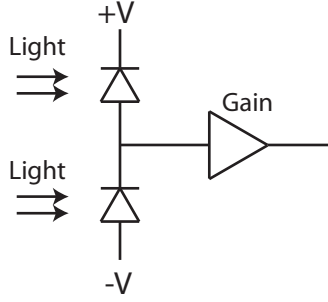
Figure 3.2: Schematic of a pair of photodiodes connected in series as part of a balanced-detection configuration.

In balanced homodyne detection, the LO phase angle can be set to maximally observe the applied modulation. In particular, the optimal θ_{LO} value for an applied amplitude ($\theta = 0$) and phase ($\theta = \pi$) modulation is $\pi/2$ and 0, respectively:

$$(\theta=0, \theta_{\mathrm{LO}}=\frac{\pi}{2}) : \langle I_{\mathrm{bal}}(t)\rangle = 2\sqrt{\epsilon}G\left[\sqrt{P_{\mathrm{LO}}P_s}+\sqrt{2P_{\mathrm{LO}}P_{\mathrm{mod}}}\cos(\omega_{\mathrm{mod}}\,t)\right], \quad (3.25)$$

$$(\theta=\pi, \theta_{\mathrm{LO}}=0) : \langle I_{\mathrm{bal}}(t)\rangle = 2\sqrt{\epsilon}G\left[\sqrt{2P_{\mathrm{LO}}P_{\mathrm{mod}}}\sin(\omega_{\mathrm{mod}}\,t)\right]. \quad (3.26)$$

However, balanced homodyne detection has the significant drawback of being sensitive to low-frequency amplitude noise present on the LO, as well as parasitic low-frequency noise in the detector's electric power source. Although ideally the LO and signal beams are combined on a perfect 50:50 beamsplitter, in practice the beamsplitter's outputs are never exactly equal in power. The residual power imbalance causes the beams' low-frequency amplitude noise, particularly that of the intense LO, to be mapped onto I_{bal}. For balanced homodyne detection, this amplitude noise, along with low-frequency electronic noise, overlaps in frequency with the modulation of interest. In the context of experiments described in this dissertation, operating in homodyne mode would mean attempting to accurately measure small optomechanical modulations, which barely rise above the signal beam's shot-noise floor, in a forest of technical noise.

Since noise tends to tail off as some function of frequency (*e.g.* the "1/f" noise), operating the balanced detector in heterodyne mode, with $\Delta_{\mathrm{LO},s} \gg 0$, makes it easier to measure signals with quantum-limited precision instead of classical-noise-limited precision. For that very reason, heterodyne detection was adopted as part of the experimental setup. Heterodyne measurements do come with one major disadvantage: there is a 50% reduction in detection efficiency when tracking one particular signal quadrature because the LO spends half its time "sensing" the incorrect quadrature. Contrary to homodyne detection, where θ_{LO} can be tuned to optimally detect a particular signal quadrature, in heterodyne detection the phase quickly raps a full 2π, at a rate $\Delta_{\mathrm{LO},s}$, which results in all quadratures being simultaneously detected.

Most of the central claims of experimental work presented as part of this dissertation are based on measurements of the balanced detector's photocurrent PSD. For a general balanced detector, the PSD of its photocurrent is given by

$$S_{\text{bal}}(\omega) = \frac{\left\langle \hat{\tilde{I}}_{\text{bal}}^\dagger(\omega') \hat{\tilde{I}}_{\text{bal}}(\omega) \right\rangle}{2\pi \tilde{\delta}(\omega' - \omega)}, \tag{3.27}$$

$$\frac{S_{\text{bal}}(\omega)}{G^2 P_{\text{LO}}} = \frac{(1-\epsilon)\hbar\omega_{\text{LO}}}{2\pi} + \frac{\epsilon}{2\pi\tilde{\delta}(\omega'-\omega)} \left\langle \left[\hat{\tilde{\zeta}}_s^\dagger(\omega'+\omega_{\text{LO}})e^{i\theta_{\text{LO}}} - \hat{\tilde{\zeta}}_s(-\omega'-\omega_{\text{LO}})e^{-i\theta_{\text{LO}}} \right] \right.$$
$$\left. \cdot \left[\hat{\tilde{\zeta}}_s(\omega+\omega_{\text{LO}})e^{-i\theta_{\text{LO}}} - \hat{\tilde{\zeta}}_s^\dagger(-\omega-\omega_{\text{LO}})e^{i\theta_{\text{LO}}} \right] \right\rangle, \tag{3.28}$$

which in homodyne configuration, for the LO and signal beams considered here, leads to

$$\frac{S_{\text{bal}}^{(\text{hom})}(\omega)}{G^2 P_{\text{LO}}} = \frac{\hbar\omega_{\text{LO}}}{2\pi} + \epsilon \left[4P_s \sin^2(\theta_{\text{LO}})\tilde{\delta}(\omega) \right.$$
$$\left. + P_{\text{mod}}[1 - \cos(2\theta_{\text{LO}} - \theta)] \cdot \left[\tilde{\delta}(\omega - \omega_{\text{mod}}) + \tilde{\delta}(\omega + \omega_{\text{mod}}) \right] \right], \tag{3.29}$$

and similarly in a heterodyne configuration yields

$$\frac{S_{\text{bal}}^{(\text{het})}(\omega)}{G^2 P_{\text{LO}}} = \frac{\hbar\omega_{\text{LO}}}{2\pi} + \epsilon \left[P_s \left[\tilde{\delta}(\omega - \Delta_{\text{LO},s}) + \tilde{\delta}(\omega + \Delta_{\text{LO},s}) \right] \right.$$
$$+ \frac{P_{\text{mod}}}{2} \left[\tilde{\delta}(\omega - \Delta_{\text{LO},s} - \omega_{\text{mod}}) + \tilde{\delta}(\omega - \Delta_{\text{LO},s} + \omega_{\text{mod}}) \right]$$
$$\left. + \frac{P_{\text{mod}}}{2} \left[\tilde{\delta}(\omega + \Delta_{\text{LO},s} - \omega_{\text{mod}}) + \tilde{\delta}(\omega + \Delta_{\text{LO},s} + \omega_{\text{mod}}) \right] \right]. \tag{3.30}$$

The $\hbar\omega_{\text{LO}}$ terms in Eqs. 3.28–3.30 represent the dominant LO's shot-noise ($P_{\text{LO}} \gg P_s, P_{\text{mod}}$), which does not subtract away in a balance measurement since vacuum fluctuations are uncorrelated. The remainder of the photocurrent's PSD is proportional to the signal beam's PSD. In the homodyne detection case (Eq. 3.30), the measured PSD is a copy of the power contained in quadrature $\theta = 2\theta_{\text{LO}} + \pi$ of the signal beam. In the heterodyne case (Eq. 3.30), the recorded PSD is an average of the signal beam's power distribution over all quadratures. The power distribution of the signal quadrature containing the modulation of interest, θ, can be isolated in a heterodyne measurement by first demodulating the balanced-detection photocurrent

at frequency $\Delta_{\text{LO},s}$:

$$\hat{I}_{\text{dem}}(t) = \hat{I}_{\text{bal}}(t) \times \sin(\Delta_{\text{LO},s}t + \theta_{\text{LO}} - \frac{\theta}{2}) \tag{3.31}$$

$$S_{\text{dem}}^{(\text{het})}(\omega) = \frac{\left\langle \hat{\tilde{I}}_{\text{dem}}^{\dagger}(\omega')\hat{\tilde{I}}_{\text{dem}}(\omega) \right\rangle}{2\pi\tilde{\delta}(\omega' - \omega)} \tag{3.32}$$

$$\frac{S_{\text{dem}}^{(\text{het})}(\omega)}{G^2 P_{\text{LO}}} = \frac{1}{2}\frac{\hbar\omega_{\text{LO}}}{2\pi} + \epsilon\left[P_s \sin^2(\theta)\tilde{\delta}(\omega) \right.$$
$$\left. + \frac{P_{\text{mod}}}{2}\left[\tilde{\delta}(\omega - \omega_{\text{mod}}) + \tilde{\delta}(\omega + \omega_{\text{mod}}) \right] \right], \tag{3.33}$$

Interestingly, the θ-quadrature PSD (Eq. 3.33) contains only half of the total detected shot-noise; the remaining half is mapped onto the orthogonal, $(\theta + \pi)$ quadrature. Consequently, the relative modulation-signal-to-shot-noise ratio in $S_{\text{dem}}^{(\text{het})}(\omega)$ is twice as large as that in $S_{\text{bal}}^{(\text{het})}(\omega)$. This advantageous signal-to-noise ratio (SNR) was used when attempting to sensitively measure externally applied forces, as detailed in Chapter 6.

Eqs. 3.27–3.33 apply for all real values of frequency ω, from $-\infty$ to ∞. However, spectrum analyzers typically only report positive frequencies when displaying PSDs. For the remainder of this dissertation, quoted PSDs will contain only positive frequencies; negative frequency components will be dropped.

Chapter 4

The experimental apparatus

*This chapter outlines the details of the experimental setup and the methods em-
ployed to conduct studies of optomechanics with ultracold atoms. The content builds
on the information provided in Tom Purdy's dissertation [50], in particular details re-
garding the construction of the experimental chamber and the atom chip, and the first
stages of experimental routines, which pertain to the preparation of atomic ensembles.*

The experiments discussed in this dissertation were based on similar experimental
sequences lasting ~ 30 to 35 seconds. Summarized briefly, these sequences started
with the capture of $\sim 10^7$ ^{87}Rb atoms emanating from a continuously powered getter
in a magneto-optical trap (MOT). Collected atoms were then referenced to an atom
chip by briefly releasing them from the initial MOT and re-capturing them in a dif-
ferent MOT, a UMOT, one whose magnetic field was in part produced by U-shaped
wires on the chip. Atoms were next optically pumped to the $|F = 2, m_F = 2\rangle$ state
and cooled via forced radio-frequency (RF) evaporation. Once cold, they were mag-
netically carried to a Fabry-Pérot cavity, termed "science cavity" and located ~ 2
cm away from the MOT region, by applying tailored currents to patterned "conveyor
belt" wires on the atom chip. Once at the cavity, atoms underwent a second round
of forced RF evaporation before being transfered to a far-off resonance trap (FORT)
formed by a standing wave of light inside the optical cavity. Atoms were then disper-
sively probed near their $|F = 2, m_F = 2\rangle \to |F = 3, m_F = 3\rangle$ closed cycling transition
(^{87}Rb D2 transition) with σ^+-polarized light, leading to optomechanical interactions,
before being released from their trap and imaged.

The material presented in this chapter deals with relevant information surrounding
the last stage of experimental sequences, when atoms were at the science cavity. Ear-
lier stages will be discussed only secondarily as part of the "experiment's checklist,"
which was developed to help diagnose problems with the MOT and atom prepara-
tion in general. Two experimental realizations are discussed in this dissertation: one
in which atoms were prepared in a single-color FORT, *i.e.* formed by only one trap
light ($\lambda_A = 850$ nm), and therefore collectively behaved as a single effective mechan-

ical element, and one in which atoms populated several lattice sites of a superlattice FORT, *i.e.* formed by two trap light beams ($\lambda_A = 861$ nm, $\lambda_B = 843$ nm), where each populated site served as a distinguishable mechanical element. The two realizations differed somewhat in construction, with the prime difference being the upgrade of two trap lasers in the multi-oscillator setup. Experimental details covered in this chapter will focus mostly on the more involved multi-oscillator construction.

4.1 The building blocks

The creation of a cold-atoms-based mechanical oscillator, followed by tailored optomechanical probing, required a carefully coordinated series of actions among six central building blocks: two trap (FORT) lasers, a probe laser, the science cavity, a "transfer" optical cavity, which served as a means to frequency reference the lasers and narrow their spectral emission, and a balanced heterodyne detector for the probe at the output of the science cavity. Information regarding each block is detailed in this section. The complete experimental lock chain, which includes interconnections among these building blocks, is discussed in the following section.

4.1.1 Science cavity

The theory of optical cavities is discussed in detail in Ref. [66]. In this section, I provide only a quick overview of certain key features relevant for the science cavity.

The place where optomechanics came to life during experiments was in the science cavity, a high-finesse Fabry-Pérot cavity. The cavity is composed of two highly reflective mirrors, with radius of curvature $R = 5$ cm, separated by a distance $L = 250\,\mu$m; it is a type of near-planar ($R \gg L$) stable resonator. The cavity admits particular transverse electromagnetic (TEM) modes of Hermite-Gaussian beams (see Fig. 4.1), with eigenfrequencies

$$\omega_{q,m,n} = \text{FSR}\left(q + (m+n+1)\frac{\arccos(g_{\text{cav}})}{\pi}\right), \tag{4.1}$$

where m and n are the horizontal and vertical orders of the eigenmodes ($\text{TEM}_{m,n}$), q is the longitudinal order of the eigenmodes and $g_{\text{cav}} = 1 - L/R = 0.995$ parametrizes the cavity. The cavity eigenmodes have a common beam waist size of

$$w_0^2 \sim \frac{\lambda}{\pi}\sqrt{\frac{RL}{2}} = (25\,\mu\text{m})^2, \tag{4.2}$$

where λ is the wavelength of the optical field. The spectrum of allowed TEM modes repeats every free spectral range, FSR:

$$\text{FSR} = \omega_{q+1,m,n} - \omega_{q,m,n} = c/(2L) = 2\pi \times 600\,\text{GHz}, \tag{4.3}$$
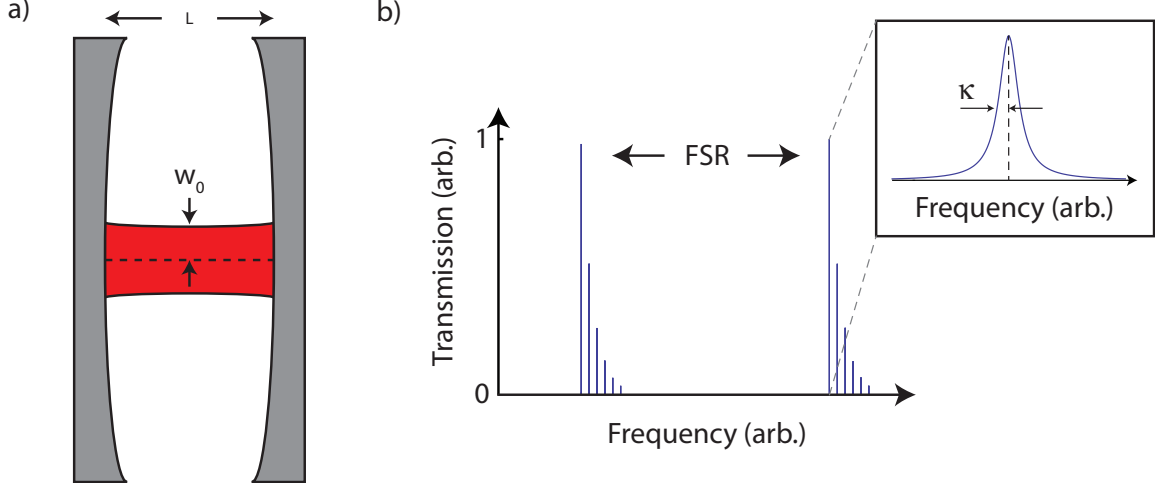
Figure 4.1: Near-planar Fabry-Pérot (FP) optical cavity. (a) Schematic of a FP cavity in near-planar configuration, with mirrors (solid grey) separated by a distance L. The transverse size of resonating beams varies only minutely between the center and the edges of the cavity, with waist w_0 relative to the longitudinal axis of the cavity (dashed line) (b) Transmission spectrum of a near-planar FP cavity. TEM modes are closely spaced in frequency (Eq. 4.1). (Inset) Magnified image of a $\text{TEM}_{0,0}$-mode transmission signal.

where c refers to the speed of light. In experiments discussed in this dissertation, all three lasers were adjusted to be resonant with a $\text{TEM}_{0,0}$ of the science cavity.

The FSR is related to the cavity's quality factor, also known as its finesse, $\mathcal{F}$, and the cavity's half-width at half-maximum (HWHM), κ:

$$\mathcal{F} = \frac{\text{FSR}}{2\kappa}. \tag{4.4}$$

The cavity mirrors' imperfections, specifically their transmission, $\mathcal{T}$, and loss, $\mathcal{L}$, coefficients, define $\mathcal{F}$:

$$\mathcal{F} = \frac{2\pi}{\mathcal{T}_1 + \mathcal{T}_2 + \mathcal{L}_1 + \mathcal{L}_2}. \tag{4.5}$$

Coefficients $\mathcal{T}$ and $\mathcal{L}$ can be understood as the probability that a photon be transmitted through a mirror or loss in a mirror's coating or substrate during one round-trip through the cavity. $\mathcal{F}$ thus reflects the likelihood of a photon reflecting off both mirrors and hence surviving a cavity round-trip. Both $\mathcal{F}$ and κ are wavelength dependent as the mirror coatings are designed to operate at one particular wavelength. For the science cavity, mirrors were designed to maximize the reflectivity in the vicinity of the ^{87}Rb D2 transition line ($\lambda = 780$ nm).

A cavity with $\mathcal{T}_1 = \mathcal{T}_2$ is referred to as a "balanced" or "two-sided" cavity, while a cavity with $\mathcal{T}_1 \neq \mathcal{T}_2$, is termed an "unbalanced" or "one-sided" cavity. The science

cavity is of the latter form; layers of reflective coating were removed from one of the mirrors prior to assembling the cavity (see Ref. [50]). Each cavity mirror's transmission at $\lambda = 780$ nm was individually measured during the construction phase of the experiment to be $\mathcal{T}_1 = 1.5 \times 10^{-6}$ and $\mathcal{T}_2 = 12 \times 10^{-6}$. After the experimental apparatus was completed, the total mirror losses, and hence the cavity finesse, at $\lambda = 780$ nm were determined using the method proposed by Christina Hood in Ref. [67] and employing the already known transmission ratio between both cavity mirrors ($\mathcal{T}_2/\mathcal{T}_1 = 8$): $\mathcal{L} = \mathcal{L}_1 + \mathcal{L}_2 = 25 \times 10^{-6}$ and $\mathcal{F} = 163,000$.

The half-linewidth, κ, was also measured at $\lambda = 780$ nm by cavity ringdown. The method essentially consists of measuring the cavity's impulse response function by inserting a delta-function-in-time light pulse into the cavity and measuring the light's exponential decay rate ($1/\tau_{\mathrm{decay}}$) out of the cavity:

$$\tau_{\mathrm{decay}} = \frac{1}{\pi \kappa}. \tag{4.6}$$

A delta-function-like pulse was generated by very quickly sweeping the laser light across the cavity resonance in frequency space. This could have in principle been done by rapidly varying the laser frequency. Instead, the laser frequency was kept fixed and the science cavity length was quickly modulated, thereby modulating the cavity resonance frequency. This modulation was done by applying a strong oscillating tone to one of the cavity mirrors' piezoelectric tube. The measurement yielded $\kappa = 2\pi \times 1.82$ MHz.

4.1.2 CQED parameters

The intensity-averaged volume occupied by $\mathrm{TEM}_{0,0}$ modes in a near-planar cavity is given as

$$V_{\mathrm{m}} = \frac{\pi}{4} w_0^2 L. \tag{4.7}$$

The dipole moment for the $|F = 2, m_F = 2\rangle \rightarrow |F = 3, m_F = 3\rangle$ closed cycling transition in ^{87}Rb is $d = 2.53 \times 10^{-29}$ C·m. When applied to the science cavity, with probe light near $\lambda = 780$ nm, these properties lead to a maximum probe-atom interaction rate of $g_o = 2\pi \times 13.1$ MHz. This rate far exceeds κ and the atomic D2 transition full-linewidth, $\Gamma = 2\pi \times 6.07$ MHz, which means that every photon scattered by the atomic ensemble during experiments was most likely to remain within its $\mathrm{TEM}_{0,0}$ science cavity mode. This scattering condition is parametrized by the CQED cooperativity, $C = g_o^2/\kappa\Gamma = 15.7$. Since $C > 1$, the experimental apparatus is said to operate in the "single-photon strong-coupling" regime.
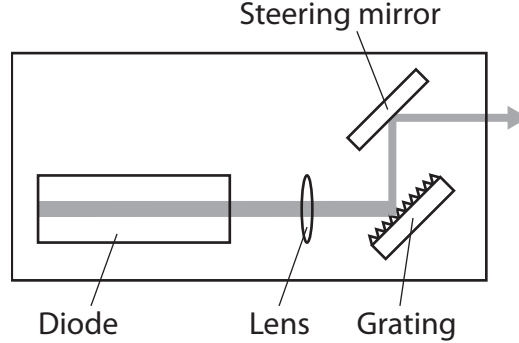
Figure 4.2: Schematic of a typical extended-cavity diode laser in Littrow configuration. The wider beam between the diode and the grating represents the overlap of the diode's emission and the grating's first-order diffraction mode.

4.1.3 Lasers

DL Pro tunable diode lasers from Toptica Photonics[1] were used for the probe and FORTs. These lasers are a type of tunable external-cavity diode lasers in Littrow configuration [69] (Fig. 4.2).

The basic principle underlying the operation of extended-cavity diode lasers is the partial reflection of emitted light back into the laser diode to maintain stimulated emission of photons, and hence stabilize the laser at one particular wavelength. In the case of Littrow configurations, this partial reflection is ensured by a diffraction grating, a periodically structured optical component which generates constructive optical interferences at wavelength-dependent angles, θ:

$$\theta_r = \arcsin\left(\frac{r\lambda}{d_s} - \sin\theta_i\right), \tag{4.8}$$

where d_s defines the spatial period of the structure (*e.g.* the spacing between slits in a multi-slit grating), r is an integer that quantizes the output grating angle θ_r, and θ_i is the incidence angle of the light beam on the grating surface. The angle of the diffraction grating is adjusted such that $r = 1$ diffraction order reflects back into the laser diode ($\theta_1 = 0$), while the more intense $r = 0$ diffraction order is allowed to exit the laser housing and serve as the experimentally useable laser source. This condition is met when $\theta_i = \arcsin\left(\frac{\lambda}{d_s}\right)$. The use of an AR-coated laser diode in this setup is particularly important: it prevents partial reflections from the diode's external facet, which would compete with the grating-provided reflection into the diode and hamper the overall stability of the system.

Optical feedback alone is generally not sufficient to maintain an extended-cavity diode laser's coherence for a long period of time. Additional sources of decoherence

---

[1]Ref. [68] offers a great description of these lasers and some of the theory behind them.

that must be overcome include nanometer-scale displacement drifts of the partially reflecting element and electronic noise in the diode's current source. Active electronic feedback based on the external measurement of the laser's frequency is therefore necessary to finely regulate the laser's emission, and hence maximize the coherence of its stimulated emission process. In the experimental setup described here, this stabilizing feedback stemmed from Pound-Drever-Hall (PDH) locks to the transfer cavity[2]. Each of the three lasers were individually stabilized by feeding back PDH-lock signals through two separate loops using Toptica Photonics' Fast Analog Linewidth Control (FALC 110): measurements of low-frequency drifts were sent to the piezoelectric device that controls the diffraction-grating angle, while high-frequency fluctuations were canceled by being returned to the diode's current source.

Under optimal operating conditions, this setup enabled laser frequency linewidths below 10 kHz. In other words, stimulated photons emitted $100\,\mu s = 1/(10\,\text{kHz})$ apart from each other remained correlated. This achievement was important as it significantly reduced noise near the mechanical oscillation frequency of trapped atoms ($\omega_m \sim 2\pi \times 120$ kHz), thereby minimizing optically induced heating of the atomic motion [49]. The lasers' overall quietness however hinged on the quality of their diodes. It turns out that many off-the-shelf AR coated diodes do not achieve the optimal, sub-10-kHz operating condition. It also turns out that Toptica Photonics has a dedicated unit to test and screen available laser diodes, and include only those that meet the stringent specifications as part of their DL Pro package. As a word of advice to future users of the experimental apparatus, I suggest you opt for Toptica's laser diodes instead of low-price diodes to ensure quality performance.

4.1.4   Transfer cavity

A Toptica Photonics' FPI 100, a confocal[3] ($R = L = 7.5$ cm) Fabry-Pérot interferometer with FSR = 1 GHz and κ near 1 MHz for the probe (780 nm) and trap (near 850 nm) wavelengths, was used as the transfer cavity. The cavity was placed inside an evacuated chamber and was both temperature stabilized and vibration isolated to maintain its length and position constant.

Temperature control was achieved via a thermoelectric cooler (TEC) sandwiched between the transfer cavity and a copper slab thermally connected to the vacuum chamber by a few thin copper ribbons. In this setup, the vacuum chamber served as a large temperature reservoir. The temperature gradient produced by applying a current to the TEC was kept absolutely constant during experiments by an active feedback on the applied TEC current, as detailed in Section 4.2.1 in the context of the overall system's lock chain. The entire cavity-to-copper stack sat on pieces of Sorbothane (the brand name of a viscoelastic polymer used for mechanical damping)

---

[2]Details regarding the theory of PDH frequency stabilization is provided in Ref. [70].

[3]For a confocal cavity, FSR = $c/\left(4L\right)$.
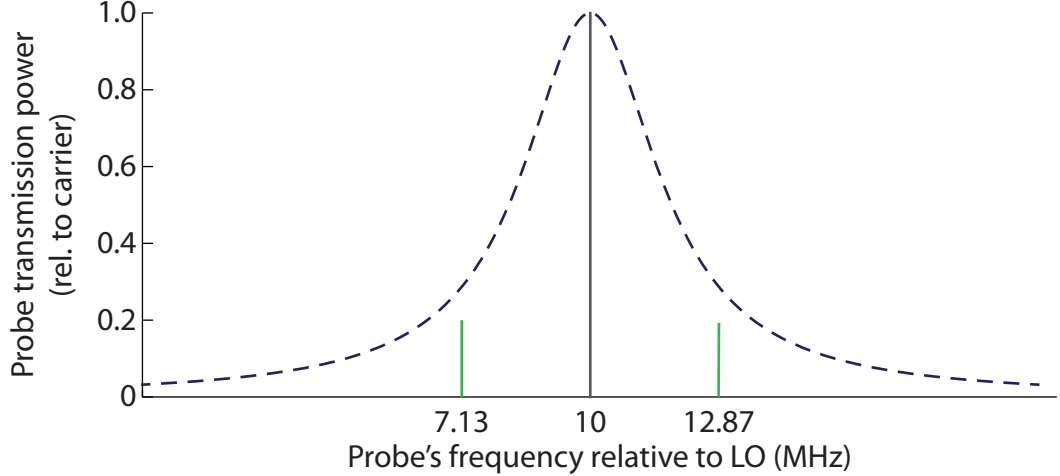
Figure 4.3: Schematic of the heterodyne-detected probe power spectrum in transmission of the science cavity during typical experiments. The probe carrier (gray) is depicted as being resonant with the science cavity, with the EOM-applied sidebands (green) symmetrically detuned from cavity resonance and $\sim 1/5$ of the carrier power. The science cavity lorentzian lineshape (dashed blue) is shown for reference.

that acted as a low-pass vibration filter, keeping the cavity isolated from ground vibrations.

4.1.5 Balanced heterodyne detector

The theory of balanced detection is discussed in Chapter 3.

Detection of the probe in transmission of the science cavity was done by heterodyne detection with an optical local oscillator (LO) on a NewFocus 80-MHz balanced photoreceiver. The two beams, the probe and LO, originated from a common laser source, the probe laser, and were separated using a polarizing beamsplitter (PBS), with most of the light directed on the LO path, which circumvented the science cavity. The LO power was stabilized to yield 1 mW at the heterodyne detector, which enabled the probe to be detected with shot-noise limited sensitivity. The small remaining fraction of laser light formed the probe and was sent to the science cavity. The probe was offset in frequency by $\Delta_{\mathrm{LO},p} = \omega_p - \omega_{\mathrm{LO}} = 2\pi \times 10$ MHz from the LO using a pair of oppositely diffracting AOMs on the cavity-bound path (see Fig. 4.4). In addition, small sidebands were applied on the probe by placing a resonant EOM, with resonance frequency $\omega_{\mathrm{mod}} = 2\pi \times 2.87$ MHz $\sim 1.6\,\kappa$, on the probe path. These sidebands served only as frequency markers; it is the carrier that acted as the optomechanical probe, with a mean number of intracavity photons, $\bar{n}$, near unity. The sidebands added a negligible amount of incoherent heating during probing, and mu-

tually cancelled their optomechanical effects (*e.g.* $\Gamma_{\rm opt}$, $\omega_{\rm opt}$) since they were detuned by an equal amount to the blue and red of cavity resonance during experiments (the probe carrier was set to be on resonance - see Fig. 4.3).

Powering the two oppositely diffracting AOMs and the resonant EOM required three separate radio-frequency (RF) sources. Two more function generators were used to demodulate the heterodyne-detected LO-probe beats for active control of certain probe properties (more details in Section 4.2.3). Since demodulation hinges on having electronic local oscillators with constant phases, the phases of all five frequency sources were locked to a "master" function generator. The master generator also clocked GageScope, the computer-based system with which experimental data was recorded.

4.2   Lock chain

The integration of all five building blocks into a single, orchestrated unit was experimentally challenging. It required developing a network of eleven active feedback loops, involving both optical and electronic connections, as shown in Fig. 4.4. The specifics about the transfer-cavity and science-cavity feedback circuits, and the procedure followed to lock the entire system are discussed in this section.

A common theme in many of the coming subsections is the overlapping of cavity resonances, specifically the $\text{TEM}_{0,0}$ cavity modes corresponding to the probe, laser A and laser B. What does that mean exactly? It does *not* mean overlapping them in frequency, since all three lasers have widely different optical frequencies. Instead, "overlapping" refers to adjusting the lasers' optical frequencies so as to make them all resonant with a $\text{TEM}_{0,0}$ cavity mode at one common cavity length. This is achieved by choosing three $\text{TEM}_{0,0}$ modes, one for each laser, that are spaced by an integer multiple of the cavity's FSR. For example, if the probe frequency is set to $\omega_p = 2\pi \times 384.188$ THz ($\Delta_{\rm ca} \sim -2\pi \times 40$ GHz) and the cavity length happens to yield a cavity FSR exactly equal to $2\pi \times 600$ GHz, then plausible resonant frequencies for lasers A and B are $\omega_A = 2\pi \times (384.188 - 60 \times 0.600)\text{THz} = 2\pi \times 348.188$ THz and $\omega_B = 2\pi \times (384.188 - 48 \times 0.600)\text{THz} = 2\pi \times 355.388$ THz.

4.2.1   Laser-transfer cavity locks

Three of the control loops were designed to reduce the level of technical phase noise of the trap and probe lasers' emission by PDH locks, described in Section 4.1.3. A few tens to hundreds of microwatts were picked off from each laser output and fiber-coupled to the transfer cavity area. The signals from laser B and the probe were sent through fiber-based wide-frequency-band electro-optic modulators (EOMs) from EO Space to produce sideband tones. These sidebands provided the necessary degrees of freedom to simultaneously overlap all three lasers on both the science and
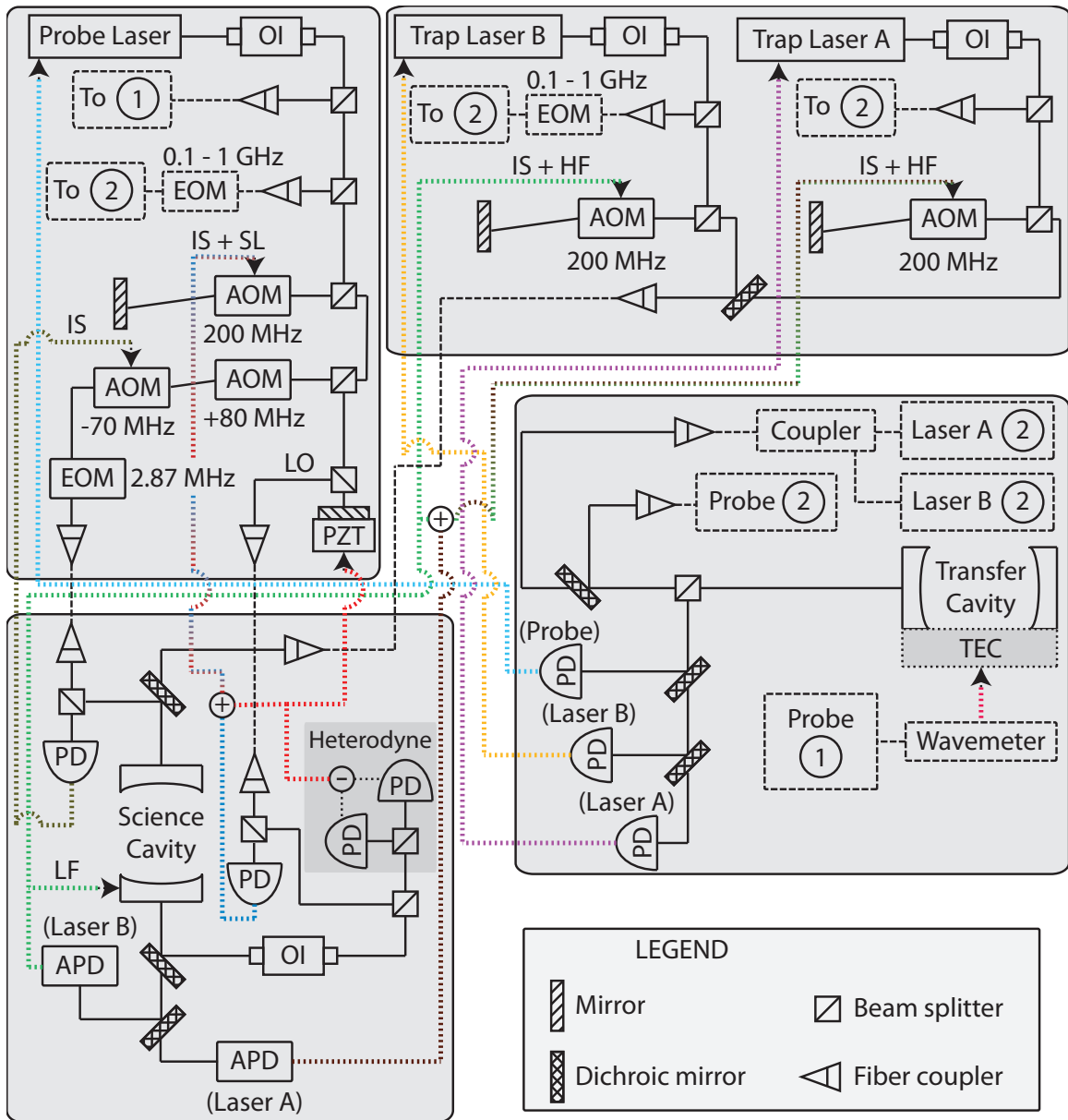
Figure 4.4: Experimental lock chain. The schematic highlights the free-space (solid line) and fibered (dashed line) optical paths of each laser, along with the many electronic feedback connections (dotted lines - color). For clarity, certain components have been omitted from the schematic including electronic control systems, wave plates and function generators. Definition of acronyms: OI - optical isolator; EOM - electro-optic modulator; AOM - acousto-optic modulator; TEC - thermoelectric cooler; PZT - piezo-electric transducer; PD - photodiode; APD - avalanche photodiode; IS - intensity stabilization; SL - "sidelock," which refers to the probe's frequency lock relative to the science cavity resonance; HF - high-frequency lock; LF - low-frequency lock.

transfer cavities. Indeed, overlapping three lasers on two separate cavities requires six different frequencies, which can only be attained if at least five frequencies are tunable. In the experiments discussed here, the five degrees of freedom were the center frequencies of all three lasers and the RF frequencies powering the two fiber-based EOMs.

The phase modulation necessary to produce a dispersive error signal in reflection of the transfer cavity was applied directly on the diodes of laser A and B. The same was not done on the probe to avoid having the applied modulation impact the dispersive interaction with atoms at the science cavity. Instead, the probe's PDH modulation was applied via the in-fiber EOM, by mixing the modulation tone with the EOM's RF signal. In all cases, the feedback was applied to the laser using Toptica's FALC 110 (see Section 4.1.3).

In addition to narrowing the spectral emission of each laser, these three lock loops also pegged each laser's optical frequency to the transfer cavity and, by extension, to each other. The lasers would therefore commonly follow any changes in the transfer cavity lengths, whether intended or not. Conversely, the laser frequencies could be kept fixed by actively maintaining the cavity length constant. In particular, the probe's detuning from atomic resonance, Δ_{ca}, a critical element of the optomechanical coupling strength g_{OM}, could be stabilized to a desired value. This capability was included in the experimental setup by monitoring the probe's emission frequency on a Toptica Photonics' High Finesse Wavelength Meter, termed "wavemeter," and applying a proportional-integral (PI) feedback signal to the transfer cavity's TEC to hold the probe's frequency constant. The feedback was digitally computed, the only digital control circuit in the entire lock chain.

4.2.2 Intensity and science cavity locks

As was done for the laser locks to the transfer cavity, all three laser beams were simultaneously overlapped on the science cavity. This time, however, the laser carriers were directly overlapped, by tuning their respective frequency, instead of relying on EOM-produced sideband tones. Since all three lasers were referenced to each other via their respective lock to the transfer cavity, maintaining this common overlap on the science cavity required referencing only one laser to the science cavity. The probe would have been a poor choice to fulfill that role. The ability to sweep the probe independently of the cavity, to tune in real time the probe-cavity detuning, Δ, and to turn off the probe completely are desirable experimental abilities that could not have been possible if the probe was locked to the science cavity. Instead, one of the trap lasers, laser B, was used to chain the laser system to the science cavity. Note that in the single-oscillator work, only laser A was used, so it served as the laser system's chain link to the science cavity.

The locking technique was similar to a PDH lock. A dispersive error signal was generated by detecting the phase modulation applied on laser B's diode as part of the

transfer cavity lock (Section 4.2.1) in transmission of the science cavity instead of in reflection. Although not technically correct, I will term this method "transmission-PDH." It is important to note that even though the same applied phase modulation was used in two different feedback loops, the information recorded in each loop was distinct. The transmission-PDH lock's low-frequency information was used to stabilize the science cavity's mirror separation; the high-frequency information was fed back to laser B's AOM and fed forward to laser A's AOM. This feedback-feedforward combination was made possible by powering both AOMs with a common voltage source, and using the same Bragg diffraction order in both double-pass AOM setups. I note that feeding high-frequency information to lasers A and B had a marginal impact on the atoms. As detailed later in the dissertation, the temperature and lifetimes of optically trapped atoms were observed to be dominantly influenced by the level of noise on the two trap lasers' emission.

As described in Section 4.4, the oscillation frequency of atoms-based mechanical elements is determined by the trap lasers' intracavity intensity. Similarly, the strength of atoms-probe optomechanical coupling is proportional to the mean number of intracavity probe photons, $\bar{n}$. Control over each laser's intracavity intensity is therefore necessary. For the trap lasers, this control was experimentally achieved by stabilizing their respective science-cavity-transmitted optical power to a computer-controlled set-point. The optical trap depth could therefore be optimally adjusted in real time over the course of experimental routines. For the probe, a more elaborate construction was used, one that also provided control over Δ. The maximum number of intracavity probe photons, $n_{\max}$, obtained when placing the probe directly on science cavity resonance, was controlled by picking off a small fraction of light before the probe enters the cavity and actively stabilizing the pick-off's power to a desired level. This method was successful in part because the input coupling into the science cavity was observed to remain constant over several days. The actual intracavity probe photon number, $\bar{n}$, was determined and set using the balanced heterodyne detector. Independent control of $n_{\max}$ and $\bar{n}$ also defined Δ based on the science cavity's lorentzian lineshape:

$$\Delta = \kappa \sqrt{\bar{n}/n_{\max} - 1}. \tag{4.9}$$

After-the-fact measurements of Δ were made on each experimental iterations using the recorded heterodyne signal. Details surrounding the active stabilization of $\bar{n}$ and Δ are presented in the coming subsection.

4.2.3 The heterodyne-detector-based locks

Since equally-spaced frequency markers were placed on the probe, active control of Δ, and by extension $\bar{n}$, could have in principle been accomplished using a heterodyne-detector-based transmission-PDH lock with a tunable offset. This would have required two consecutive demodulations: first at the probe-LO detuning ($\Delta_{\text{LO},p} = 2\pi \times 10$

MHz), and then at the EOM modulation frequency ($\omega_{\text{mod}} = 2\pi \times 2.87$ MHz). However, in practice, the signal-to-noise ratio (SNR) following the double demodulation was simply too small to produce a reliable lock. The limitations were the *very* small amount of detected sideband power, usually below 1 pW, and the relatively considerable amount of noise added at the different amplification and demodulation stages following heterodyne detection.

Instead, Δ and $\bar{n}$ were set by actively controlling the frequency of the RF signal powering the "200 MHz AOM," which importantly was common to both the probe and LO, so as to maintain the lower-frequency sideband at a set intensity. This approach required two parallel demodulations rather than two consecutive demodulations. The clearest explanation I can offer starts with a mathematical expression of the system's heterodyne photocurrent in the absence of optomechanics (*i.e.* without atoms present in the science cavity), which comes from Eq. 3.24:

$$
\begin{aligned}
I_{\text{bal}}(t) \;=\; & \sqrt{\epsilon}G\sqrt{P_{\text{LO}}} \cdot \Big[2\sqrt{P_p}\sin\left(2\pi \times 10\,\text{MHz} \cdot t + \theta_{\text{LO}}\right) \\
& + \sqrt{P_{\text{mod}}}\sin\left(2\pi \times 12.87\,\text{MHz} \cdot t + \theta_{\text{LO}}\right) \\
& + \sqrt{P_{\text{mod}}}\sin\left(2\pi \times 7.13\,\text{MHz} \cdot t + \theta_{\text{LO}} - \theta\right) \Big],
\end{aligned}
\tag{4.10}
$$

where ϵ is the detection efficiency, G is the detection gain, θ_{LO} is the relative phase offset between the LO and probe carrier, θ defines the phase of the applied modulation, and P_{LO}, $P_p = 2\kappa\hbar\omega_p\bar{n}$ and P_{mod} are the LO, probe carrier and probe sideband powers, respectively. The latter two powers are related by the depth of the EOM modulation, η: $P_{\text{mod}} = \eta \cdot P_p$. In order to observe and eventually stabilize the amplitude of the lower-frequency sideband, one must have a good handle on θ_{LO}, which is to say that the relative path length difference between the LO and probe should be kept constant via active control. Experimentally, this control was achieved by demodulating $I_{\text{bal}}(t)$ at 10 MHz,

$$
\begin{aligned}
I_{\text{dem}}^{(1)}(t) \;&=\; I_{\text{bal}}(t) \cdot \cos(2\pi \times 10\,\text{MHz} \cdot t), \tag{4.11}\\
&=\; \sqrt{\epsilon}G\sqrt{P_{\text{LO}}P_p}\sin(\theta_{\text{LO}}) + (\text{higher frequency terms}), \tag{4.12}
\end{aligned}
$$

and locking $I_{\text{dem}}^{(1)}(t)$ to zero, thereby fixing $\theta_{\text{LO}} = 0$, by stabilizing the position of a retro-reflection mirror on to the LO path (see Fig. 4.4). The amplitude of the lower-frequency sideband could then be isolated by applying a second, parallel demodulation to $I_{\text{bal}}(t)$, at 7.13 MHz, with a very specific phase:

$$
\begin{aligned}
I_{\text{dem}}^{(2)}(t) \;&=\; I_{\text{bal}}(t) \cdot \sin(2\pi \times 7.13\,\text{MHz} \cdot t - \theta), \tag{4.13}\\
&=\; \sqrt{\epsilon}G\frac{\sqrt{P_{\text{LO}}P_{\text{mod}}}}{2} + (\text{higher frequency terms}). \tag{4.14}
\end{aligned}
$$

Stabilizing $I_{\text{dem}}^{(2)}(t)$ to a computer-controlled setpoint thus stabilized P_{mod}, which for a constant η also fixed P_p and, by extension, $\bar{n}$. This rather involved method of controlling $\bar{n}$ was referred to as "sidelocking."
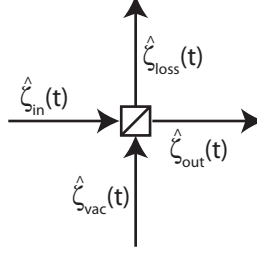
Figure 4.5: Beamsplitter model for any loss mechanism on an optical path. The output optical signal's electric field, $\hat{\zeta}_{\text{out}}$, is related to that of the input, $\hat{\zeta}_{\text{in}}$, based on the transmission efficiency, ϵ: $\hat{\zeta}_{\text{out}} = \sqrt{\epsilon}\hat{\zeta}_{\text{in}} + \sqrt{1-\epsilon}\hat{\zeta}_{\text{vac}}$. The electric field terms $\hat{\zeta}_{\text{vac}}$ and $\hat{\zeta}_{\text{loss}}$ refer to vacuum fluctuations and the loss channel, respectively.

The probe's detuning, Δ, was monitored during experimental runs by comparing the mean number of transmitted photons in the red, $\bar{n}_{\text{sb},r}$, and blue, $\bar{n}_{\text{sb},b}$, sidebands:

$$\Delta = \frac{R+1}{R-1}\omega_{\text{mod}} - \sqrt{\frac{4R\omega_{\text{mod}}^2}{(R-1)^2} - \kappa^2}, \tag{4.15}$$

where $R = \bar{n}_{\text{sb},r}/\bar{n}_{\text{sb},b}$ and $\omega_{\text{mod}} = 2\pi \times 2.87$ MHz is the EOM modulation frequency. As described in Chapters 5 and 6, both the single- and multi-oscillator experiments were designed to operate with the probe on cavity resonance. Post-selection ensured that only data with Δ within $\pm$ 200 kHz $\sim \pm\kappa/10$ were kept for analysis.

4.3 Detection efficiency

Every source of optical power loss between the cavity and the detector must be accounted for when determining the heterodyne detection efficiency. Fortunately, every loss mechanism, regardless of its nature, can be modeled as light exiting the incorrect port of a beam splitter and being replaced by an equivalent fraction of optical vacuum fluctuations (Fig. 4.5). The overall detection efficiency is thus like placing a series of beam splitters along the optical path, one for every channel of optical loss, and then taking the product of their respective efficiency.

In the experimental setup, four different sources of loss were labeled for the probe photons. The first concerned the efficiency with which intracavity photons would exit the transmission port of the science cavity:

$$\epsilon_{\text{cav}} = \frac{\mathcal{T}_2}{\mathcal{T}_1 + \mathcal{T}_2 + \mathcal{L}_1 + \mathcal{L}2} = \mathcal{T}_2\frac{\mathcal{F}}{2\pi} = 0.32. \tag{4.16}$$

The inability to collect more photons from the one-sided science cavity was the main source of loss in the detection chain. The second efficiency grouped the entire optical

path between the science cavity and balanced detector. The dominant sources of loss in that path were an optical isolator, inserted to prevent photons from being reflected back to the science cavity, polarizing beamsplitters and dichroic mirrors. Combined, these elements yielded a path efficiency of $\epsilon_{\text{path}} \sim 0.60$. The third efficiency, termed "mode-matching" efficiency, measured the spatial overlap of the LO and probe's respective gaussian mode at the heterodyne detector. Optimizing this efficiency was not only a matter of aligning their wavevectors, but also making sure that their intensity profiles were as identical as possible. Characterizing the mode-matching efficiency, ϵ_{mm}, was done by comparing the root-mean-squared (RMS) value of the measured LO-probe beat power, P_{RMS}, relative to their respective optical powers at the detector (P_{LO} and P_p - recall Eq. 3.24):

$$\epsilon_{\text{mm}} = \frac{P_{\text{RMS}}^2}{2P_{\text{LO}}P_p} = \frac{V_{\text{RMS}}/G_{\text{TI}}}{2P_{\text{LO}}P_p} \sim 0.80, \tag{4.17}$$

where V_{RMS} is the RMS voltage of the heterodyne-detected LO-probe beat, as measured on an impedance-matched device, and G_{TI} is the transimpedance gain of the balanced photodetector at the matched impedance. The fourth and final efficiency was the quantum efficiency of the NewFocus 80-MHz balanced photoreceiver, that is the number of electrons produced for every photon detected. The photoreceiver's specifications, in particular its quoted responsivity, indicated a quantum efficiency of $\epsilon_{\text{q}} = 0.8$.

The experimental setup's overall detection efficiency was therefore given as $\epsilon = \epsilon_{\text{cav}} \cdot \epsilon_{\text{path}} \cdot \epsilon_{\text{mm}} \cdot \epsilon_{\text{q}} \sim 0.12$. On good days, this compounded efficiency could reach 0.15, while on bad days it could drop to as low as 0.09. The overall detection efficiency was commonly termed the homodyne detection efficiency to distinguish it from the effective heterodyne detection efficiency. The latter applied when demodulating the LO-probe beat to look at a particular quadrature of the probe signal, which as explained in Section 3.2 would lead to a 50% reduction in efficiency.

4.4   Far off-resonance optical dipole trap (FORT)

The concept of optical trapping of particles was pioneered in the 1980s. Two architectures were simultaneously developed, one focused on biological structures [71, 72, 73], for which optical traps were termed "optical tweezers," and the other, on neutral atoms [16]. Today, far off-resonance optical dipole traps (FORTs) are common occurrences in cold-atom experiments, including CQED experiments [28, 29, 51, 74]. Extensive descriptions of the theory behind optical traps can be found in many textbooks [43, 53, 75, 76] and review articles [77]. In this section, I will first outline a few basic concepts regarding optical trapping and, in the process, present the one-color FORT used for the single-oscillator experiments (Chapter 5). I will then expand on

these concepts to introduce the two-color FORT used for the multi-oscillator experiments (Chapter 6).

4.4.1   FORT with a single color of light

An optical trapping potential arises from a trap light's induced dipole moment on an atom, the same effect that contributed to the probe-induced energy splitting between dressed states in Chapter 2. The effect is known as the AC Stark shift. For a trap light that is far-detuned from an atomic transition, $|\Delta_\text{ta}| \gg \Gamma$, the AC Stark shift leads to a dipole potential, U_dip, of the form

$$U_\text{dip} = \frac{\hbar\Gamma}{8} \frac{\Gamma}{\Delta_\text{ta}} \frac{I_t}{I_\text{sat}}, \tag{4.18}$$

where I_t is the trap light intensity, $I_\text{sat} = \hbar\omega_a^3\Gamma/(12\pi c^2)$ is the saturation intensity of the atom's closed cycling transition, and ω_a and Γ are the frequency and full-linewidths of the atomic transition. In the single-oscillator experiments, linearly polarized light from laser A significantly red-detuned from both the D1 and D2 ^{87}Rb transitions ($\Delta_\text{ta} < 0$) was used to confine atoms prepared in the $|F = 2, m_F = 2\rangle$ state. The atoms therefore experienced a total dipole potential, U_t, given by

$$U_t \;\; = \;\; \frac{\hbar I_t}{8} \left(\frac{1}{3} \frac{\Gamma^2}{\Delta_\text{ta}I_\text{sat}} \bigg|_\text{D1} + \frac{2}{3} \frac{\Gamma^2}{\Delta_\text{ta}I_\text{sat}} \bigg|_\text{D2} \right), \tag{4.19}$$

The factor of 1/3 and 2/3 for the D1 and D2 transitions, respectively, comes from the Clebsch-Gordon (CG) coefficients, c_CG, for optical transitions in ^{87}Rb. Information regarding I_sat and Γ for ^{87}Rb, as well as the the D1 and D2 transition frequencies can be found in Ref.[78].

Eq. 4.18 shows that the spatial dependence of U_dip is the same as that of I_t. Here, each FORT was created with a TEM$_{0,0}$ modes of the science cavity, which has a sinusoidally varying intensity pattern along the cavity. The dipole potential produced by laser A's emission alone therefore had the form

$$U_t(z) = U_A \sin^2(k_A z + \phi_A), \tag{4.20}$$

where U_A and k_A refer to potential depth and wavenumber of laser beam A, respectively. The angle ϕ_A captures the offset between the intensity standing wave of beam A relative to the intensity standing wave of the probe, an offset caused by both science-cavity mirrors having different reflectivity at wavelengths λ_A and λ_p.

Atoms deposited into the single-color FORT became trapped at locations where $U_t(z)$ was at a minimum. Since $\Delta_\text{ta} < 0$ during experiments, atoms were attracted to

locations of maximum optical intensity, $z_{\min,j}$:

$$\left.\frac{dU_t(z)}{dz}\right|_{z=z_{\min,j}} = 0, \tag{4.21}$$

$$z_{\min,j} = \frac{1}{k_A}\left(\frac{(2j+1)\pi}{2} - \phi_A\right), \tag{4.22}$$

where j indexes the potential minima, *i.e.* the lattice sites, and takes on real positive integers. Under typical experimental conditions, trapped atoms had a temperature of 2.5 to 5 μK, while the FORT had a potential depth of $|U_t| \sim k_B \cdot 50\,\mu$K, where k_B is the Boltzmann constant. Atoms were therefore tightly confined in potential minima, deep below the upper edge of the potential and with minimal excursions about their respective potential minimum. Each atom's effective potential could therefore be expressed as a low-order expansion of Eq. 4.20 about its equilibrium point, $z_{\min}$:

$$\begin{aligned} U_t(\hat{z}_i) = & \; U_A \sin^2(k_A z_{\min} + \phi_A) + U_A k_A \sin\left(2(k_A z_{\min} + \phi_A)\right)\hat{z}_i \\ & +U_A k_A^2 \cos\left(2(k_A z_{\min} + \phi_A)\right)\hat{z}_i^2, \end{aligned} \tag{4.23}$$

where $\hat{z}_i$ refers to each atom's displacement about $z_{\min}$. The first term in Eq. 4.23 gives the constant energy offset of each trap minimum. This offset was negative during experiments since $\Delta_{\text{ta}} < 0$. The second term describes the linear coupling between each atom's motion and the trap potential. The prefactor to $\hat{z}_i$, equal to $dU_t(\hat{z}_i)/d\hat{z}_i|_{\hat{z}_i=0}$, follows from Eq. 4.21 and is therefore identically 0. Finally, the third term expresses the trap's potential curvature at location $z_{\min}$. This quadratic dependence on motion relates to each atom's harmonic motion and hence defines each atom's motional oscillation frequency:

$$\frac{m}{2}\omega_{m,i}^2\,\hat{z}_i^2 = U_A k_A^2 \cos\left(2(k_A z_{\min} + \phi_A)\right)\hat{z}_i^2, \tag{4.24}$$

$$\omega_{m,i} = \omega_m = \sqrt{\frac{-2U_A k_A^2}{m}}. \tag{4.25}$$

Every atom, regardless of its location in the FORT, therefore had the same oscillation frequency, ω_m.

Published results pertaining to optomechanical probing of the atoms' collective CM motional mode, where only laser A was used to form the FORT ($\lambda_A = 850$ nm), were obtained with $\omega_m = 2\pi \times 110$ kHz, though the experimental setup had sufficient trap light power to reach $\omega_m = 2\pi \times 200$ kHz. In any case, the setup operated in the unresolved-sideband regime, where $\omega_m \ll \kappa$ (see Appendix A).

4.4.2 FORT with two colors of light

The objective in creating a FORT with two different colors of light is to produce a superlattice, that is a lattice whose amplitude is spatially modulated due to beats

between the intensity profiles of each light beams [79]. Experimental work involving an array of atoms-based mechanical elements was done using an optical superlattice formed by linearly polarized light from lasers A and B, with $\lambda_A = 862$ nm and $\lambda_B = 843$ nm, respectively. Both lasers were therefore significantly red-detuned from the D1 and D2 transitions of ^{87}Rb. The total dipole potential experienced by atoms in this case was given by extensions of Eqs. 4.19 and 4.20:

$$U_t(z) \ = \ \sum_{\text{A,B}} \frac{\hbar I_t(z)}{8} \left(\frac{1}{3} \frac{\Gamma^2}{\Delta_{\text{ta}} I_{\text{sat}}} \Big|_{\text{D1}} + \frac{2}{3} \frac{\Gamma^2}{\Delta_{\text{ta}} I_{\text{sat}}} \Big|_{\text{D2}} \right), \qquad (4.26)$$

$$U_t(z) \ = \ U_A \, \sin^2(k_A z + \phi_A) + U_B \, \sin^2(k_B z + \phi_B), \qquad (4.27)$$

where A and B label the two different colors of light.

No analytic expression for the locations of potential minima in this optical superlattice exists; only a transcendental relationship can be obtained:

$$\frac{dU_t(z)}{dz} \Big|_{z=z_{\min,j}} \ = \ 0, \qquad (4.28)$$

$$U_A k_A \, \sin\left(2(k_A z_{\min,j} + \phi_A)\right) + U_B k_B \, \sin\left(2(k_B z_{\min,j} + \phi_B)\right) \ = \ 0. \qquad (4.29)$$

However, a low-order approximation of the FORT potential near each atom's potential minimum, $z_{\min}$, can still be derived:

$$\begin{aligned}
U_t(\hat{z}_i) \ = \ & U_A \, \sin^2(k_A z_{\min} + \phi_A) + U_B \, \sin^2(k_B z_{\min} + \phi_B) \qquad\qquad (4.30) \\
& + \left[U_A k_A \, \sin\left(2(k_A z_{\min} + \phi_A)\right) + U_B k_B \, \sin\left(2(k_B z_{\min} + \phi_B)\right) \right] \hat{z}_i \\
& + \left[U_A k_A^2 \, \cos\left(2(k_A z_{\min} + \phi_A)\right) + U_B k_B^2 \, \cos\left(2(k_B z_{\min} + \phi_B)\right) \right] \hat{z}_i^2.
\end{aligned}$$

As before, this approximation applies for ultracold atoms, which are trapped deep below the upper edge of their local potential wall. Eq. 4.30 has two interesting differences relative to its single-color counterpart, Eq. 4.23, assuming $k_A \neq k_B$. First, the energy offset varies from one potential minimum location to the next. This stems from the spatial beat pattern between lasers A and B along the cavity axis, with a beat period of $(2/\lambda_B - 2/\lambda_A)^{-1} = 19.1 \, \mu$m. Second, although atoms are trapped at locations of zero net optical force, as given by Eq. 4.29, the force from each trap beam at these locations can be non-zero; atoms are attracted to spatial locations of equal and opposite forces from the two trap lights. Consequently, contrary to single-color FORTs, each trap potential in two-color FORTs can be linearly coupled to the motion of atoms. This makes atoms more susceptible to low-frequency noise on the trap lasers, as discussed in Chapter 6.

The motional oscillation frequency of each atom in an optical superlattice can be modeled from the trap's quadratic dependence on each atom's $\hat{z}_i$:

$$\frac{m}{2} \omega_{m,i}^2 \, \hat{z}_i^2 \ = \ \left[U_A k_A^2 \cos\left(2(k_A z_{\min} + \phi_A)\right) + U_B k_B^2 \cos\left(2(k_B z_{\min} + \phi_B)\right) \right] \hat{z}_i^2, \quad (4.31)$$

$$\omega_{m,i} \ = \ \sqrt{\frac{2\left[U_A k_A^2 \cos\left(2(k_A z_{\min} + \phi_A)\right) + U_B k_B^2 \cos\left(2(k_B z_{\min} + \phi_B)\right) \right]}{m}}. \quad (4.32)$$
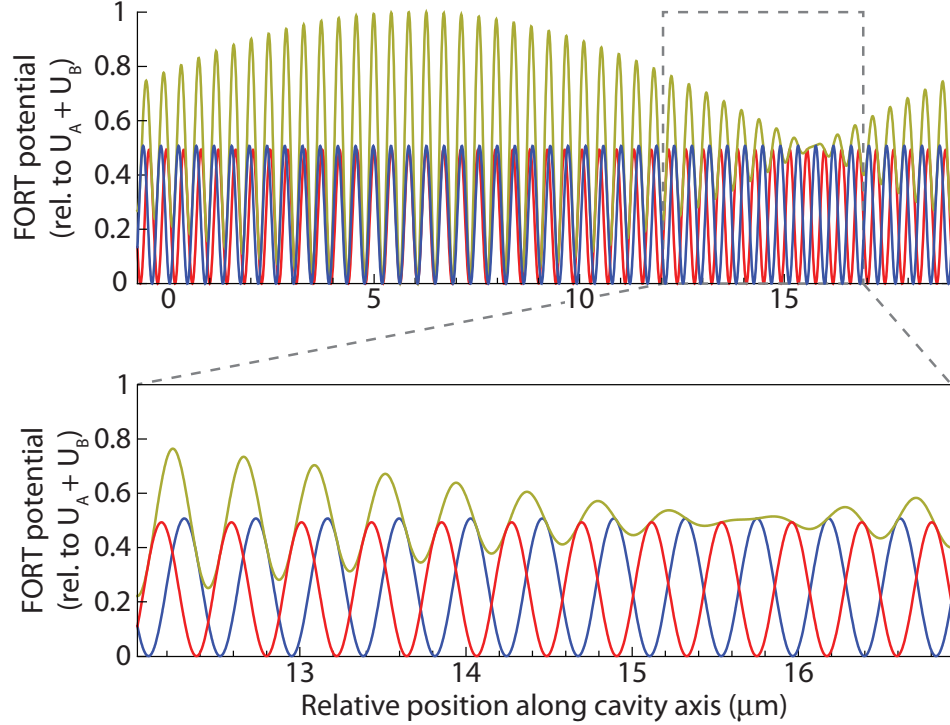
Figure 4.6: Model of the FORT used during the multi-oscillator experiments, with $\omega_{m,A,B} = 2\pi \times$ (127 kHz, 128 kHz). The figure includes the potential produced by standing waves A (blue) and B (red) individually, as well as the total, combined potential (gold). Lower panel shows a magnified view of the region bounded by the dashed gray in the upper panel.

Interestingly, the oscillation frequency can vary quite substantially from one lattice site to the next ($z_{\min,j}$ to $z_{\min,j+1}$) depending on U_A, U_B, k_A and k_B. This dispersion in ω_m allowed each lattice site to be mechanically resolved and therefore enabled the creation of an array of distinguishable atoms-based mechanical oscillators. More details on this topic will be provided in Chapter 6.

The upper and lower bounds on ω_m can be expressed as

$$\omega_{m,\max} = \sqrt{\frac{2\left|U_A k_A^2 + U_B k_B^2\right|}{m}} = \sqrt{\omega_{m,A}^2 + \omega_{m,B}^2}, \tag{4.33}$$

$$\omega_{m,\min} = \sqrt{\frac{2\left|U_A k_A^2 - U_B k_B^2\right|}{m}} = \sqrt{\omega_{m,A}^2 - \omega_{m,B}^2}, \tag{4.34}$$

$$\tag{4.35}$$

where $\omega_{m,A}$ and $\omega_{m,B}$ refer to the individual trap frequency produced by lasers A and B, respectively (Eq. 4.25). The largest variation in trap frequency, which coincides with the condition of maximum variation in trap depth over one superlattice period,

is attained when the two trap lights produce equal dipole potential ($\omega_{m,A} = \omega_{m,B}$). This was the case in the mechanical-array experiments where $\omega_{m,A,B} = 2\pi\times$ (127 kHz, 128 kHz). The resulting potential structure is shown in Fig. 4.6.

4.5   The atoms

4.5.1   Distribution, temperature and number

As described in Tom Purdy's dissertation [50], the magnetic transport to the science cavity confined atoms into very tight cigar-shaped traps, with transverse (*i.e.* along the y and z axes in Fig. 2.1) trap frequencies reaching 4.5 kHz at the science cavity. Magnetically trapped atoms could therefore be tailored to have a spatial extent along the cavity axis comparable to the FORT lattice spacing. The magnetic field minimum inside the science cavity had to be carefully and precisely overlapped with the FORT in order to optimally populate one particular optical lattice site. This was experimentally achieved by adjusting the final atom-chip-based waveguide wire currents during the atom transport to the science cavity, as described in Dan Brooks' dissertation [80]. Atoms were inserted into the cavity with the FORT as weak as possible, with just enough trap light to reliably maintain the science cavity lock. Once inside the cavity, with the magnetic trap still on, forced RF evaporation was applied to reduce the spatial extent of the atom cloud, particularly along the cavity axis, to a desired size. The evaporation also eliminated hotter atoms, but the final temperature of optically trapped atoms was found to be predominantly dependent on the characteristics of the FORT, such as the trap lasers' linewidth (*i.e.* the quality of their lock to the transfer cavity) and the level of linear coupling between the atoms and trap lights in the two-color FORT. Nonetheless, the distribution, temperature and number of optically trapped atoms remained related; no experimental knobs could control one of these parameters independently of the other two. Attainable distributions, temperatures and numbers ranged from one to eight populated lattice sites, from ~ 1 to $10\,\mu\text{K}$, and from ~ 800 to 6000 atoms, respectively.

A sporadic source of heating was uncontrolled noise impulses during experimental sequences, such as current surges on one of the conveyor wires during atom transport or mechanical "earthquakes" in the atom chip due to intense dissipated heat from the integrated electrical wires. These transient noises would show up on certain days for no apparent reasons and would rattle both the science cavity and the magnetic trap minimum. Although the sources of noise were difficult to track down, the presence of noise bursts could be clearly observed when monitoring the trap lights' intensity stabilization signal in transmission of the science cavity and the currents circulating through the atom chip wires using Hall probes. Noises would tend to appear at particular time intervals during and after atom transport. Atoms were found to be most immune to them when in the FORT. Experimental sequences were therefore

tailored to hurry atoms into the FORT and hold them in the trap, when possible, to allow the noise bursts to pass before undertaking optomechanical measurements. Post-selection was also at times used to reject experimental iterations containing too few atoms.

As previously mentioned, the distribution of atoms in the FORT was intimately related to the location of magnetic trap minimum relative to the science-cavity optical mode during handoff. Maintaining a stable atom chip temperature was observed to be critical to ensure atoms were inserted at the correct location along the cavity axis on every experimental iteration. As described in Tom's dissertation, temperature regulation was done through an actively controlled TEC, which had a maximum current input of 1.5 A. The TEC was capable of maintaining a steady temperature over an indefinite number of consecutive experimental iterations provided each iteration lasted at least 20 seconds. When shorter experimental cycles were employed, the average thermal load caused by the intense atom-chip-wire current on each cycle would exceed the TEC's capabilities, resulting in the science cavity slowly moving relative to the atom chip and hence atoms being deposited at unintended locations in the FORT.

4.5.2   Experimental checklist

As with any atomic physics experiment, properly preparing the atoms is key to getting good, reliable data. Here, the quality and size of the atoms-based oscillator produced at every experimental iteration was intimately tied with the first experimental stages, involving atom trapping and cooling prior to transport. For that reason, at the start of every day, the MOT light, routed to the experimental chamber via fiber optic cables, was re-optimized: lasers were re-locked when necessary and the beam path leading to fiber optic cables were carefully adjusted to maximize the light intensity at the experimental chamber.

Despite these day-to-day tweaks, fewer or no atoms were at times observed at the science cavity region. In virtually all cases, the root cause pertaining to a problem during the preparation stages, not with the atom transport or the hand-off to the FORT. Identifying the problem was sometimes hard. The last resort was always adjusting the mirrors directing MOT light into the experimental chamber, as the process was pain staking and difficult to undo. But, that option was sometimes used a little pre-emptively, before other possible causes were verified. It was therefore determined that having a "checklist" of things to test *before* tweaking the MOT beam alignment into the science chamber was beneficial. The list included some standard elements, applicable to many atomic physics experiments, such as the level of MOT repump power, the obstruction of free-space-circulating MOT beams, the Rb dispenser current setting. The list also included elements specific to this experimental setup, such as the range of motion of electro-mechanically controlled waveplates and the MOT to UMOT handoff. Implementing a checklist considerably helped in quickly
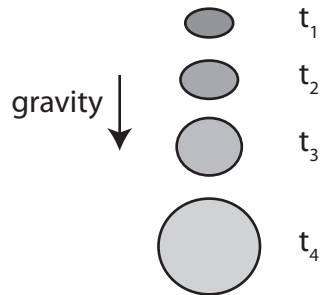
Figure 4.7: TOF imaging. The schematic shows the superposition of four fictitious images, taken at four distinct times (labeled 1 through 4), of an atom cloud falling under gravity and ballistically expanding after being released from a gaussian trap. The uneven vertical and horizontal widths at t_1 indicates the trap was initially asymmetric, while the symmetric atomic distribution at t_4 shows that atoms were initially in thermal equilibrium. The variation in the cloud's grey shade as a function of time reflects the decreasing atomic density as the cloud ballistically expands.

diagnosing atom-preparation-related problems.

4.6 Characterization tools at the science cavity

Three tools were used consistently used to properly calibrate and measure both atomic and optical properties at the science cavity. These tools and methods are discussed in this section.

4.6.1 Absorption imaging in time-of-flight

Absorption imaging in time-of-flight (TOF), that is a motion-picture-like series of snapshots of atoms expanding after being released from their optical or magnetic trap (Fig. 4.7), was a powerful tool to determine the atomic cloud's size, temperature and mean atom number. The pictures were taken horizontally, perpendicularly to both the science cavity axis and the direction of free fall. The imaging process consisted of first applying a strong steady-state magnetic field along the imaging axis to tilt the atomic spins, then releasing the atoms from their trap and, after waiting a controllable amount of time (*i.e.* the time-of-flight - TOF), resonantly imaging the atoms on their $|F = 2, m_F = 2\rangle \rightarrow |F = 3, m_F = 3\rangle$ closed cycling transition. The process would then be repeated over multiple experimental iterations, changing the TOF at every iteration.

Atoms released from their trap expanded ballistically while falling under gravity. The cloud's time-dependent size along one cartesian direction, $\sigma_{\mathrm{TOF}}(t)$, was set by the convolution of two gaussian distributions: the atomic distribution and the velocity

distribution along that same cartesian direction. The cloud's initial gaussian full-width at half-maximum (FWHM), σ_w, therefore added in quadrature with the cloud's mean gaussian expansion to yield $\sigma_\mathrm{TOF}(t)$:

$$\sigma_\mathrm{TOF}(t) = \sqrt{\sigma_\mathrm{w}^2 + |v|^2 t^2}, \tag{4.36}$$

where $|v| = \sqrt{k_B T/m}$ was the cloud's mean speed as defined by the equipartition theorem and T was the mean temperature of atoms. By fitting the series of measured gaussian cloud sizes as a function of the TOF according to Eq. 4.36, σ_w and T along the cartesian directions perpendicular to the imaging axis could be determined.

Information regarding the atom number was determined from the cloud's optical depth. The principle was simple: the more light was absorbed by the atomic cloud during imaging, the more atoms must have been present in the cloud. Details on how to extract the number of atoms from TOF images is described in Tom Purdy's dissertation [50].

4.6.2   Parametric heating

A well-known method to characterize potential traps in atomic physics is parametric heating. The technique relies on modulating the source of the trap (*e.g.* magnetic field amplitude or light intensity). When tuning the modulation to exactly twice the trap's harmonic oscillation frequency, $2 \times \omega_m$, the motion of each atom is parametrically excited until their exponentially growing motional amplitude carries them out of the trap.

This technique was applied throughout the experiments described in this dissertation to determine $\omega_{m,A}$ and $\omega_{m,B}$. The process consisted of loading atoms into a single-color FORT of interest, either A or B, applying a small modulation at frequency ω on the intensity stabilization signal of the laser light for a time t_d, and measuring both the number of remaining atoms and the cloud's final transverse size in TOF. The process would then be repeated several more times, varying ω at every iteration.

Fig. 4.8 shows a typical result obtained from such a measurement. Atoms minimally responded when the modulation was set above $2\omega_m$, leading to a narrow imaged cloud containing nearly all atoms. Atoms responded most strongly when the drive was tuned just below $2\omega_m$ due to the trap's anharmonic potential curvature. Atoms had again little response to the applied drive when driving far below $2\omega_m$. Although the number of surviving atoms and the cloud's spatial size in the direction transverse to the cavity axis pointed towards a similar ω_m, measurements of the cloud size generally gave more precise results. Results were found to be most accurate when weakly modulating the trap light, but doing so for a long time ($t_d \geq 100$ ms).
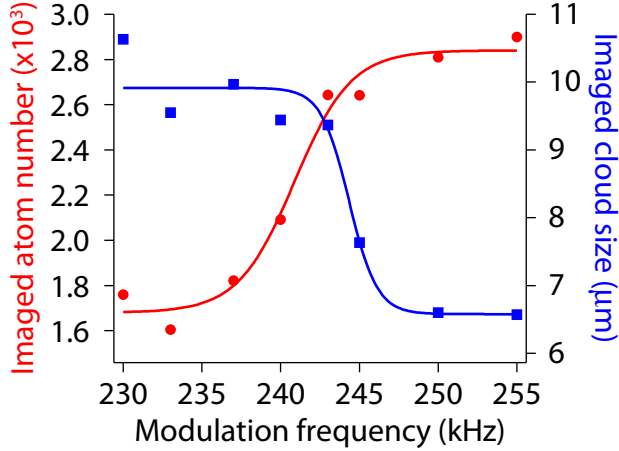
Figure 4.8: Example of measured atom number (red) and cloud size (blue) following parametric heating of optically trapped atoms. Data points shown here were done using laser A and indicate $\omega_{m,A} = 2\pi \times 121$ kHz. Lines only serve as guides for the eye.

4.6.3 Dispersive contrast measurements

As shown in Eq. 2.14, atoms positioned along the probe's standing wave collectively shift the effective resonance frequency of the science cavity. Experimentally, when loading a gaussian distribution of magnetically trapped atoms at a particular location along the cavity axis, the observed shift is dependent on both the atoms' gaussian full-width at half maximum (FWHM), σ_w, and the distribution of CQED coupling rates, $g(z)$, in the overlapping lattice sites. By mapping the cavity resonance shift, Δ_N, as a function of loading location, z_a, a measurement which has become commonly termed "contrast measurement," locations of maximum linear optomechanical, as well as parameters N and σ_w can be determined.

Consider first a single-color FORT, *e.g.* an optical trap formed only by laser A. For sufficiently weak probes, atoms are dominantly trapped by laser A at locations given in Eq. 4.22. Each lattice site has a unique probe-atom coupling rate, parametrized by $\phi_j = k_p z_j$, since the lattice site spacing, $a = \lambda_A/2 = 425$ nm, is incommensurate with the period of the probe's intensity standing wave, $\lambda_p/2 = 390$ nm (Fig. 4.9). During the magnetic-to-optical trap handoff, magnetic and optical fields are ramped faster than the site-to-site tunneling timescale, though adiabatically relative to a trap oscillation period. Each optical lattice site thus acquires a population of atoms proportional to its overlap with the magnetically trapped atomic ensemble. Under ideal experimental conditions, where the initial cloud's location z_a can be controlled with arbitrary precision, lattice site j, located at $z_{\min,j}$ (Eq. 4.22), has an atom
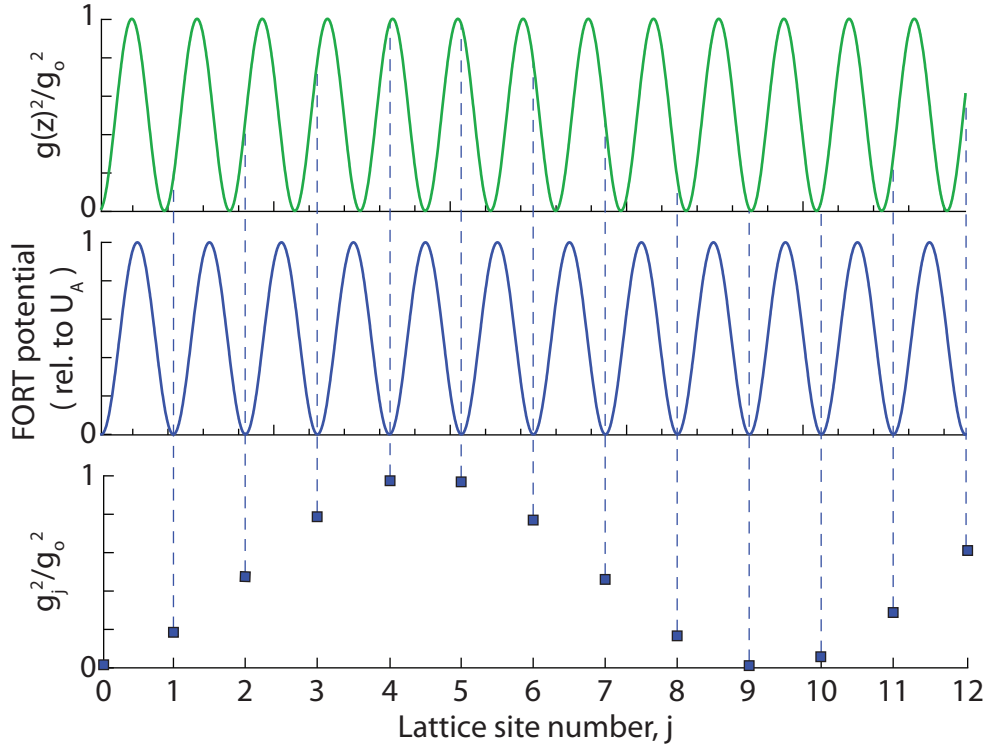
Figure 4.9: Example of the squared CQED coupling rate distribution over an entire probe - trap superperiod. The probe and trap are assumed here to have an identical phase at $j = 0$.

population of

$$N_j = \int_{z_{\mathrm{min},j}-a/2}^{z_{\mathrm{min},j}+a/2} \frac{N}{\sigma_{\mathrm{w}}\sqrt{2\pi}} e^{-\frac{1}{2}\left(\frac{z-z_a}{\sigma_{\mathrm{w}}}\right)^2} dz, \tag{4.37}$$

$$= \frac{N}{2} \left[\mathrm{erf}\left(\frac{z_{\mathrm{min},j} + a/2 - z_a}{\sqrt{2}\sigma_{\mathrm{w}}} \right) - \mathrm{erf}\left(\frac{z_{\mathrm{min},j} - a/2 - z_a}{\sqrt{2}\sigma_{\mathrm{w}}} \right) \right]. \tag{4.38}$$

The overall cavity resonance frequency shift (Eq. 2.14) as a function of loading position z_a is therefore given as

$$\Delta_N(z_a) = \sum_j \frac{N g_o^2 \sin^2(k_p z_{\mathrm{min},j})}{2\Delta_{\mathrm{ca}}} \times$$

$$\left[\mathrm{erf}\left(\frac{z_{\mathrm{min},j} + a/2 - z_a}{\sqrt{2}\sigma_{\mathrm{w}}} \right) - \mathrm{erf}\left(\frac{z_{\mathrm{min},j} - a/2 - z_a}{\sqrt{2}\sigma_{\mathrm{w}}} \right) \right], \tag{4.39}$$

where j runs over all lattice sites, contrary to Eq. 2.14 where i spanned all atoms. In the limit of an infinitely narrow initial atomic distribution ($\sigma_{\mathrm{w}} \to 0$), all atoms would
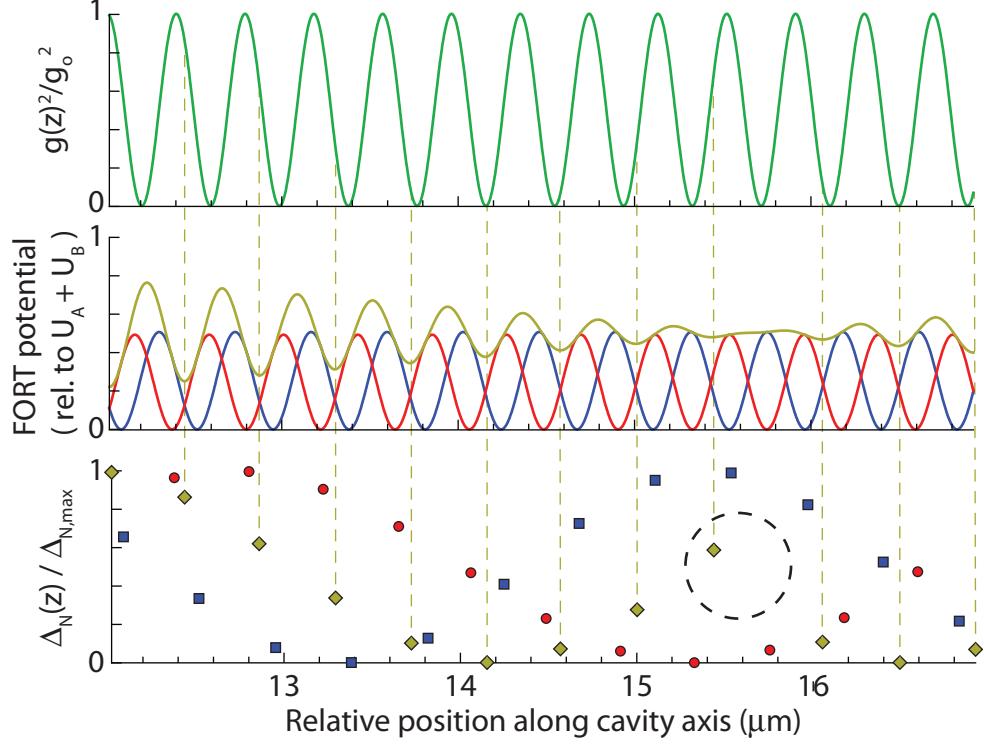
Figure 4.10: Model of the atom-induced science-cavity resonance frequency shift, Δ_N, at each lattice site based on the spatial distribution of squared CQED coupling rates and optical potentials. Three separate FORT structures are considered: laser A (blue squares, $\lambda_A = 862$ nm) and B (red dots, $\lambda_B = 843$ nm) alone, and a balanced two-color optical trap (gold diamonds, $\omega_{m,A,B} = 2\pi \times (127, 128)$ kHz). The black dashed circle in the lower panel highlights the "kink" in the two-color-FORT Δ_N distribution due to offsetting potentials from lasers A and B. The relative positions are the same as those used in the published preprint on multi-oscillator cavity optomechanics (Ref. [39]). The model applies to the experimental results shown in Fig. 4.11.

be inserted into the same lattice site $z_{\min}$, that nearest to z_a, leading to

$$\Delta_N \to \frac{Ng_o^2 \sin^2(k_p z_{\min})}{\Delta_{\mathrm{ca}}}. \tag{4.40}$$

The atom-induced cavity shift would consequently vary in a step-like fashion as a function of z_a, where steps would correspond to transitions in nearest potential minimum, from site $z_{\min,j}$ to site $z_{\min,j+1}$. When the initial cloud distribution extends over multiple sites ($\sigma_{\mathrm{w}} \gtrsim a$), the weighted sum of each site's contribution to Δ_N (Eqs. 4.37
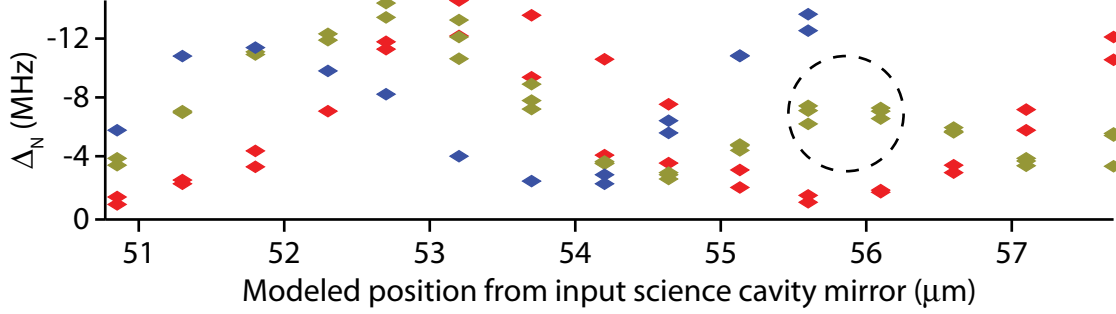
Figure 4.11: Experimentally recorded distribution of the atom-induced science-cavity resonance frequency shift as a function of the calculated loading locations relative to the input mirror. Three separate contrast measurements were taken: atoms contained in traps A (blue, $\lambda_A = 862$ nm) and B (red, $\lambda_B = 843$ nm) alone, and in a balanced FORT ($\omega_{m,A,B} = 2\pi \times (127, 128)$ kHz). Loading locations were determined based on a model of the magnetic trap produced by the atom chip and the chip's approximate distance from the input mirror. Atom-induced shifts have negative values since $\Delta_{\text{ca}} < 0$. The black dashed circle highlights the "kink" in the two-color-FORT Δ_N distribution due to offsetting potentials from lasers A and B.

and 4.39) can be approximated by an overlap integral:

$$\Delta_N(z_a) = \frac{Ng_o^2}{\Delta_{\text{ca}}} \int_{-\infty}^{\infty} \sin^2\left((k_p - k_A)z\right) \cdot \frac{1}{\sigma_{\text{w}}\sqrt{2\pi}} e^{-\frac{1}{2}\left(\frac{z-z_a}{\sigma_{\text{w}}}\right)^2} dz, \qquad (4.41)$$

$$= \frac{Ng_o^2}{2\Delta_{\text{ca}}} \left[1 - e^{-2((k_p-k_A)\sigma_{\text{w}})^2} \cdot \cos\left(2(k_p - k_A)z_a\right)\right]. \qquad (4.42)$$

Eq. 4.42 shows that the cloud's width effectively washes out the predicted steps in Δ_N, yielding instead a sinusoidal shape. To date, no experimental observation of the predicted steps in Δ_N when transitioning from one lattice site to the next has been made using the science cavity; all measurements of the distribution of Δ_N in a single-color FORT have demonstrated sinusoidal dependence on z_a.

Parameters N and σ_{w} can be readily extracted from contrasts measurements:

$$N = \Delta_{N,1/2} \times \frac{2\Delta_{\text{ca}}}{g_o^2} \qquad (4.43)$$

$$e^{-2((k_p-k_A)\sigma_{\text{w}})^2} = \frac{\Delta_{N,\text{max}} - \Delta_{N,\text{min}}}{\Delta_{N,\text{max}} + \Delta_{N,\text{min}}} \qquad (4.44)$$

where $\Delta_{N,\text{min}}$, $\Delta_{N,\text{max}}$ and $\Delta_{N,1/2}$ are the minimum, maximum, and mid-point values of Δ_N's spatial distribution. Loading locations yielding $\Delta_{N,1/2}$, $z_{a,1/2}$, are ideal for maximum linear optomechanical coupling for a particular pair of probe and trap wavelengths since $k_p z_{a,1/2} = \pi/4$.

In experiments involving both lasers A and B, contrast measurements were extensively used to characterized the relative phase between each trap light's potential structure. The distribution of Δ_N using each trap laser individually was measured first (Fig. 4.11 and lower panel of Fig. 4.10). A final contrast was then taken in a balanced superlattice ($|U_A| = |U_B|$) over one full superlattice period, where Δ_N inevitably displayed a sharp kink at the locations where traps A and B were exactly out of phase (Fig. 4.11 and lower panel of Fig. 4.10). The spatial position of the kink together with the single-color-FORT contrast measurements were used to approximately determine ϕ_A and ϕ_B (Section 4.4).

Optical frequencies and wavelengths

ω_a	:	^{87}Rb $\lvert 2,2\rangle \rightarrow \lvert 3,3\rangle$ transition frequency ...	$2\pi\times$ 384.228 THz
λ_A	:	Wavelength of laser A	850 nm (single-osc.)
		....	862 nm (multi-osc.)
λ_B	:	Wavelength of laser B	843 nm
Δ_{ca}	:	Cavity-atom detuning	$\omega_c - \omega_a$
Δ_{ta}	:	Trap light-atom detuning	$2\pi\, c/\lambda_{A,B} - \omega_a$

Science cavity properties - near-planar cavity

R	:	Radius of cavity mirrors	5 cm
L	:	Cavity length	250 μm
w_0	:	Cavity mode waist	25 μm
$\mathcal{T}_{1,2}$	:	Transmission of cavity mirrors 1 and 2	(1.5, 12) ppm
$\mathcal{L}$	:	Total optical losses in cavity mirrors	25 ppm
FSR	:	Free spectral range	$c/\left(2L\right) = 2\pi \times 600$ GHz
$\mathcal{F}$	:	Finesse at ^{87}Rb D2 transition	$2\pi/\left(\mathcal{T}_1+\mathcal{T}_2+\mathcal{L}\right) = 163,000$
κ	:	HWHM of the cavity resonance	$\mathrm{FSR}/(2\mathcal{F}) = 2\pi\times1.82$ MHz

Transfer cavity properties - confocal cavity

L	:	Cavity length	7.5 cm
FSR	:	Free spectral range	$c/\left(4L\right) = 2\pi \times 600$ GHz
$\mathcal{F}$	:	Finesse at all relevant wavelengths	500
κ	:	HWHM of the cavity resonance	$\mathrm{FSR}/(2\mathcal{F}) \sim 2\pi \times 1$ MHz

CQED and optomechanical parameters

m	:	Mass of ^{87}Rb	1.44×10^{-25} kg
Γ	:	FWHM of ^{87}Rb D2 transition	$2\pi \times 6.07$ MHz
g_o	:	Maximum atom-cavity coupling rate	$2\pi \times 13.1$ MHz
C	:	CQED cooperativity	$C = g_o^2/\kappa\Gamma = 15.7$
$\omega_{m,A}$	:	Trap frequency produced by laser A	$2\pi \times 110$ kHz (single-osc.)
		....	$2\pi \times 127$ kHz (multi-osci.)
$\omega_{m,B}$	:	Trap frequency produced by laser B	$2\pi \times 128$ kHz

Table 4.1: Experimental parameters

Chapter 5

The quantum collective motion of atoms

This chapter discusses key concepts surrounding the optical detection of ground-state collective motion of an ensemble of atoms. Its aim is to complement the results presented in Ref. [38].

When probing a cavity optomechanical system on cavity resonance ($\Delta = 0$), the mechanical object's motion couples to the light field's phase. The coupling results from inelastic scattering of probe photons. This process is known as Raman scattering. In perturbation theory, the Raman effect is understood as an absorption and subsequent emission of a photon that changes the internal state of the absorbing material. In the context of optomechanics, the mechanical object can either gain energy from the light by emitting a photon of lower frequency than the absorbed probe photon (Stokes Raman scattering), or lose energy to the light field by emitting a photon of higher frequency than the absorbed probe photon (anti-Stokes Raman scattering). This process is not strictly limited to probe photons; in principle, Raman scattered photons could themselves be inelastically scattered by the mechanical object. However, producing a cascade of Raman scattered photons require *highly* nonlinear optomechanical interactions and has therefore not yet been experimentally demonstrated[1].

Raman scattering rates can be calculated from Fermi's golden rule. For an optomechanical system in which the mechanical oscillator is in a coherent mechanical state, with a mean phonon occupation of $\bar{\nu}$, the Stokes and anti-Stokes scattering rates are $|\langle \nu + 1|\hat{z}|\nu \rangle|^2 \propto \bar{\nu} + 1$ and $|\langle \nu - 1|\hat{z}|\nu \rangle|^2 \propto \bar{\nu}$, respectively. An oscillator in its ground motional state ($\bar{\nu} = 0$) will therefore only produce Stokes photons (see Fig. 5.1). More generally, asymmetry between the number of Stokes and anti-Stokes scattered photons is indicative of the zero-point motion of the mechanical object.

---

[1]The Stamper-Kurn group's observation of ponderomotive squeezing [37] suggests that such nonlinear interactions might have been present in our system.
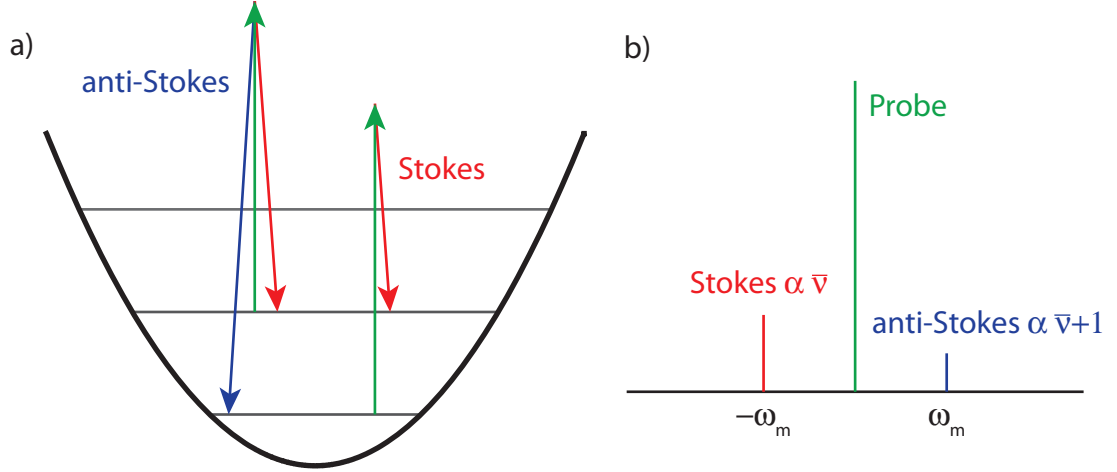
Figure 5.1: Raman scattering from the collective CM motion of atoms. (a) Schematic of the lowest three energy levels of a harmonic potential. Raman scattering from the ground state can only lead to to Stokes photons. (b) Spectrum of light following Raman scattering from the collective motion of atoms oscillating at ω_m. The asymmetry between Stokes and anti-Stokes sidebands reflects the motional mode's near-ground-state occupation. Red and blue colors emphasize that the Stokes and anti-Stokes sidebands are red-detuned and blue-detuned from the probe, respectively.

This asymmetry is most pronounced when the object is near its ground state.

This concept of asymmetric Stokes and anti-Stokes sidebands was used to show that the center-of-mass (CM) mode of motion of an ensemble of ultracold atoms, trapped in a single-color FORT, is dominantly in its ground state ($\bar{\nu} < 1$). The spectrum of Raman scattered photons was also used as a bolometer (*i.e.* heat-flow meter) to measure the level of backaction heating, that is the amount of energy deposited into the CM motional mode by the optical probe itself. Strictly speaking, the ensemble of atoms that constituted this collective CM mode was not all the optically trapped atoms, but rather a weighted sum of these atoms based on their individual linear coupling to the light field (recall Eq. 2.28). However, since atoms were distributed among only three adjacent sites, all of which had nearly maximal linear coupling to the probe field ($\phi \sim \pi/4$), the mechanical element was approximated as the entire gas' CM mode.

5.1 Raman scattering spectrum in cavity optomechanics

This section's discussion of a moving object's signature in the optical spectrum is not limited to an atoms-based realization of optomechanics; it applies generally to all

linear optomechanical systems.

The mechanical excitation spectrum of a harmonically bound object's motion linearly interacting with light inside an optical cavity is related to the spectrum of optical and mechanical inputs. The connection between the inputs and the object's phonon field follows from the transfer matrices developed as part of the linear optomechanical amplifier model (see Appendix A, Eq. A.9):

$$
\begin{pmatrix} \hat{\tilde{b}}(\omega) \\ \hat{\tilde{b}}^{\dagger}(-\omega) \end{pmatrix} = \mathbf{U} \left(\mathbf{I} - \mathbf{F}_b \mathbf{T} \mathbf{F}_a \mathbf{T} \right)^{-1} \times
$$

$$
\left[\mathbf{F}_b \mathbf{T} \mathbf{F}_a \mathbf{U}^{-1} \sqrt{2\kappa} \begin{pmatrix} \hat{\tilde{\alpha}}_{\text{in}}(\omega) \\ \hat{\tilde{\alpha}}_{\text{in}}^{\dagger}(-\omega) \end{pmatrix} + \mathbf{F}_b \mathbf{U}^{-1} \sqrt{\Gamma_m} \begin{pmatrix} \hat{\tilde{\eta}}_{\text{in}}(\omega) \\ \hat{\tilde{\eta}}_{\text{in}}^{\dagger}(-\omega) \end{pmatrix} \right], (5.1)
$$

where $\mathbf{I}$ is the identity matrix, $\mathbf{F}_a$ and $\mathbf{F}_b$ are matrices that capture the lorentzian response of the optical cavity and mechanical oscillator, respectively, $\mathbf{T}$ is the optomechanical system's transduction matrix, and $\mathbf{U}$ is a normalized rotation matrix to convert quadrature operators into corresponding creation and annihilation operators. The latter four matrices are defined in Appendix A. Since the optical field was modeled in a frame rotating at the probe carrier frequency, ω_p, frequency ω for the optical operators corresponds to the frequency detuning from ω_p; optically induced excitations of the object's motion in a linear model come from beats between the probe, at frequency ω_p, and the spectrum of optical fluctuations, at frequency $\omega_p + \omega$. The probe's delta-function tone at $\omega = 0$ was deliberately neglected since the focus of this section is to establish the mechanical object's signature in the optical spectrum, which is expected to be near $\omega = \pm\omega_m$.

In its current form, Eq. 5.1 is not particularly informative. However, the equation can be applied to a particular set of input conditions to yield the power spectral density (PSD) of the phonon field, $S_{\text{bb}}(\omega)$, which corresponds to the mechanical object's excitation spectrum. For the experiments described in this chapter, three assumptions are relevant:

- the optical probe is parked on cavity resonance ($\Delta = 0$),

- the optical input spectrum is dominated by zero-point vacuum fluctuations ($\left\langle \hat{\tilde{\alpha}}_{\text{in}}^{\dagger}(\omega)\hat{\tilde{\alpha}}_{\text{in}}(\omega) \right\rangle = 0$ and $\left\langle \hat{\tilde{\alpha}}_{\text{in}}(\omega')\hat{\tilde{\alpha}}_{\text{in}}^{\dagger}(\omega) \right\rangle = \tilde{\delta}(\omega' - \omega)$),

- the mechanical object is in physical contact and thermal equilibrium with a large reservoir at temperature T, leading to a base mean motional quantum number (*i.e.* mean phonon occupation) of $\bar{\nu}_{\text{th}} = \left[e^{\hbar\omega_m/(k_B T)} - 1 \right]^{-1}$. Mechanical inputs from the reservoir are typically described by the Caldeira-Leggett model under Markov approximation ($\left\langle \hat{\tilde{\eta}}_{\text{in}}^{\dagger}(\omega')\hat{\tilde{\eta}}_{\text{in}}(\omega) \right\rangle = \bar{\nu}_{\text{th}}\tilde{\delta}(\omega' - \omega)$ - see Appendix A).

Under these assumptions, $S_{\rm bb}(\omega)$ is found to be

$$
\begin{aligned}
S_{\rm bb}(\omega) &= \frac{\left\langle \hat{\tilde{b}}^\dagger(\omega')\hat{\tilde{b}}(\omega)\right\rangle}{2\pi\tilde{\delta}(\omega'-\omega)}, &(5.2)\\
&= \frac{1}{2\pi}\left[\frac{\Gamma_m\bar{\nu}_{\rm th} + \kappa g_c^2/\left(2(\kappa^2+\omega^2)\right)}{(\Gamma_m/2)^2 + (\omega-\omega_m)^2}\right], &(5.3)
\end{aligned}
$$

where $g_c = 2g_{\rm OM}\sqrt{\bar{n}}$ is the effective optomechanical coupling rate. The mean phonon occupation of the mechanical object's motion, $\bar{\nu}$, is obtained by integrating $S_{\rm bb}(\omega)$:

$$
\bar{\nu} = \int_{-\infty}^{\infty} S_{\rm bb}(\omega)d\omega = \bar{\nu}_{\rm th} + \frac{g_c^2}{\Gamma_m^2 + 2\Gamma_m\kappa} \sim \bar{\nu}_{\rm th} + C_{\rm OM}/2, \qquad (5.4)
$$

where the approximation $\kappa \gg \Gamma_m$ is applied. Eq. 5.4 shows that $\bar{\nu}$ is the sum of the mechanical object's initial phonon occupation, $\bar{\nu}_{\rm th}$, and the probe's quantum backaction on the object's motion, $C_{\rm OM}/2$, where $C_{\rm OM} = g_c^2/(\kappa\Gamma_m)$ is the optomechanical cooperativity. Much like the CQED cooperativity, $C_{\rm OM}$ parametrizes the rate of information exchange between the mechanical and optical degrees of freedom, g_c, relative to the mechanical and optical decay rates, Γ_m and κ, respectively. The mechanical object's motion thus transitions from being dominated by its thermal environment to its optical environment, a logical extension of Braginsky and Manukin's original finding [3]. However, here, the optical backaction does not come from a deliberately applied modulation or some spurious noise on a laser, but rather from the intracavity probe photons beating with the zero-point fluctuations at frequencies $\omega_p \pm \omega_m$. Controlling $C_{\rm OM}$ in an atoms-based optomechanical system can be achieved in two ways: by adjusting $\bar{n}$ and $\Delta_{\rm ca}$. More details on the experimental methods employed will follow in Section 5.2.

Optomechanical interactions also imprint the mechanical element's motion onto the circulating, intracavity light field (Eq. A.9, Appendix A). The optomechanically colored intracavity photon spectrum, $S_{\rm aa}(\omega)$, follows from Eq. 9 and is linearly proportional to $S_{\rm bb}$:

$$
\begin{aligned}
S_{\rm aa}(\omega) &= \frac{\left\langle \hat{\tilde{a}}^\dagger(\omega')\hat{\tilde{a}}(\omega)\right\rangle}{2\pi\tilde{\delta}(\omega'-\omega)}, &(5.5)\\
&= \frac{g_c^2}{4\left(\kappa^2+\omega^2\right)}\left[S_{\rm bb}(\omega) + \left(S_{\rm bb}(-\omega) + \frac{\left\langle\left[\hat{\tilde{b}}(-\omega'),\hat{\tilde{b}}^\dagger(-\omega)\right]\right\rangle}{2\pi\tilde{\delta}(\omega'-\omega)}\right)\right], &(5.6)
\end{aligned}
$$

where

$$
\left\langle\left[\hat{\tilde{b}}(-\omega'),\hat{\tilde{b}}^\dagger(-\omega)\right]\right\rangle = \frac{\Gamma_m\tilde{\delta}(\omega'-\omega)}{(\Gamma_m/2)^2 + (\omega+\omega_m)^2}. \qquad (5.7)
$$

The assumptions itemized above were included as part of Eqs. 5.6–5.7. Eq. 5.6 shows obvious evidence of inelastic optomechanical scattering: the terms $(S_{\rm bb}(-\omega) +$ commutation relation) and $S_{\rm bb}(\omega)$ correspond to Stokes and anti-Stokes scattered photons. Moreover, the Stokes and anti-Stokes scattering rates are asymmetric by exactly the amount expected from Fermi's golden rule: the former is proportional to $\bar{\nu} + 1$, while the latter, to $\bar{\nu}$. The intracavity photon spectrum thus forms a self-calibrated "calorimeter" of the mechanical object's mean motional energy, and hence its mean phonon occupation, based on the rate of red ($\omega = -\omega_m$) and blue ($\omega = \omega_m$) scattered photons:

$$\bar{\nu} = \frac{S_{\rm aa}(\omega_m)}{S_{\rm aa}(\omega_m) - S_{\rm aa}(-\omega_m)}. \tag{5.8}$$

An optical record of the mechanical object's energy state can be detected at the output of the cavity. For an ideal, one-sided cavity, the optical output field is given by the cavity boundary condition [45]:

$$\begin{pmatrix} \hat{\tilde{\alpha}}_{\rm out}(\omega) \\ \hat{\tilde{\alpha}}_{\rm out}^{\dagger}(-\omega) \end{pmatrix} = \sqrt{2\kappa} \begin{pmatrix} \hat{\tilde{a}}(\omega) \\ \hat{\tilde{a}}(-\omega) \end{pmatrix} - \begin{pmatrix} \hat{\tilde{\alpha}}_{\rm in}(\omega) \\ \hat{\tilde{\alpha}}_{\rm in}^{\dagger}(-\omega) \end{pmatrix} \tag{5.9}$$

$$= \sqrt{2\kappa}\mathbf{U}\mathbf{F}_a\mathbf{T}\mathbf{U}^{-1} \begin{pmatrix} \hat{\tilde{b}}(\omega) \\ \hat{\tilde{b}}^{\dagger}(-\omega) \end{pmatrix} + \left(2\kappa\mathbf{U}\mathbf{F}_a\mathbf{U}^{-1} - \mathbf{I}\right) \begin{pmatrix} \hat{\tilde{\alpha}}_{\rm in}(\omega) \\ \hat{\tilde{\alpha}}_{\rm in}^{\dagger}(-\omega) \end{pmatrix}. \tag{5.10}$$

The optical PSD at the cavity output is therefore

$$S_{\alpha\alpha}(\omega) = \frac{\left\langle \hat{\tilde{\alpha}}_{\rm out}^{\dagger}(\omega')\hat{\tilde{\alpha}}_{\rm out}(\omega) \right\rangle}{2\pi\tilde{\delta}(\omega' - \omega)} = 2\kappa S_{\rm aa}(\omega), \tag{5.11}$$

$$= \frac{1}{2\pi}\frac{C_{\rm OM}}{2}\frac{\kappa^2}{\kappa^2 + \omega^2} \times \tag{5.12}$$

$$\left[\frac{\Gamma_m^2\bar{\nu}}{(\Gamma_m/2)^2 + (\omega - \omega_m)^2} + \frac{\Gamma_m^2(\bar{\nu} + 1)}{(\Gamma_m/2)^2 + (\omega + \omega_m)^2}\right],$$

or, in cyclical units, $S_{\alpha\alpha}(f) = 2\pi S_{\alpha\alpha}(\omega)$. The more experimentally relevant form of Eq. 5.12 includes the photon energy: $S_{\zeta\zeta}(f) = \hbar\omega_p \cdot S_{\alpha\alpha}(f)$ (units of W/Hz). The cavity output spectrum holds the same direct record of the mechanical object's phonon occupation as the intracavity field (Eq. 5.8). In addition, $S_{\zeta\zeta}(f)$ can also be adapted as a bolometer for the energy exchange between the light field and the mechanical object inside the cavity. The area contained under the Stokes and anti-Stokes sidebands capture the energy deposited and removed from the mechanical element, respectively, per unit time. The difference between both areas is therefore a measure of the total power exchange:

$$P_{\rm OM} = \int_{-\infty}^{0} S_{\zeta\zeta}(f)df - \int_{0}^{\infty} S_{\zeta\zeta}(f)df, \tag{5.13}$$

$$= \frac{\Gamma_m\hbar\omega_m C_{\rm OM}}{2}\frac{\kappa^2}{\kappa^2 + \omega_m^2}, \tag{5.14}$$

where P_{OM} is the power deposited *into* the mechanical mode of motion during probing.

5.2 Calorimetry and bolometry of the quantum collective motion of atoms

During experiments, an ensemble of 4000 ultracold ^{87}Rb atoms was loaded into three adjacent lattice sites of a single-color FORT, with $\omega_m = 2\pi \times 110$ kHz, formed by laser A alone. Given their common ω_m, the dispersed atoms optomechanically responded as a single effective mechanical element, with an observed inhomogeneous mechanical full-linewidth $\Gamma_{\text{inh}} = 2\pi \times 3$ to 4 kHz. Details on the atomic ensemble's Γ_{inh} and Γ_m are presented in Section 5.4.

The center of the atomic distribution was chosen to overlap with a maximum of the probe's standing-wave intensity profile ($\phi = \pi/4$), and hence maximize the system's optomechanical coupling rate, g_{OM}. Care was taken to minimize the amount of heat delivered to the atoms during the magnetic-to-optical trap handoff. Absorption imaging of the optically trapped cloud revealed its initial temperature to be $T = 2.85\,\mu\text{K}$, yielding $\hbar\omega_m/(k_B T) = 0.54$. Atoms were then optomechanically probed. Stokes and anti-Stokes photons, scattered by collective motion of atoms, were detected in transmission of the cavity on a heterodyne detector.

The heterodyne detector's signal field operator, as defined in Section 3.2, is directly related to the probe field at the output of the cavity:

$$\hat{\tilde{\zeta}}_s(\omega) = \hat{\tilde{\zeta}}_p(\omega) = \sqrt{\hbar\omega_p}\left[\hat{\alpha}_p\sqrt{2\pi}\tilde{\delta}(\omega - \omega_p) + \hat{\tilde{\alpha}}_{\text{out}}(\omega - \omega_p)\right], \qquad (5.15)$$

where the frequency-marking sidebands are neglected. Applying this field operator to Eq. 3.28 yields a model of the experimentally detected PSD:

$$\frac{S_{\text{bal}}^{(\text{het})}(\omega + \Delta_{\text{LO},p})}{G^2 P_{\text{LO}}} = \frac{\hbar\omega_{\text{LO}}}{2\pi} + \epsilon P_p\tilde{\delta}(\omega - \Delta_{\text{LO},p}) + \epsilon\hbar\omega_p S_{\alpha\alpha}(\omega), \qquad (5.16)$$

$$= \frac{\hbar\omega_{\text{LO}}}{2\pi} + \epsilon P_p\tilde{\delta}(\omega - \Delta_{\text{LO},p}) + \frac{\epsilon\hbar\omega_p}{2\pi} \times \qquad (5.17)$$

$$\frac{C_{\text{OM,eff}}}{2}\frac{\kappa^2}{\kappa^2+\omega^2}\left[\frac{\Gamma_m^2\bar{\nu}}{\left(\frac{\Gamma_m}{2}\right)^2+(\omega-\omega_m)^2}+\frac{\Gamma_m^2(\bar{\nu}+1)}{\left(\frac{\Gamma_m}{2}\right)^2+(\omega+\omega_m)^2}\right],$$

where $\Delta_{\text{LO},p} = \omega_p - \omega_{\text{LO}} = 2\pi \times 13.6$ MHz was the LO-probe detuning during experimental measurement (different from the $2\pi \times 10$ MHz quoted in Chapter 4, which applied to the multi-oscillator experiments), $P_p = 2\kappa\hbar\omega_p\bar{n}$ the probe carrier power at the output of the cavity, and $C_{\text{OM,eff}}$ is the effective optomechanical cooperativity of the entire distribution of atoms (see Section 2.1). Eq. 5.17 was used to extract $\bar{\nu}$ from experimental measurements, and compare P_{OM} to measured integrated powers.

Tuning $C_{\text{OM,eff}} = 4\bar{n}g^2_{\text{OM,eff}}/(\Gamma_m\kappa)$ is typically done by controlling $\bar{n}$. This is particularly true in solid-state optomechanical systems, where the construction of the mechanical oscillator and cavity permanently defines the other parameters. In atomic cavity optomechanics however, $g_{\text{OM,eff}} = (N_{\text{eff}}g^2_o/\Delta_{\text{ca}})k_p Z_{\text{HO,eff}}$ can also readily be tuned by adjusting Δ_{ca}. This additional control knob is particularly sensitive since $C_{\text{OM,eff}} \propto 1/\Delta^2_{\text{ca}}$. In experiments discussed here, in order to cover a sufficiently large $C_{\text{OM,eff}}$ range, optomechanical measurements were recorded at three different Δ_{ca}: $2\pi\times$ -12, -40, and -70 GHz. At each Δ_{ca} setting, the collective atomic motion was probed with different $\bar{n}$ values, ranging from 0.4 to 2 photons.

5.3   Thermodynamics in optomechanics

In an atoms-based realization of linear cavity optomechanics with N atoms, there are N longitudinal modes of motion[2], one of which is the optically bright CM mode. The remaining $N-1$ motional modes are different collective "breathing" modes of the ensemble that have the same mechanical oscillation frequency as the CM mode, ω_m, but, to linear order, are not sensed by the optical probe[3]. All N modes are prepared at the same temperature and are physically isolated from the rest of the world since atoms are levitated inside the cavity; they only interact with each other via atom-atom collisions, which collectively define Γ_m. During optomechanical probing, optical energy is exchanged exclusively with the CM mode via backaction, while the remaining $N-1$ modes effectively form a "thermal reservoir" with which CM mode interacts.

Although unobserved by the optomechanical probe, the mean occupation of these optically dark modes can nonetheless be measured via absorption imaging. Indeed, absorption imaging at long TOF records the mean kinetic energy of an atomic ensemble (Section 4.6.1), which for a large atomic cloud $N \gg 1$ is dominated by the "breathing" modes. This ability to image the mean occupation of the CM mode's mechanical environment is unique to atomic optomechanical systems and allows the probe's backaction to be independently quantified. When probing for a time Δt, an amount $P_{\text{OM}}\Delta t$ of energy is added to the collective CM motion. After turning off the probe, the gas recovers thermal equilibrium, meaning the backaction-added energy is distributed among all $3N$ modes of motion (N modes in each cartesian direction), in a time $1/\Gamma_m$. The gas' mean temperature therefore rises by an amount

---

[2]These N modes refer to the mechanics of the system. They are not to be confused with the $N+1$ dressed-system eigenstates, involving both the photon field and the atoms' internal energy states, discussed in Section 2.1.

[3]The $N-1$ optically dark modes correspond to the higher-order expansion terms in Eqs. 2.11–2.13. Although in theory these motional modes are not sensed by the probe at locations of linear optomechanical coupling, during experiments they were very weakly sensed because atoms populated several adjacent lattice sites, none of which had *exactly* linear optomechanical coupling (*i.e.* $\phi_j \sim \pi/4$).

$\Delta T = P_{\mathrm{OM}} \Delta t / C_V$, where C_V is the heat capacity at constant volume of the trapped atomic ensemble, which can be observed in absorption imaging.

From statistical mechanics, one knows that $C_V = \partial U_{\mathrm{gas}} / \partial T$. The internal energy of an ideal gas trapped in a harmonic potential is given as $U_{\mathrm{gas}} = 3 N k_B T$ according to the equipartition theorem, which yields $C_V = 3 N k_B$. Although the FORT can be approximated as a harmonic potential, the heat capacity of a collection of *ultracold* [87]Rb atoms cannot blindly be assumed to be that of an ideal gas. A more careful derivation begins with the statistical mechanics definition of the total energy and mean quantum number of N bosons at temperature T contained in a one-dimensional harmonic trap of frequency ω_m:

$$U_{\mathrm{gas}}^{1D} = N \hbar \omega_m \bar{\nu}, \tag{5.18}$$

$$\bar{\nu} = \frac{1}{e^{\frac{\hbar \omega_m}{k_B T}} - 1}. \tag{5.19}$$

The corresponding heat capacity along that direction is therefore

$$
\begin{aligned}
C_V^{1D} &= \left(\frac{\partial U_{\mathrm{gas}}^{1D}}{\partial T} \right)_V = N k_B \left(\frac{\hbar \omega_m}{k_B T} \right)^2 \frac{e^{\frac{\hbar \omega_m}{k_B T}}}{\left(e^{\frac{\hbar \omega_m}{k_B T}} - 1 \right)^2}, \tag{5.20} \\
&= N k_B \bar{\nu}^2 \left(1 + \bar{\nu}^{-1} \right) \left[\ln \left(1 + \bar{\nu}^{-1} \right) \right]^2 \tag{5.21}
\end{aligned}
$$

As stated earlier, atoms were cooled to $T = 2.85 \,\mu\mathrm{K}$ and had a longitudinal oscillation frequency of $\omega_m = 2\pi \times 110$ kHz, leading to a classical occupation of $\hbar \omega_m / (k_B T) = 0.54$. The gas' initial mean phonon occupation and heat capacity along the cavity axis were therefore $\bar{\nu} = 0.19$ and $C_V^{1D} = 0.76 N k_B$. Along the radial directions, the FORT oscillation frequencies were smaller than the longitudinal frequency by a factor of $k_A w_0 / \sqrt{2} \sim 130$, as explained in the dissertations of Kater Murch [49] and Tom Purdy [50]. The atomic ensemble consequently behaved as an ideal gas along these radial axes, with a heat capacity of $C_V^{1D} = N k_B$. Summing the results along all three cartesian directions, one finds that the [87]Rb gas had a total heat capacity of $C_V = 2.76 N k_B$ before its motion was optically probed, but recovered the ideal gas heat capacity, $C_V = 3 N k_B$, after even short and weak probing. Since this variation in C_V from start to finish was less than 10%, the atomic ensemble's heat capacity was assumed to be that of an ideal gas for the purpose of experimental analyses.

5.4 The mechanical damping rate of collective atomic motion

In an optomechanical system, observed and predicted dynamics are intimately dependent on the mechanical element's damping. Accurately calibrating the mechanical damping is therefore important. Realizing such a calibration is easier said than

done, particularly when working with a levitated cloud of atoms. One option for calibrating Γ_m is to measure the mechanical element's impulse response function, that is to give a brief, but powerful kick and observe its ensuing oscillatory motion decay. That approach works well for systems with large mechanical Qs, where the motion remains coherent for many oscillation cycles, and where the relative level of noise is small. Unfortunately, a reliable "kick and watch" type measurement is very challenging with a cloud of ultracold atom [49]. First, the anharmonicity of the finite-depth sinusoidal potential can distort measurements of Γ_m. Any kick must therefore be kept sufficiently weak so as to dominantly generate harmonic collective motion. Second, probing with an optimal probe power in this anharmonicity-limited regime, where the coherent motional state occupation can only be slightly above unity, is difficult. The cavity probe field can easily be too strong, such that its zero-point fluctuations incoherently perturb the motion of atoms and mask the coherent motional decay, or too weak, such that an unrealistic level of statistics and filtering is necessary to reliably pick out the atoms' motion. Despite these challenges, experimental attempts at determining Γ_m in this way were made, but without success.

An alternative route is to rely on the optomechanical spring shift, Γ_{opt}, to determine Γ_m. According to linear cavity optomechanics, an optically driven mechanical element can be stimulated to the point of unstable motion. Such an unstable mechanical state has been dubbed "phonon lasing," since, much like in a laser, the mechanical element's phonon occupation rapidly amplifies at the instability threshold [81, 82]. The onset of phonon lasing occurs when $\Gamma_{\mathrm{tot}}(\omega_{\mathrm{tot}}) = \Gamma_{\mathrm{opt}}(\omega_{\mathrm{tot}}) + \Gamma_m = 0$, that is when the total mechanical damping rate of the system becomes null at the optomechanically shifted oscillation frequency[4], ω_{tot}. By measuring ω_{tot} at which the observed optomechanical response suddenly shoots up, the corresponding $\Gamma_{\mathrm{opt}}(\omega_{\mathrm{tot}})$, and hence Γ_m, can be determined using linear cavity optomechanics.

A calibration of this sort was done as part of the series of experiments detailed in this chapter. A collection of 2,600 atoms were prepared in their collective motional ground state, with $\omega_m = 2\pi \times 106$ kHz. A probe tone parked near atomic resonance ($\Delta_{\mathrm{ca}} = 2\pi \times -10.7$ GHz) was inserted a full linewidth to the blue of cavity resonance ($\Delta = 2\pi \times 3.8$ MHz $\sim 2\kappa$). The number of intracavity probe photon was varied over a series of experimental iterations. The atoms' collective optomechanical response was observed to rise nearly two orders of magnitude near $\omega_{\mathrm{tot}} = 2\pi \times 114$ kHz with, amazingly, $\bar{n} \sim 1.2$ photons (Fig. 5.2). Attributing this sharp rise to phonon lasing, one would conclude from linear cavity optomechanics that

$$\Gamma_m = -\Gamma_{\mathrm{opt}}(\omega_{\mathrm{tot}}) = \frac{-2\kappa}{\kappa^2 + \Delta^2 - \omega_{\mathrm{tot}}^2} \left(\omega_m^2 - \omega_{\mathrm{tot}}^2 \right) = 2\pi \times 360 \, \mathrm{Hz}. \qquad (5.22)$$

As a self-consistent check that linear theory can be applied at the onset of such a nonlinear phenomenon, Γ_m is separately calculated based *not* on the observed ω_{tot} at the

---

[4]ω_{tot} is represented as ω_{eff} in Appendix A. In the main body of this dissertation, symbol "eff" is reserved for the effective CM mode of atoms that couples to the light field
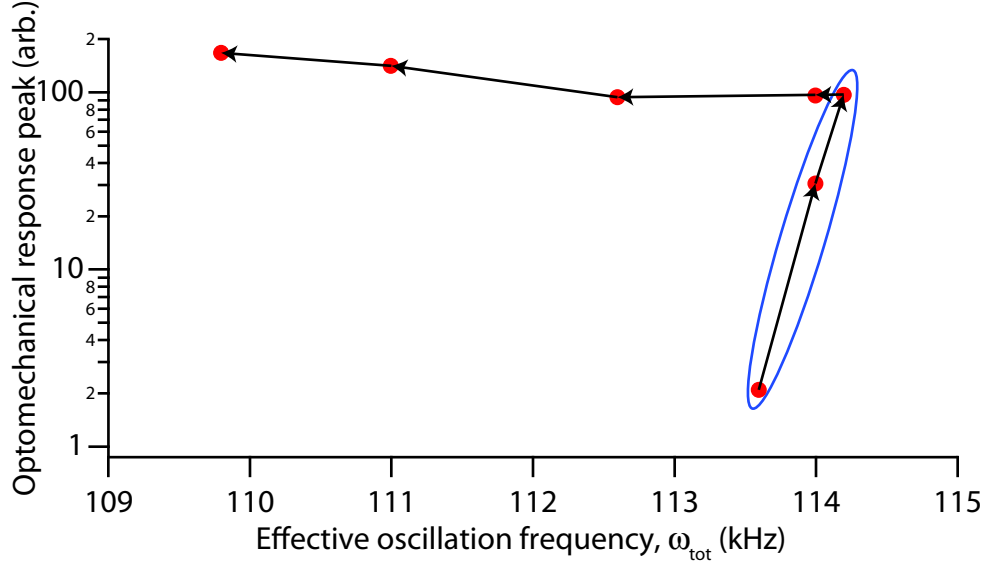
Figure 5.2: Plot of the atoms' collective optomechanical response to a quantum-limited optical drive as a function of the optomechanically shifted oscillation frequency, ω_{tot}, near the phonon lasing limit. Arrows point in the direction of increasing $\bar{n}$. The phonon lasing threshold appears as a sharp rise in the response height relative to ω_{tot} (blue ellipse). Beyond the threshold, excited atoms explore a much larger fraction of the anharmonic FORT and hence experience a lower ω_{tot}.

onset of phonon lasing, but on other, independently known experimental parameters, such as N and $\bar{n}$. Starting with Eqs. A.17–A.18 in Appendix A,

$$\Gamma_m = -\Gamma_{\text{opt}}(\omega_{\text{tot}}) = \frac{2\kappa s(\omega_{\text{tot}})}{\kappa^2 + \Delta^2 - \omega_{\text{tot}}^2}, \tag{5.23}$$

which, in the unresolved sideband limit ($\omega_{\text{tot}} \ll \kappa$) reduces to

$$\Gamma_m = \frac{8\kappa\omega_m\Delta\bar{n}g_{\text{OM,eff}}^2}{\left(\kappa^2 + \Delta^2\right)^2} \sim \frac{8\kappa\omega_m\Delta\bar{n}}{\left(\kappa^2 + \Delta^2\right)^2} \left(\frac{Ng_o^2}{\Delta_{\text{ca}}}k_p\sqrt{\frac{\hbar}{2mN\omega_m}}\right)^2 = 2\pi \times 530\,\text{Hz}. \tag{5.24}$$

Although the two results do not exactly match, they are sufficiently consistent to validate the linear theory and, on that basis, conclude that $\Gamma_m \sim 2\pi \times 450\,\text{Hz}$.

The discrepancy between Γ_m and the full mechanical linewidth detected by the on-resonance optical calorimeter and bolometer, Γ_{inh}, leads one to conclude that $\hat{Z}_{\text{CM,eff}}$, the effective CM mode of the atomic cloud that couples to the probe field, dephases into $\Gamma_{\text{inh}}/\Gamma_m \sim 7$ to 8 normal modes of motion, each of which contains $N/(\Gamma_{\text{inh}}/\Gamma_m) \sim$ 400 to 500 atoms. Causes of this dephasing include the slight dispersion in ω_m between populated lattice sites due to the probe's non-zero trap potential (i.e. contributions
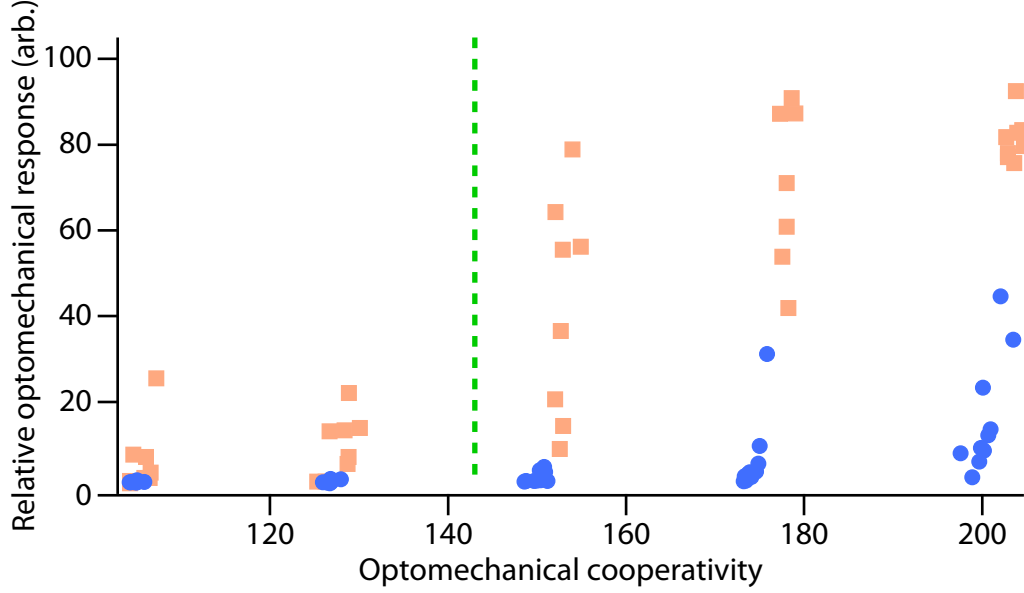
Figure 5.3: Phonon lasing threshold. Optomechanical response of two differently pre-pared atomic ensemble: one prepared in its ground state of motion (beige square), and one parametrically heated out of its motional ground state before probing (blue dots). A sharp increase in the optomechanical response, characteristic of phonon lasing, is observed at $C_{\mathrm{OM}} \sim 150$ and 200 for the ground-state and hot clouds, re-spectively. The green dashed line indicates the expected threshold C_{OM} for phonon lasing as predicted by linear cavity optomechanics theory, assuming $\Gamma_m = 2\pi \times 450$ Hz. $\Delta = 2\pi \times 3.8$ MHz, $N_{\mathrm{eff}} = N = 2600$, $g_{\mathrm{OM,eff}} = g_{\mathrm{OM}} = 2\pi \times 143$ kHz, and $\omega_m = 2\pi \times 106$ kHz

from the quadratic term in Eq.2.13 when $\phi_i \neq \pi/4$), the anharmonic nature of the FORT, both along the cavity axis and transverse directions, and collisions between atoms. Slight fluctuations in the intensity stabilization of laser A in transmission of the science cavity, and hence ω_m, also contribute to Γ_{inh}.

Another important factor in the discrepancy between Γ_m and Γ_{inh} is heating of the atomic gas, both during the preparation stages, which leads to a hotter initial cloud, and during probing. It is unclear how Γ_{inh} should change as a function of the atom cloud's temperature. On the one hand, hotter atoms occupy a larger volume and therefore have a lower collision rate, which should reduce both Γ_m and Γ_{inh}. On the other hand, hotter atoms are more susceptible to populate higher energy states, leading to a broader distribution of oscillation frequencies in an anharmonic potential and, consequently, increasing Γ_{inh}. Regardless of the end result, raising the gas' temperature should have a noticeable impact on the lasing threshold, which was empirically verified to be true: a larger C_{OM}, as calculated based on known experimental parameters and assuming $\Gamma_m = 2\pi \times 450$ Hz, was required to initiate

phonon lasing in clouds prepared with a higher temperature via parametric heating (Fig. 5.3).

The Stamper-Kurn group's understanding of damping (and dephasing) in optomechanical system remains incomplete. The answers to come will surely be tied with the concept of other collective mechanical modes acting as a reservoir, with both thermal and mechanical interactions. Answers might also be tied with more fundamental aspects of the gas, such as its spin properties (*e.g.* bosons vs. fermions) and its thermodynamic state. For instance, in the limit $\Gamma_m \to 0$, optomechanical probing one particular collective mode, even at low $\bar{n}$, should push the atomic system far out of thermal equilibrium. The gas should remain out of equilibrium for a time $1/\Gamma_m \to \infty$, enabling time-resolved experimental observations of the non-equilibrium evolution of the gas.

5.5   External means of exciting the atomic motion

In parallel to observations of probe-induced backaction, attempts were made to excite the atomic motion by a means other than the probe. The motivation was of two folds: the probe could be made to act as a "real" probe, with minimal backaction relative to the externally applied motional kick, and the drive's phase could be controlled, enabling the detection of a coherent motional response. The approach taken was to resonantly drive each atom via a large oscillating magnetic field gradient along the cavity axis, $dB(z)/dz \cdot \cos(\omega t)$, produced by the atom chip's waveguide wires. Details of the atom chip and the fields it generates are fully described in Tom Purdy's dissertation [50]. The oscillating force experienced by atom i at location z_i due to the applied magnetic field gradient was

$$F_i = m_F g_F \mu_B \left. \frac{dB(z)}{dz} \right|_{z_i} \cdot \cos(\omega_{\mathrm{dr}} t), \tag{5.25}$$

where $m_F = 2$ and $g_F = 1/2$ are the trapped atoms' magnetic sublevel and Landé g-factor, respectively, μ_B is the Bohr magneton, and $\omega_{\mathrm{dr}} = \omega_m$ is the drive frequency. All atoms, regardless of their distribution within the FORT, responded in-phase with the applied drive, meaning only the collective CM mode of motion was excited. However, the force varied from one occupied lattice site to the next since the applied magnetic field was not linearly dependent on z [50]. This limitation was no different than the probe-driven case, where each occupied lattice site had a different linear coupling to the probe, ϕ_j.

Applying a strong, oscillating magnetic field gradient through the atom chip, it turned out, not only drove the atoms, but also modulated the cavity length. This collateral shaking of the cavity modulated the phase of resonant probe light in the same way the atoms' collective motion would optomechanically respond to the probe. Moreover, the shaking cavity's phase modulation magnitude exceeded that of the

atoms, making any reliable measurement of collective atomic motion impossible. Attempts were made to compensate cavity vibrations caused by the atom-chip-based magnetic fields by applying a corrective signal to one of the cavity mirrors' PZT. This meant determining the optimal magnitude and phase of the corrective signal offline, in the absence of atoms, and feeding this information to the mirror PZT during experimental sequences; the corrective signal could not be part of a feedback loop, since atom-induced modulations would also have been canceled in this way. Unfortunately, the cavity vibrations' phase varied from one experimental iteration to the next, meaning the corrective signal sometimes reduced the vibrations, but sometimes added to them. Magnetic-field-gradient driving of the collective atomic motion as a reliable experimental method was eventually dropped.

Chapter 6

An array of quantum oscillators using ultracold atoms

This chapter discusses key concepts surrounding the creation and detection of an array of atoms-based mechanical oscillators prepared near their motional ground states. Its aim is to complement the results presented in Ref. [39].

Recalling Eqs. 2.21–2.23, linear cavity optomechanics involving atoms distributed among many lattice sites can be expressed as the sum of each site's CM mode individually coupling to the probe field. When employing a single-color FORT, such that all sites have the same ω_m, this sum of individual interactions reduces to a single effective mechanical element interacting with the light field (Eqs. 2.25–2.28). This single-effective-element-type system was the subject of study in Chapter 5. However, when employing a two-color FORT to create an optical superlattice in which each populated site has a distinguishable mechanical frequency, the mechanical system does not collapse into a single effective oscillator. Instead, each populated site's CM mode acts as an individual and distinguishable mechanical element. The distribution of ultracold atoms thus becomes an array of quantum oscillators.

Optomechanical probing of an array of mechanically distinguishable atoms-based mechanical elements was experimentally investigated. Asymmetry between Stokes and anti-Stokes sideband pairs was used to demonstrate that every element within the array was prepared near its ground state of motion. Further, as a first step towards parallel quantum-level information storage in cavity optomechanics, it was shown that energy could be communicated to one targeted oscillator, thereby changing its motional state, while preserving other oscillators in their initial quantum state.

6.1 Raman scattering from an array of mechanical elements

This section's discussion of optomechanical detection of an array of mechanical elements is not limited to an atoms-based realization of optomechanics; it applies generally to all linear optomechanical systems.

Modeling the dynamics of a single mechanical element in a cavity optomechanical system involving an array of N_{osc} mechanical objects requires expanding the transfer matrices defined as part of the optomechanical amplifier model (Appendix A, Eq. A.9):

$$\begin{pmatrix} \hat{\bar{a}}(\omega) \\ \hat{\bar{a}}^{\dagger}(-\omega) \end{pmatrix} = \mathbf{U}\mathbf{F}_a \left[\sum_{j=1}^{N_{\text{osc}}} \mathbf{T}_j \mathbf{U}^{-1} \begin{pmatrix} \hat{\bar{b}}_j(\omega) \\ \hat{\bar{b}}_j^{\dagger}(-\omega) \end{pmatrix} + \mathbf{U}^{-1}\sqrt{2\kappa} \begin{pmatrix} \hat{\bar{\alpha}}_{\text{in}}(\omega) \\ \hat{\bar{\alpha}}_{\text{in}}^{\dagger}(-\omega) \end{pmatrix} \right], \quad (6.1)$$

$$\begin{pmatrix} \hat{\bar{b}}_j(\omega) \\ \hat{\bar{b}}_j^{\dagger}(-\omega) \end{pmatrix} = \mathbf{U}\mathbf{F}_{b,j} \left[\mathbf{T}_j \mathbf{U}^{-1} \begin{pmatrix} \hat{\bar{a}}(\omega) \\ \hat{\bar{a}}^{\dagger}(-\omega) \end{pmatrix} + \mathbf{U}^{-1}\sqrt{\Gamma_{m,j}} \begin{pmatrix} \hat{\bar{\eta}}_{\text{in},j}(\omega) \\ \hat{\bar{\eta}}_{\text{in},j}^{\dagger}(-\omega) \end{pmatrix} \right], \quad (6.2)$$

where $\mathbf{F}_a$ is optical cavity's lorentzian response matrix, $\mathbf{F}_{b,j}$ and $\mathbf{T}_j$ are matrices that capture the lorentzian response and optomechanical coupling rate of the jth mechanical element, respectively, and $\mathbf{U}$ is a normalized rotation matrix to convert quadrature operators into corresponding creation and annihilation operators (see Appendix A). Eqs. 6.1–6.2 show that the mechanical elements communicate with each other only via the light field; the light, in effect, places a spring between each mechanical oscillator. These light-induced springs couple the oscillators together, thereby changing the normal modes of the system and, in a larger picture, determining which mode(s) the light senses.

The intracavity photon field's contribution to each mechanical element's phonon field spectrum can be adiabatically removed by combining Eqs. 6.1–6.2:

$$\begin{pmatrix} \hat{\bar{b}}_r(\omega) \\ \hat{\bar{b}}_r^{\dagger}(-\omega) \end{pmatrix} = \mathbf{U}\left(\mathbf{I} - \mathbf{F}_{b,r}\mathbf{T}_r\mathbf{F}_a\mathbf{T}_r\right)^{-1}\mathbf{F}_{b,r} \times \qquad (6.3)$$

$$\left[\mathbf{T}_r\mathbf{F}_a \sum_{\substack{j=1 \\ j \neq r}}^{N_{\text{osc}}} \mathbf{T}_j \mathbf{U}^{-1} \begin{pmatrix} \hat{\bar{b}}_j(\omega) \\ \hat{\bar{b}}_j^{\dagger}(-\omega) \end{pmatrix} \right.$$

$$\left. + \mathbf{T}_r\mathbf{F}_a\mathbf{U}^{-1}\sqrt{2\kappa} \begin{pmatrix} \hat{\bar{\alpha}}_{\text{in}}(\omega) \\ \hat{\bar{\alpha}}_{\text{in}}^{\dagger}(-\omega) \end{pmatrix} + \mathbf{U}^{-1}\sqrt{\Gamma_{m,j}} \begin{pmatrix} \hat{\bar{\eta}}_{\text{in},j}(\omega) \\ \hat{\bar{\eta}}_{\text{in},j}^{\dagger}(-\omega) \end{pmatrix} \right],$$

where $\mathbf{I}$ is the identity matrix. The second line of Eq. 6.3 reflects the effective springs that binds the rth mechanical element and all other elements arrayed within the

optical resonator. Obviously, each phonon field spectrum in its general form is quite complex. However, when restricting the probe to be on cavity resonance ($\Delta = 0$), $\mathbf{F}_a$ becomes a diagonal matrix, which yields $\mathbf{T}_r \mathbf{F}_a \mathbf{T}_j = 0$ for all (r, j) combinations. This means the light-induced springs have a spring constant of 0 when the probe is parked on cavity resonance. Each mechanical element's phonon field in this specialized case is therefore independent of other phonon fields arrayed within the optical resonator:

$$
\begin{pmatrix} \hat{\tilde{b}}_r(\omega) \\ \hat{\tilde{b}}_r^\dagger(-\omega) \end{pmatrix} = \mathbf{U}\mathbf{F}_{b,r} \left[\mathbf{T}_r \mathbf{F}_a \mathbf{U}^{-1} \sqrt{2\kappa} \begin{pmatrix} \hat{\tilde{\alpha}}_{\text{in}}(\omega) \\ \hat{\tilde{\alpha}}_{\text{in}}^\dagger(-\omega) \end{pmatrix} + \mathbf{U}^{-1} \sqrt{\Gamma_{m,j}} \begin{pmatrix} \hat{\tilde{\eta}}_{\text{in},j}(\omega) \\ \hat{\tilde{\eta}}_{\text{in},j}^\dagger(-\omega) \end{pmatrix} \right]. \quad (6.4)
$$

This condition of on-resonance probing was applied during experiments treated in this chapter. Moreover, the same assumptions regarding the optical and mechanical inputs as those postulated for the single-oscillator experiments (Chapter 5) are relevant here:

- the optical input spectrum is dominated by zero-point vacuum fluctuations ($\left\langle \hat{\tilde{\alpha}}_{\text{in}}^\dagger(\omega) \hat{\tilde{\alpha}}_{\text{in}}(\omega) \right\rangle = 0$ and $\left\langle \hat{\tilde{\alpha}}_{\text{in}}(\omega') \hat{\tilde{\alpha}}_{\text{in}}^\dagger(\omega) \right\rangle = \tilde{\delta}(\omega' - \omega)$),

- the mechanical input spectrum follows the Caldeira-Leggett model under Markov approximation: $\left\langle \hat{\tilde{\eta}}_{\text{in}}^\dagger(\omega') \hat{\tilde{\eta}}_{\text{in}}(\omega) \right\rangle = \bar{\nu}_{\text{th}} \tilde{\delta}(\omega' - \omega)$, where $\bar{\nu}_{\text{th}}$ is the mean phonon occupation due to the gas' finite temperature.

Following the same approach as that outlined in Section 5.1, the outgoing cavity field's PSD, composed of all Raman-scattered photons inside the cavity, is found to carry a proportional copy of each mechanical element's motional PSD:

$$
S_{\alpha\alpha}(\omega) = \frac{\left\langle \hat{\tilde{\alpha}}_{\text{out}}^\dagger(\omega') \hat{\tilde{\alpha}}_{\text{out}}(\omega) \right\rangle}{2\pi \tilde{\delta}(\omega' - \omega)} = 2\kappa S_{\text{aa}}(\omega), \quad (6.5)
$$

$$
= \frac{1}{2\pi} \frac{\kappa^2}{\kappa^2 + \omega^2} \times \quad (6.6)
$$

$$
\sum_{j=1}^{N_{\text{osc}}} \frac{C_{\text{OM},j}}{2} \left[\frac{\Gamma_{m,j}^2 \bar{\nu}_j}{(\Gamma_{m,j}/2)^2 + (\omega - \omega_{m,j})^2} + \frac{\Gamma_{m,j}^2 (\bar{\nu}_j + 1)}{(\Gamma_{m,j}/2)^2 + (\omega + \omega_{m,j})^2} \right],
$$

where $C_{\text{OM},j}$, $\bar{\nu}_j$, $\Gamma_{m,j}$ and $\omega_{m,j}$ are the optomechanical cooperativity, mean phonon occupation, mechanical damping rate and mechanical resonance frequency of the jth mechanical element. The analog to $S_{\alpha\alpha}(\omega)$ in units of W/Hz is given by $S_{\zeta\zeta}(f) = 2\pi \cdot \hbar\omega_p \cdot S_{\alpha\alpha}(\omega)$. Each element's contribution to $S_{\alpha\alpha}(\omega)$ is peaked near its mechanical resonance frequency. If every element r arrayed within the cavity has a unique mechanical frequency, such that $|\omega_{m,j} - \omega_{m,r}| > (\Gamma_{m,j} + \Gamma_{m,r})/2$ for every $j \neq r$, then each element's motional spectrum can be distinguished from that of others. This condition of distinguishability was applied during experiments. The number of populated optomechanically bright lattice sites was determined based on the heterodyne-detected distribution of Raman peaks. And each site's $\bar{\nu}_j$ was individually and simultaneously measured by comparing its distinguishable Stokes and anti-Stokes sideband pair.

6.2 Creation, detection and control of an array of quantum collective atomic oscillators

Experimental realizations of an array of atoms-based mechanical oscillators relied on populating several potential minima of an optical superlattice formed by lasers A ($\lambda_A = 862$ nm) and B ($\lambda_B = 843$ nm), with lattice spacing $a \sim 420$ nm. An ensemble of ultracold atoms was loaded into the superlattice, populating between 1 and 8 sites depending on the ensemble's size, which was controlled by tuning the end point of the force radio-frequency (RF) evaporation applied at the science cavity (see Section 4.5.1). The temperature of the resulting, optically trapped gas was measured through absorption imaging to be $< 7\,\mu$K for all evaporation settings. As detailed in Section 4.4.2, the intracavity intensities of lasers A and B were stabilized to nearly identical values in order to maximize the variation in ω_m from one site to the next; the stabilized optical potentials had oscillation frequencies of $\omega_{m,A,B} = 2\pi \times (127$ kHz, 128 kHz). These settings satisfied the distinguishability criteria stated in the previous section, meaning that the collective CM motion of atoms in each populated superlattice site formed a distinguishable mechanical element that could be optomechanically probed.

In order to create an array of maximally distinguishable collective atomic oscillators, the spatial structure of the superlattice needed to be mapped first. This was achieved experimentally using a method that was termed "mechanical resonance imaging." The method, explained in detail as part of the published experimental results (see Ref. [39]), consisted of sequentially measuring the distribution of mechanical resonance frequencies over one full superlattice period; only one site was populated and probed on each experimental iteration. The method relied heavily on the ability to populate a single lattice site, which meant having a tight magnetic trap prior to loading atoms into the FORT and controlling the minimum location of that magnetic trap with nanometer-scale precision. Both requirements were experimentally achieved thanks to the atom chip and an extensive model of the magnetic fields produced by its embedded wires (see Dan Brook's dissertation [80]).

Having characterized the superlattice and its distribution of mechanical resonances, an array of collective atomic oscillators was prepared. A cloud of atoms with gaussian FWHM $\sigma_{\rm w} \sim 3.1\,\mu$m, centered at a location of large mechanical-frequency dispersion and maximal linear optomechanical coupling to the probe, was loaded into the two-color FORT. The created array was then exposed to a weak probe light ($\Delta_{\rm ca} = -2\pi \times 40$ GHz and $\bar{n} \sim 1$), with each site having $C_{\rm OM} \leq 0.6$, and the spectrum of Raman-scattered photons were detected in transmission of the science cavity. The asymmetry between corresponding Stokes and anti-Stokes sidebands demonstrated that each site's collective CM mode had a mean phonon occupation $\bar{\nu}$ near unity, indicating that every distinguishable mechanical element in the array was near its motional quantum ground state. As many as six atoms-based oscillators were simultaneously probed to be near their mechanical ground states, a remarkable

achievement given that no other optomechanical architecture at the time contained more than two mechanical elements and none of the two-oscillator optomechanical systems [33, 83, 84, 85] could demonstrate that both oscillators simultaneously satisfied $\bar{\nu} \sim 1$. This system's ability to simultaneously probe the mechanical spectrum of all the occupied sites stemmed from operating in the unresolved sideband regime $(\omega_m \ll \kappa)$. Eq. 6.6 shows that if the system had operated in the resolved sideband regime $(\omega_m \gg \kappa)$, as is the case for most other optomechanical architectures, the probe's sensitivity to the spectrum of Raman sidebands when parked on cavity resonance would have been proportional to $\kappa^2/\omega_m^2 \ll 1$.

6.3   Exciting collective motion by force

With an array of distinguishable atoms-based mechanical elements near their ground states of motion experimentally in hand, one attractive path forward aims at exciting the collective motion of atoms at certain, targeted sites by harnessing their spatial and mechanical isolation. This selective "addressing" of mechanical elements requires the ability to apply controllable position- and/or frequency-dependent forces, which, in a system with as many as three colors of light illuminating atoms, can be realized through optical forces.

As stated in Section 4.4.2, lattice sites in an optical superlattice are localized at the intersection of equal-magnitude and oppositely oriented forces from the two trap lasers. When probe light is added to the system, the potential minima are shifted to locations of zero net force from all three light source. This probe-induced shift is responsible for optical nonlinearity and bistability when large probe powers are applied [28, 54]. For experimental conditions considered here, however, the probe negligibly displaces the potential minima. The confining force applied by each laser at the many lattice sites, $z_{\mathrm{min},j}$ (Eq. 4.29), is equal to their respective local potential gradient:

$$\bar{F}_A(z_{\mathrm{min},j}) = U_A k_A \sin\left(2(k_A z_{\mathrm{min},j} + \phi_A)\right), \tag{6.7}$$

$$\bar{F}_B(z_{\mathrm{min},j}) = U_B k_B \sin\left(2(k_B z_{\mathrm{min},j} + \phi_B)\right), \tag{6.8}$$

$$\bar{F}_p(z_{\mathrm{min},j}) = U_p k_p \sin\left(2k_p z_{\mathrm{min},j}\right). \tag{6.9}$$

These static optical forces are fixed for a particular array of atomic oscillators, with desired spatial and mechanical frequency distribution, and a particular optomechanical probe strength. Instead, controllable forces can be generated by modulating the trap intensities about their stabilized, mean values.

For a modulation of the form $A_r \sin(\omega_{\mathrm{mod,r}} t + \theta_r)$ on laser r, where $r = A, B$ or p, atoms trapped at site $z_{\mathrm{min},j}$ experience an oscillating force given by

$$F_r(t, z_{\mathrm{min},j}) = \bar{F}_r(z_{\mathrm{min},j}) \times A_r \sin(\omega_{\mathrm{mod,r}} t + \theta_r), \tag{6.10}$$

$$\tilde{F}_r(\omega, z_{\mathrm{min},j}) = i\sqrt{2\pi} \frac{\bar{F}_r(z_{\mathrm{min},j}) A_r}{2} \left[e^{-i\theta_r} \tilde{\delta}(\omega - \omega_{\mathrm{mod}}) - e^{i\theta_r} \tilde{\delta}(\omega + \omega_{\mathrm{mod}}) \right], \tag{6.11}$$

where $F_r(t, z_{\min,j})$ and $\tilde{F}_r(\omega, z_{\min,j})$ are the time- and frequency-domain forms of the applied force, respectively. Atoms at each populated lattice site collectively and coherently respond to this force by a time-dependent change in their center-of-mass momentum. Modeling this response draws upon the optomechanical amplifier model introduced in Chapter 2.

As stated in Sec. 2.3, applied forces are related to $\hat{\xi}_-$, and their bosonic analog $\hat{\eta}_-$. The frequency-domain position, $\hat{\tilde{Z}}_{\mathrm{CM},j}^{(F)}(\omega)$, and momentum, $\hat{\tilde{P}}_{\mathrm{CM},j}^{(F)}(\omega)$, coherent response of atomic oscillator j to $\tilde{F}_r(\omega, z_{\min,j})$ can be extrapolated from Eqs. 9 and 35 in Appendix A:

$$\left\langle \hat{\tilde{Z}}_{\mathrm{CM},j}^{(F)}(\omega) \right\rangle = \frac{-\omega_{m,j}}{\left(\frac{\Gamma_{m,j}}{2} - i\omega\right)^2 + \omega_{m,j}^2} \frac{\tilde{F}_r(\omega, z_{\min,j})}{N_j m \omega_{m,j}}, \tag{6.12}$$

$$\left\langle \hat{\tilde{P}}_{\mathrm{CM},j}^{(F)}(\omega) \right\rangle = \frac{\frac{-\Gamma_{m,j}}{2} - i\omega}{\left(\frac{\Gamma_{m,j}}{2} - i\omega\right)^2 + \omega_{m,j}^2} \tilde{F}_r(\omega, z_{\min,j}). \tag{6.13}$$

Unsurprisingly, $\left\langle \hat{\tilde{Z}}_{\mathrm{CM},j}^{(F)}(\omega) \right\rangle$ and $\left\langle \hat{\tilde{P}}_{\mathrm{CM},j}^{(F)}(\omega) \right\rangle$ are largest when $\omega_{\mathrm{mod}} = \omega_{m,j}$. In other words, atoms are most susceptible to the applied force modulation when driven on resonance. In the context of a superlattice with mechanically distinguishable elements (recall $|\omega_{m,j} - \omega_{m,r}| > (\Gamma_{m,j} + \Gamma_{m,r})/2$), a targeted lattice site, labeled "tgt," can be selectively "addressed" by tuning ω_{mod} to be resonant with $\omega_{m,\mathrm{tgt}}$ while, in principle, leaving neighboring sites unperturbed.

When simultaneously pinging the atoms with an external force modulation and optomechanically probing each site's collective response, a delta-function like modulation is imprinted on the light field. For the experimentally relevant case of $\Delta = 0$, only the phase-quadrature of the intracavity light field is modulated by the coherent response of atomic oscillators:

$$\hat{\tilde{a}}_-^{(F)}(\omega) = \frac{\sqrt{\kappa}}{\kappa - i\omega} \sum_{j=1}^{N_{\mathrm{osc}}} \sqrt{\frac{C_{\mathrm{OM},j}\Gamma_{m,j}}{2}} \frac{\left\langle \hat{\tilde{Z}}_{\mathrm{CM},j}^{(F)}(\omega) \right\rangle}{Z_{\mathrm{HO,j}}}. \tag{6.14}$$

The force-induced Raman scattering can also be observed in the intracavity light's phase-quadrature PSD. Accounting for the both coherent atomic response to the applied force ("F") and the incoherent collective motion of atoms at each site ("inh"), with an incoherent phonon occupation of $\bar{\nu}_j$, the total intracavity PSD ("tot") is given

by

$$S_{a_-a_-}^{(\text{tot})}(\omega) \;=\; \frac{\left\langle \hat{\tilde{a}}_-^{(\text{tot})\dagger}(\omega')\hat{\tilde{a}}_-^{(\text{tot})}(\omega)\right\rangle}{2\pi\tilde{\delta}(\omega'-\omega)} = S_{a_-a_-}^{(\text{inh})}(\omega) + S_{a_-a_-}^{(F)}(\omega), \tag{6.15}$$

$$S_{a_-a_-}^{(\text{inh})}(\omega) \;=\; \frac{\left\langle \hat{\tilde{a}}_-^{(\text{inh})\dagger}(\omega')\hat{\tilde{a}}_-^{(\text{inh})}(\omega)\right\rangle}{2\pi\tilde{\delta}(\omega'-\omega)}, \tag{6.16}$$

$$\;=\; \frac{1}{2\pi}\frac{\kappa}{\kappa^2+\omega^2}\sum_{j=1}^{N_{\text{osc}}}\frac{C_{\text{OM},j}}{4}\frac{\Gamma_{m,j}^2(2\bar{\nu}_j+1)}{(\Gamma_{m,j}/2)^2+(\omega-\omega_{m,j})^2}, \tag{6.17}$$

$$S_{a_-a_-}^{(F)}(\omega) \;=\; \frac{\left\langle \hat{\tilde{a}}_-^{(F)\dagger}(\omega')\hat{\tilde{a}}_-^{(F)}(\omega)\right\rangle}{2\pi\tilde{\delta}(\omega'-\omega)}, \tag{6.18}$$

$$\;=\; \frac{1}{2\pi}\frac{\kappa}{\kappa^2+\omega^2}\sum_{j=1}^{N_{\text{osc}}}\frac{C_{\text{OM},j}\Gamma_{m,j}}{2}\frac{\left\langle \hat{\tilde{Z}}_{\text{CM},j}^{(F)}(\omega')\right\rangle^{\dagger}\left\langle \hat{\tilde{Z}}_{\text{CM},j}^{(F)}(\omega)\right\rangle}{Z_{\text{HO},j}^2\tilde{\delta}(\omega'-\omega)}. \tag{6.19}$$

When experimentally detecting $S_{a_-a_-}^{(F)}(\omega)$, the remaining delta function in Eq. 6.19, $1/\tilde{\delta}(\omega'-\omega)$, is replaced by ω_{BW}, the measurement frequency bandwidth.

The total phase-quadrature PSD is, of course, also present at the output of the cavity and can be detected downstream on the heterodyne detector. The heterodyne photocurrent's phase-quadrature PSD, $S_{\text{dem}}^{(\text{het})}(\omega)$ is related to $S_{a_-a_-}^{(\text{tot})}(\omega)$:

$$\frac{S_{\text{dem}}^{(\text{het})}(\omega)}{G^2 P_{\text{LO}}} \;=\; \frac{1}{2}\frac{\hbar\omega_{\text{LO}}}{2\pi} + \epsilon\hbar\omega_p \cdot 2\kappa S_{a_-a_-}^{(\text{tot})}(\omega) \tag{6.20}$$

Looking specifically at the phase-quadrature PSD has the important advantage that the relative signal-to-noise ratio (SNR) of both the force-induced and incoherent-atomic-motion-produced modulations are maximal since only half of the total detected shot-noise appears in each quadrature (see Section 3.2).

This method of producing an isolated mechanical response within an array of atomic oscillators by controllably modulating one or more of the light beams, and optomechanically detecting the response of each oscillator either during or after the applied force, was applied in a variety of ways. Most of these experimental undertakings were never reported in the literature, since they failed to meet their respective intended objective. These unsuccessful investigations, described one-by-one in the following subsections, did provide helpful lessons which eventually led to the experimental demonstration that the collective motional state at one targeted lattice site could be excited by several quanta while maintaining neighboring mechanical elements near their ground states of motion (see Ref. [39]).
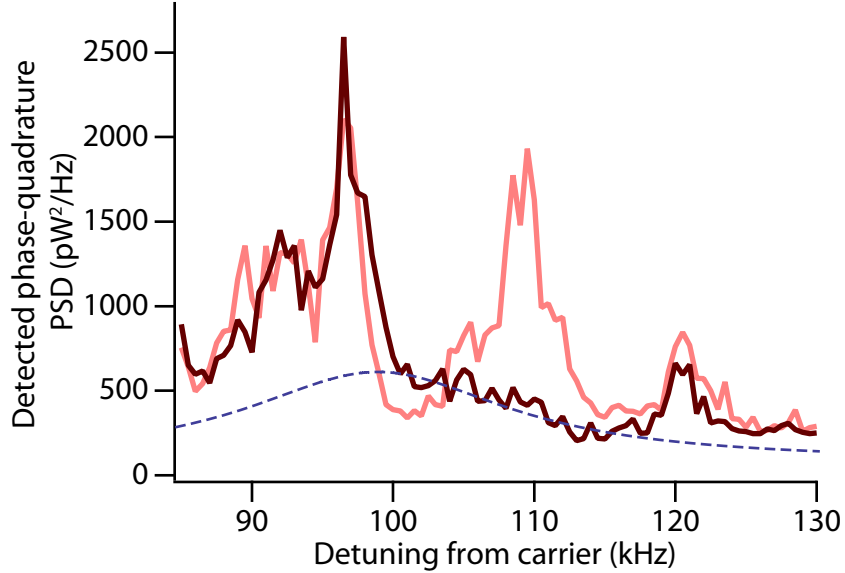
Figure 6.1: Attempted elimination of a collective atomic oscillator. Figure shows the measured optomechanical response from three initially distinguishable collective atomic oscillators ($\omega_{m,(1,2,3)} = 2\pi \times (97, 110, 121)$ kHz) with (maroon) and without (light red) an applied modulation on laser B at $\omega_{\mathrm{mod}} = 2\pi \times 102$ kHz prior to probing. The initially peaked response at $\omega_{m,2} = 2\pi \times 110$ kHz becomes shifted to lower frequencies and broaden (dashed blue curve - a guide for the eye only), as atoms are heated up the anharmonic ladder of motional modes by the force modulation. Site $\omega_{m,3}$ is also unintentionally affected by the applied modulation.

6.3.1 Selective elimination of atomic oscillators

A first experimental objective following the creation of a superlattice-based array of collective atomic oscillators was the selective removal of one oscillator without altering the motional states of its neighbors. The motivation was to show that the array structure, that is the distribution of mechanical elements in space, could be controllably tailored. The proposed method consisted of resonantly exciting the collective CM motion of atoms at a targeted lattice site by modulating one of the trap potentials until atoms escaped from the optical potential. The remaining distribution of atoms-based mechanical elements would then be optomechanically probed to show that all neighboring elements were still near their motional ground states while no photons were Raman scattered at the mechanical oscillation frequency of the eliminated site. To confirm atoms were truly ejected from the superlattice, the number of surviving atoms would be counted through absorption imaging.

Experimental attempts at single-site elimination began by populating three adjacent and distinguishable sites ($\omega_{m,(1,2,3)} = 2\pi \times (97, 110, 121)$ kHz) with most atoms residing in the lower two sites. Intensity modulations were applied to laser B for a du-

ration of ~ 100 ms at $\omega_{\mathrm{mod}} = 2\pi \times 102$ kHz in an attempt to forcefully eliminate atoms from the middle site, with mechanical oscillation frequency $\omega_{m,\mathrm{tgt}} = \omega_{m,2} = 2\pi \times 110$ kHz. The modulation frequency was deliberately red-detuned from mechanical resonance in order to compensate for the trap's anharmonic frequency distribution, that is the reduction in oscillation frequency as atoms climb to higher motional energy bands. A suppression of Raman-scattered photons at $\omega_{m,\mathrm{tgt}}$ was convincingly observed by the optical probe, though with some impact to the motional state of atoms in the highest-frequency site (Fig. 6.1). However, the ejection of atoms was not corroborated by absorption images, which showed no noticeable change in atom number. The combination of results instead indicated that the energy received by the targeted CM mode was insufficient to eject atoms, but did excite atoms to many of the higher motional bands and consequently reduced the CM mode's coupling to the probe field.

Measurements with a frequency-chirped force modulation were also taken in an attempt to follow atoms up their ladder of motional states. The chirp started at $\omega_{m,\mathrm{tgt}}$ and ended at $\omega_{\mathrm{mod}} = 2\pi \times 102$ kHz, just before the mechanical resonance frequency of the neighboring site. Unfortunately, no appreciable loss of atoms was observed and the collective motional states in neighboring sites were perturbed. The idea of single-site elimination was consequently dismissed as a worthwhile experimental pursuit.

6.3.2 Single-site force modulation cancellation

The second experimental objective aimed to simultaneously modulate two optical beams in such as way as to avoid exciting the collective CM motion of atoms at one targeted location, a rather backwards application of force driving. By carefully adjusting the relative phases and amplitudes of each laser's modulation (see Eq. 6.10), the net drive at one site could be exactly canceled, while being nonzero at adjacent sites. In principle, the pair of forces could have originated from any two of the three lasers present in the system. However, the site-to-site variation in force cancellation was most pronounced when employing the probe as one of the two drive sources, since its wavelength was the most incommensurate.

Atoms were dominantly loaded into two neighboring and distinguishable sites of the superlattice. Optomechanical probing of their motion then followed, during which modulations on the probe and on laser B were applied. The motional spectra of both sites were simultaneously recorded at the output of the science cavity. The magnitude and phase of the observed responses served as a guide to optimize the force cancellation at one of the sites. Since the probe light both drove and recorded the collective CM motion of atoms, its settings were kept fixed; laser B's amplitude and phase was instead iteratively adjusted. The optimization procedure was cumbersome and lengthy as it involved navigating in a two-dimensional space. As many as one hundred consecutive measurements were taken to optimize one parameter, say the amplitude, as function of the other, in this case the phase (Fig. 6.2). This local
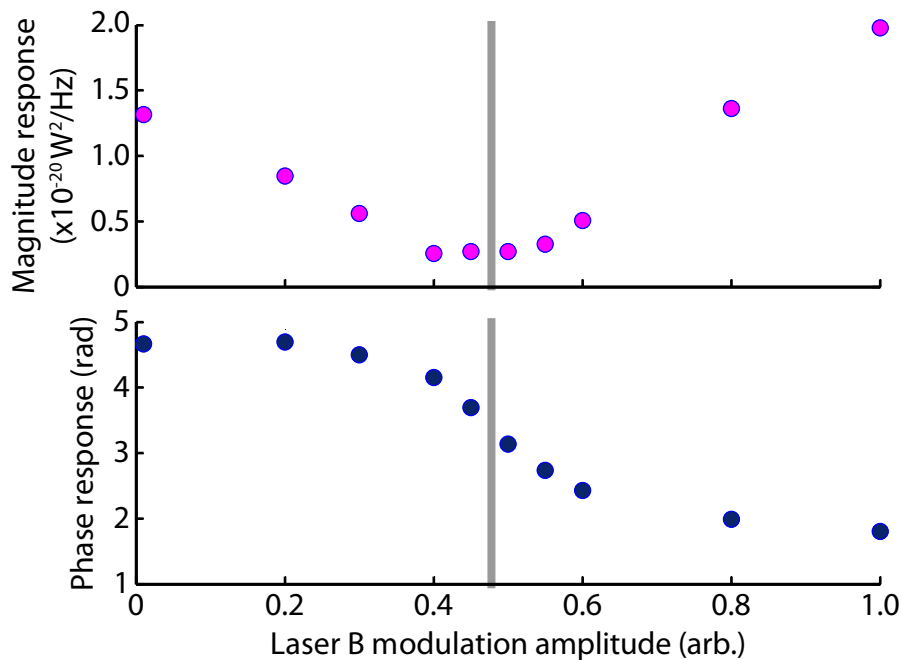
Figure 6.2: Calibration of laser B's modulation amplitude for force cancellation at a targeted lattice site. Figures show the coherent optomechanical response from atoms at that targeted site for various laser B amplitudes. Gray lines highlight optimal amplitude for one particular modulation phase.

optimum would then be applied on the next hundred measurements to locally optimize the phase (Fig. 6.3), and so forth. Optimizing the settings for force cancellation at both sites typically took the better fraction of a day.

Experimental observations following the careful optimization of laser B's modulation sadly did not demonstrate adequate force cancellation at either sites; the collective phonon state at both locations were steadily high under both drive settings (Fig. 6.4). Part of the blame was attributed to the lack of stability in the system. Optimal settings were found to vary slightly from one calibration to the next, enough to impart substantial momentum kicks on the targeted site. Part of the blame was also assigned to the insufficient level of site-to-site variation in each light's linear coupling to the collective atomic motion. In other words, the probe and trap lasers needed to be much further apart in wavelength in order to hope for better results.

6.3.3 Force field detection

Having a chain of atomic oscillators spaced by half an optical wavelength ($a \sim 420$ nm) offers a unique setting to detect sharply varying force fields. Potential applications include the detection of the short-range gravitational forces, a fundamental part
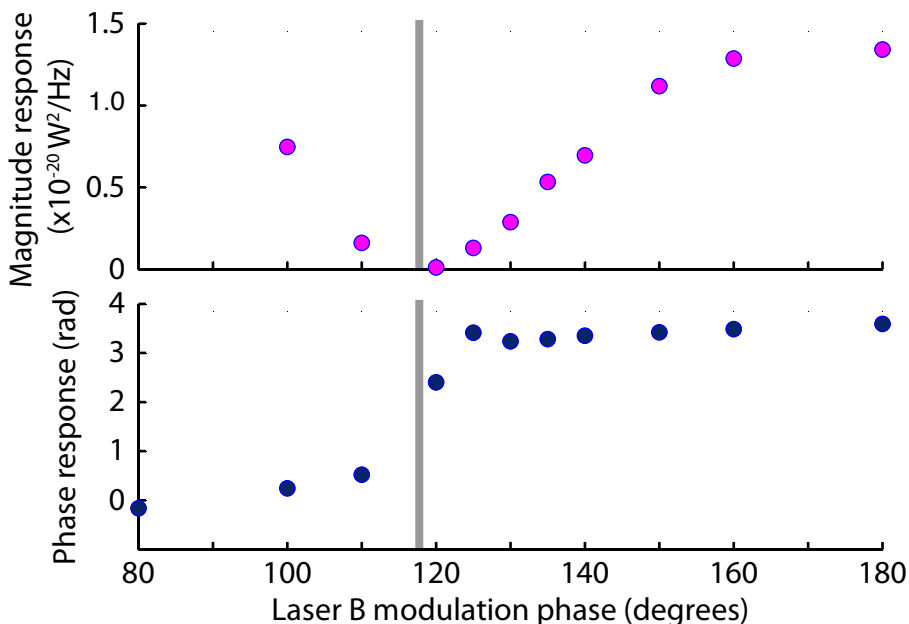
Figure 6.3: Calibration of laser B's modulation phase for force cancellation at a targeted lattice site. Figures show the coherent optomechanical response from atoms at that targeted site for various laser B phases. Gray lines highlight optimal phase for one particular modulation amplitude.
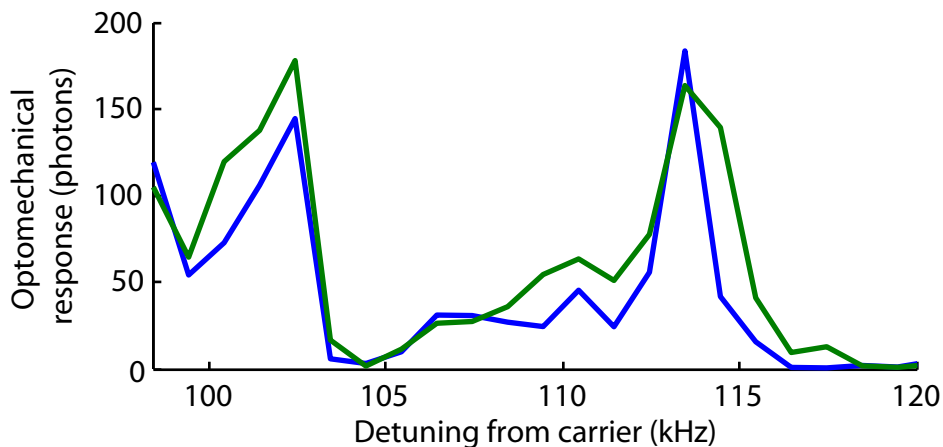

Figure 6.4: Unsuccessful force modulation cancellation. Figure displays the spectrum of optomechanically scattered probe photons ($= S_{a_-a_-}^{(F)}(\omega) \times \omega_{\mathrm{BW}}$) under combined resonant force driving from laser B and the probe at both occupied lattice sites, $\omega_{m,(1,2)} = 2\pi \times (102.5, 114)$ kHz, simultaneously. Force parameters were optimized to yield a null net force at site $\omega_{m,1} = 2\pi \times 102.5$ kHz (blue) and $\omega_{m,2} = 2\pi \times 114$ kHz (green), respectively.

of the Standard Model, and of the Casimir-Polder force. A much less ambitious goal was put forward as a first demonstration of this capability: measuring the spatial variation in the confining static force applied by one of the trap lasers, specifically laser B ($\bar{F}_B$).

As shown in Eqs. 6.10–6.11, optical force modulations applied at each lattice site are proportional to the local static optical forces. Resonant collective atomic responses to a particular drive amplitude applied on laser B is therefore expected vary between sites as the static optical force applied by B changes. Moreover, by simultaneously applying several equal-amplitude modulations, each resonant with a different lattice site's oscillation frequency, the entire array of atomic oscillators can be simultaneously driven and optomechanically probed, leading to parallel sensing of laser B's force field. The measurement can also be interpreted as sensing the summed force distribution from all other sources that offset laser B at each lattice site, most prominently laser A but also, to a limited extent, the probe's static force and the Earth's gravitational field (science cavity was oriented vertically - see Ref.[50]).

Initial experimental efforts focused on parallel force sensing at three neighboring and distinguishable lattice sites. A collection of ~ 500 to 1000 atoms were loaded at each site. The collective atomic motion at each site was then resonantly driven at the same time by applying three calibrated intensity modulations on laser B. The trio of oscillators were weakly probed while being driven. From the superlattice model presented in Section 4.4, $\bar{F}_B$ was predicted to change by $\sim 5\%$ from one site to the next. This relatively low site-to-site force variation was not surprising considering λ_A and λ_B were relatively similar, meaning the lattice spacing $a \sim \lambda_B/2$. Unfortunately, the relative statistical uncertainties in the measured static forces at all three locations, extracted from the optomechanical responses, were between 5% and 10%. The predicted variation in $\bar{F}_B$ could therefore not be distinguished from the measurement noise.

Parallel force field sensing at three neighboring lattice site was abandoned in favor of sequential force sensing at three distant lattice sites, such that the expected distribution in $\bar{F}_B$ could be precisely resolved. One lattice site from three consecutive regions of the two-color FORT with maximal linear optomechanical coupling to the probe field ($\phi_{(1,2,3)} \sim \pi/4$) were chosen as targets. The targeted sites were therefore spaced by $\sim 2.3\,\mu$m, too far spaced to simultaneously load all three sites with an atom-chip-prepared cloud (hence the need for sequential sensing). During experiments, atoms were first loaded into the optical superlattice; the three targeted sites were sequentially loaded over three experimental iteration. At each iteration, the atoms were simultaneously driven by modulating laser B with a calibrated tone, $A_B \sin(\omega_{\mathrm{mod,B}} t)$, and optomechanically sensed. In order to avoid driving one site slightly off from its mechanical resonance, $\omega_{\mathrm{mod,B}}$ was discretely scanned across each site's resonance over a series of nine measurements; the modulation frequency was kept fixed at each measurement, but incremented by $2\pi \times 500\,\mathrm{Hz} < \Gamma_{\mathrm{inh}} \sim 2\pi \times 1\,\mathrm{kHz}$ from one measurement to the next. A total of 10 scans across each targeted site's resonance
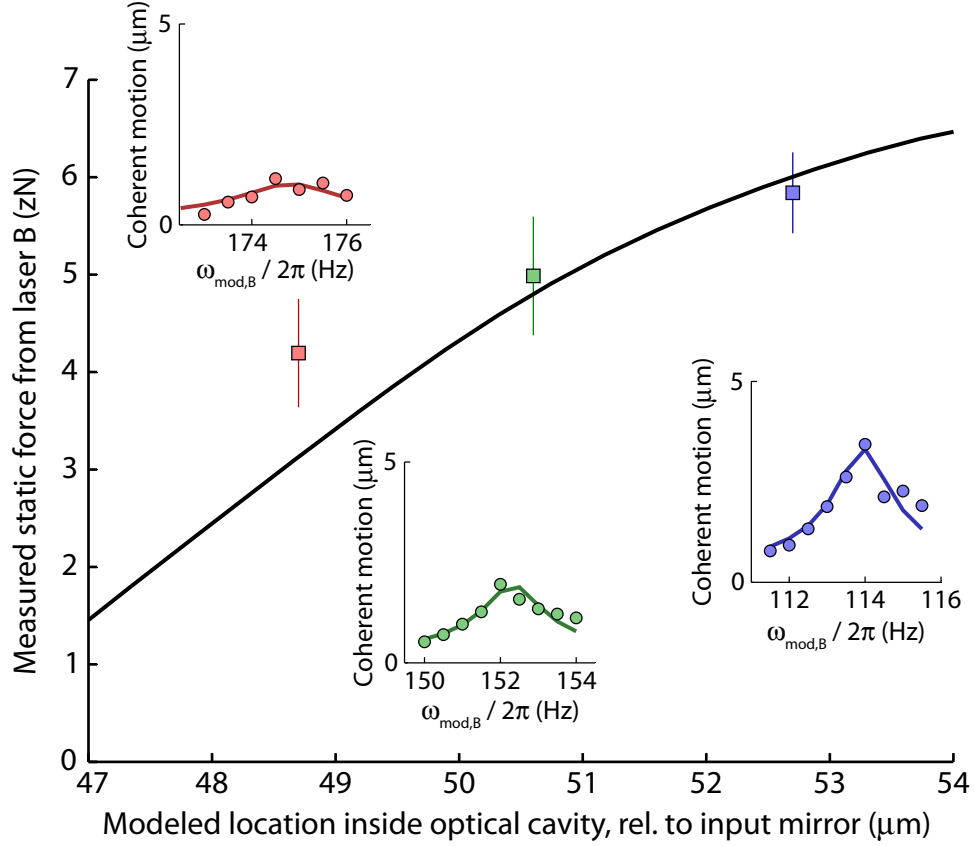
Figure 6.5: Sequential force field sensing. Figure shows the measured static per-atom force applied by laser B, $\bar{F}_B$, applied at three distant lattice sites, as well as the expected distribution of $\bar{F}_B$ over many sites (black line). Each targeted site's location was modeled based on the atom-chip-produced magnetic trap and the chip's approximate distance from the input mirror, similarly to Fig. 4.10. (Insets) Measured coherent displacement of each atomic oscillator in response to each of the applied force modulations ($= \left\langle \hat{\bar{Z}}_{\text{CM},j}^{(F)}(\omega_{\text{mod,B}}) \right\rangle \cdot \omega_{\text{BW}}/A_B$).

were collected and averaged together. Both $\bar{F}_B$ and $\left\langle \hat{\bar{Z}}_{\text{CM},j}^{(F)}(\omega_{\text{mod,B}}) \right\rangle \cdot \omega_{\text{BW}}/A_B$ were extracted from the average coherent response at each of the twenty seven modulation frequencies.

The experimentally measured static forces did show a visible spatial variation, one which agreed reasonably well with the modeled superlattice structure (see Fig. 6.5). All three measured $\bar{F}_B$, however, were within statistical uncertainties of each other, which somewhat limited the result's impact. In addition, the measured variation was approximately half as steeped as expected for reasons unknown. Due to both of these limitations, as well as the narrow application of the method, these results were not

included as part of Ref. [39].

6.4   Chasing down noise and excessive heating

When an optical superlattice was first formed inside the science cavity, atoms were found to be hot. Their temperatures were recorded to be as much as ~ 5 times higher than in the single-color FORT. This initiated a long chase through the lock chain's forest of noise sources. The search for culprits is outlined below in roughly chronological order. The eventual conclusion was that noise was due to a combination of excessive noise on the trap lasers, caused primarily by secondary optical modes in the laser diodes (*i.e.* nearby laser mode hops), the atoms' linear susceptibility to optical amplitude noise when confined in a two-color FORT, and the relative weak confinement at regions of equal and opposite trap potentials in a balanced superlattice ($U_A = U_B$).

Early in the process, heating was observed to be lower at certain "magical" wavelengths of trap light, both on laser A and B. There was, however, no trend to these "magical" wavelengths. Moving as little as 1 GHz, about a FSR of the science cavity, could yield a noticeably colder cloud, while moving a full nanometer would return the cloud to an absurdly hot temperature. These wavelengths tests were primarily made without locking to the transfer cavity in order to save time.

After finding a few reasonable pairs of operating wavelengths, the lock chain was applied in full, with trap lasers locked to the transfer cavity. Surprisingly, initial measurements showed atoms were hotter when the lasers were "narrowed" on the transfer cavity. Investigative efforts immediately turned to the lasers and their locks. Several routes were taken, including optimizing the optical feedback in both trap lasers' housing, optimizing the various gains and frequencies used as part of their respective closed-loop feedback circuit, and carefully adjusting the parameters of the science cavity - laser B lock. The combination of changes only made marginal improvements on the atoms' temperature.

Faced with virtually no success after going down the list of obvious solutions, random changes started being applied. One of them turned out to be particularly fortuitous. For a given pair of trap wavelengths and decent locking conditions, the loading point of atoms into the superlattice was changed. Time-of-flight images showed drastically different temperatures both locations. After carefully modeling the superlattice and conducting additional tests, the root causes of this variation in temperature were attributed to variations in ω_m across the superlattice and the atoms' linear susceptibility to trap noise. Superlattice sites with the largest ω_m hold colder atoms not only because they have deeper potentials with which to confine atoms, but also because atoms inserted at these sites have minimal linear coupling to static optical forces from the trap lasers. These conclusions seem obvious at this point of the chapter, after detailing much of the experimental efforts, but unfortunately required much
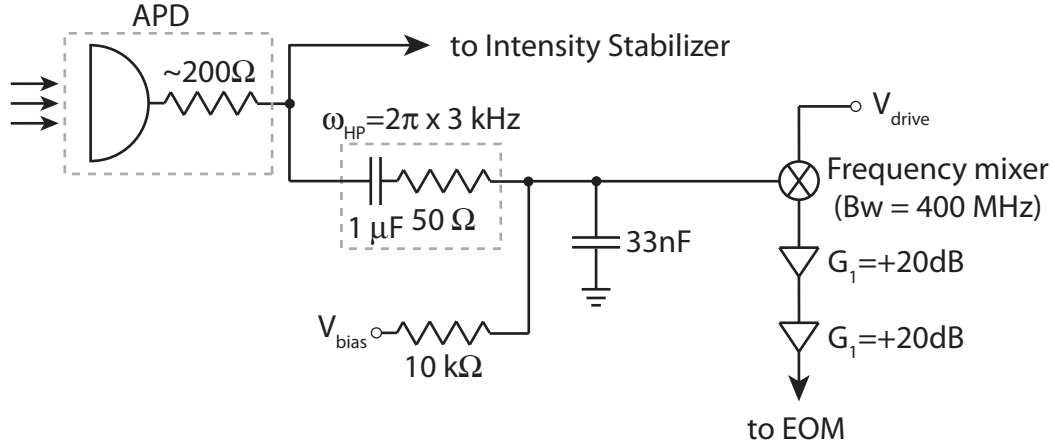
Figure 6.6: Added intensity-stabilization circuit, in transmission of the science cavity, for laser A. An EOM was added to laser A's cavity-bound path, with sidebands produced by mixing a direct-current (DC) voltage (V_{bias}) with a frequency modulation (V_{drive} - 200 MHz, 8.4 dBm). The EOM carrier was placed on science-cavity resonance and served as A's intracavity optical potential; laser A's sidebands were both significantly detuned from science-cavity resonance. Intensity fluctuations above $2\pi \times 3$ kHz recorded by laser A's APD in transmission of the science cavity were added to V_{bias} and fed back to the EOM using the above circuit. Detected intensity increases (decreases) were compensated by the feedback circuit by taking optical power out of EOM carrier (sidebands) and into the EOM sidebands (carrier). Bw = bandwidth.

investigative work when first developing the experimental setup.

This important finding guided the remaining preparation work. Since the spectral distribution of laser noise tends to fall off as a function of frequency, atoms with larger ω_m are typically less perturbed by trap laser noise. However, increasing each laser's power, *i.e.* U_A and U_B, so as to increase ω_m ($\propto \sqrt{U_A}, \sqrt{U_B}$) only helps alleviate laser-induced heating if the noise spectral distribution drops faster than $1/\omega^2$. A balance was struck between the noise distribution of each laser, including known technical noise spikes at certain frequencies, and the total trap light available, yielding $\omega_{m,A,B} = 2\pi \times (127$ kHz, 128 kHz$)$. Laser A continued to transmit a significant amount of heat to atoms. A direct intensity feedback loop (Fig. 6.6), involving only passive electronic components with minimal cabling in order to maximize the feedback bandwidth, was therefore added in parallel to laser A's initial intensity-stabilization circuit in transmission of the science cavity (see Fig. 4.4). The added construction was found to have minimal impact on the atoms' temperature and, consequently, removed from the setup. What did have a substantial impact and finally ended the noise chase was a slight adjustment of the laser diode A's current, an indication that the diode was operating near a mode hop.

Chapter 7

Summary and future endeavors

This final chapter provides a brief summary of the major achievements emanating from the two experimental efforts discussed in this dissertation (Chapters 5–6). Unanswered questions left behind by these experiments are also highlighted, leading to a short list of possible future research avenues.

7.1   Summary

The single-oscillator and multi-oscillator experiments presented in this dissertation provided one of the first in-depth looks at quantum features in cavity optomechanics. Several important findings were reported, including the observation of zero-point motion of a collective atomic mode of motion, the experimental validation of an atom cloud's thermodynamic evolution under constant probing, the demonstration of quantum-limited optomechanical measurement backaction, *i.e.* the increase in $\bar{\nu}$ due to the probe's quantum optical fluctuations, and the ability to selectively transfer, store and detect a coherent mechanical state in a single, targeted mechanical element within an array of elements. However, perhaps the most important achievement, one that connects both projects, is the experimental demonstration that an atoms-based setup can reliably produce a tunable and near-ground-state mechanical system for the purpose of quantum studies in cavity optomechanics. On any given day, the experimental apparatus described herein could be tuned to produce one or many mechanical elements, each near its motional ground state, with a desired site-to-site variation in mechanical resonance frequency and optomechanical cooperativity. Moreover, the type of coupling to the probe could also be selectively controlled, from very dominantly linear ($\phi = \pi/4$) to dominantly quadratic ($\phi = 0 \operatorname{or} \pi/2$), as was done in Ref. [54]. This versatility, unique to atoms-based systems, is in large part responsible for the wide variety of distinctly quantum features in cavity optomechanics reported by the Stamper-Kurn group.

The many answers provided by the single-oscillator and multi-oscillator experiments also brought upon several questions, both technical and fundamental, some of which are still unanswered. Two of these remaining question marks are particularly noteworthy: what physical characteristics define native mechanical damping rate, Γ_m, and the observed, broadened mechanical linewidth, Γ_{inh}, and why does the observed optomechanical response of atoms decay over time, becoming indistinguishable from quantum fluctuations of the probe field at long times? Tying both of these loose ends will be particularly important for future experiments that aim to build on the results presented in Chapters 5–6. The challenge of resolving these issues is likely technical rather than fundamental in nature, and will yield information specific to the present experimental system. However, gaining experimental control over the mechanical damping rate and the steady-state optomechanical response will be useful for all future studies (*i.e.* system non-specific) of fundamental features of cavity optomechanics.

7.2 Future endeavors

In this final section, I propose a series research paths that follow from the contents of this dissertation. Each suggested topic is motivated by highlighting its relevance to one or more active scientific communities. The topics are are approximately ordered in a chronological form, from near-term priorities to longer-terms objectives.

7.2.1 The physics behind collective motional damping

In solid-state micro- and nanomechanical systems, understanding the physics behind motional damping has received much scientific interest recently [86, 87]. Carrying this interest over to atomic physics appears natural in the context of atoms-based cavity optomechanics. Speculations are that Γ_m for a collectively moving ensemble of atoms is predominantly defined by atom-atom collisions. In addition, numerous possible sources of inhomogeneous broadening have been proposed to explain the observed Γ_{inh} (see Section 5.4). Some of these sources of broadening are expected to be asymmetric in frequency, favoring lower-frequency oscillation, such as the anharmonic spacing between the FORT's energy levels (see Sec. 7.2.3), and the radial spread of atoms. The exact origins of Γ_m and Γ_{inh} likely lie at the intersection of cold-atoms physics, many-body dynamics and nonlinear mechanics, making this a complex and intriguing research topic, relevant to multiple atomic physics communities. Developing a reliable model for Γ_m and Γ_{inh}, one that would help predict the damping rates for various experimental realizations (*e.g.* scaling with atom number), promises to greatly benefit atoms-based cavity optomechanics by allowing future experiments to be planned around a particular Γ_m and providing solutions to what is today a rather limited mechanical quality factor ($Q = \omega_m/\Gamma_m \sim 250$, $Q_{\text{inh}} = \omega_m/\Gamma_{\text{inh}} \sim 50$).
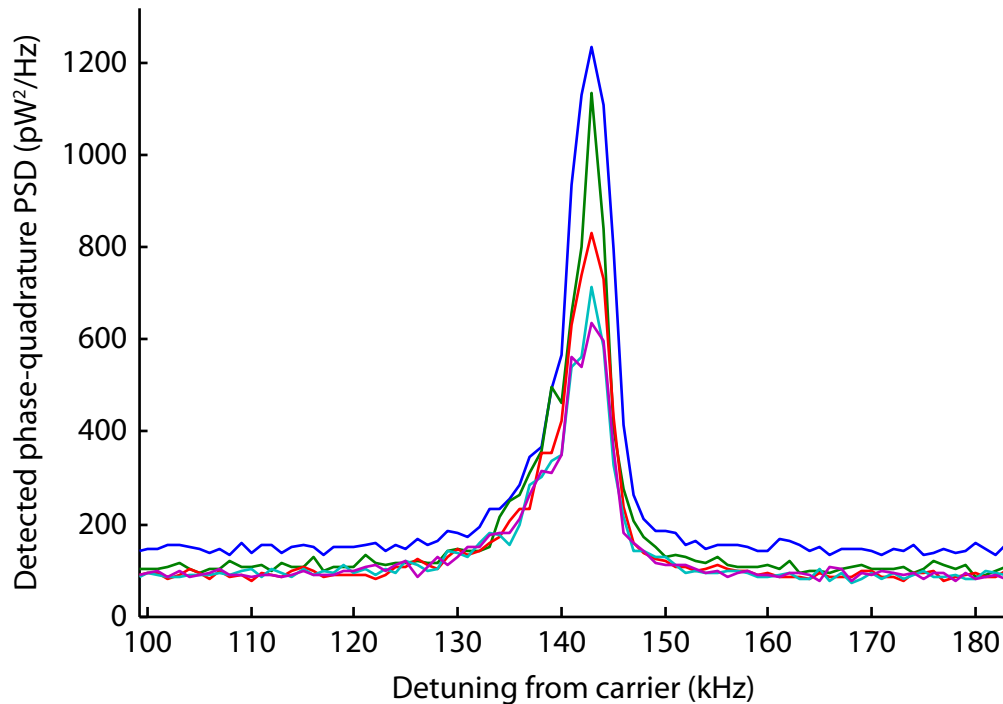
Figure 7.1: Decay in optomechanical response over time. The figure shows a typical example of the observed reduction in optomechanically scattered photons over time. Five different time intervals following the injection of probe light into the cavity are displayed: 1-2 ms (blue), 2-3 ms (green), 3-4 ms (red), 4-5 ms (turquoise), 5-6 ms (pink).

7.2.2 Optomechanical responses at long times

As eluded in Section 7.1, optomechanical responses were observed to consistently decay over time (Fig. 7.1) until, finally, being indistinguishable from the detected shot-noise floor. The timescale over which optomechanical data was considered sufficiently reliable for analysis was the first ~ 10 ms of probing for $C_{\mathrm{OM}} \sim 1$. This observed decay, unexplained by linear cavity optomechanics theory, has been a considerable limitations, in particular causing a lengthy total acquisition time of adequate levels of statistics, with a maximum yield of ~ 10 ms of data for each ~ 40-second-long experimental iteration.

Exploring the reasons of this decay should fall high on the list of future experimental roads. Findings will not only improve the quality and reliability of experimental data, but will also likely provide precious answers to fundamental questions. For instance, what happens to atoms and their collective motion during the decay of optomechanical response? Answers to this question might point to large motional dephasing due to atom-atom interactions, effectively breaking up the collective CM mode of motion, $\hat{Z}_{\mathrm{CM}}$, in favor of all other collective motional modes. Establishing this
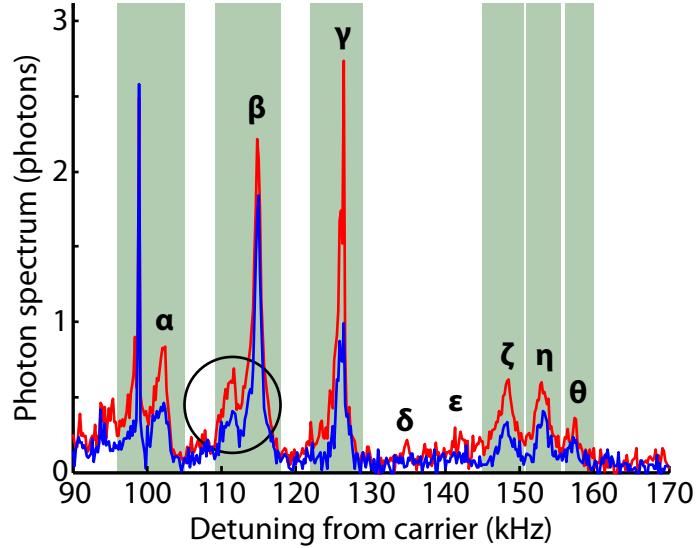
Figure 7.2: Possible evidence of anharmonic energy level spacing. This figure is a copy of Fig. (3) in the published preprint on multi-oscillator cavity optomechanics (Ref. [39]). The encircled "bump" in the observed spectrum is suspected to be Raman scattered photons from mechanical element β's first excited state, detuned to lower frequency from ground-state-scattered photons because of the trap potential's anharmonic energy level distribution.

possible connection would contribute to the previously stated goal of understanding the origins of Γ_m and Γ_{inh}. Answers might also point to optomechanically dependent dynamics, such as an influence of the probe-cavity detuning Δ on the observed decay rate. In any case, the findings will enhance capabilities of future atoms-based optomechanical experiments.

7.2.3 Anharmonic collective motion

The linear cavity optomechanical effects described in this previous chapters relied on approximating the sinusoidal optical potential that traps and confines atoms as a harmonic potential. However, a more complete model of the experimental system must include the anharmonic features naturally present in the system. Evidences of anharmonic effects have been indirectly observed in Fig. 5.2 and Fig. 6.1, and even suspected as part of published results (Fig. 7.2). These observations remain sporadic and poorly understood.

Acquiring a better handle on the anharmonicity present in atoms-based realizations of cavity optomechanics will considerably further explorations of quantum motion. First, signatures of nonlinear quantum motion could conceivably be detected. Observations of anharmonic motion in time would of course be a prime objective,

but one difficult to realize given the incoherent nature of quatum-driven oscillations. Observations in the frequency domain, on the other hand, could be straightforward: by having a distinguishable mechanical resonance for every motional energy state, the occupation of each state within the collective nonlinear oscillator could be individually detected, as proposed in Fig. 7.2. This would enable any superposition of motional energy states to be directly imaged, thereby also enabling a new type of optomechanical thermometer based on the relative occupation of each energy state r:

$$\nu_r = e^{-r\hbar\omega_m/k_B T}\left(1 - e^{-\hbar\omega_m/k_B T}\right). \tag{7.1}$$

Second, anharmonic motion could be harnessed for the purpose of quantum information. Indeed, by spectrally isolating two motional energy levels, coherent exchange of quantum information between these two states becomes possible, as was done for superconducting qubits nearly 15 years ago [88]. Here, in the case of anharmonic optomechanical systems with ground-state oscillators, bits of information would be stored in the motional degrees of freedom, with the benefits of relatively small damping rates, and accessed by the light field. This would build on a recent experimental demonstration of the ability to exchange one bit of quantum information between a superconducting qubit and a nanomechanical resonator [34].

7.2.4 Quantum-limited measurements

As detailed in Chapter 1, the initial development of cavity optomechanics was in large part motivated by the perspective of enhanced measurement sensitivity for the purpose of gravitational wave detectors, in particular the ability to reach and potentially surpass the "standard quantum limit" (SQL). Ironically, decades later, the experimental demonstration of an optomechanical sensor operating at its optimal quantum sensitivity (*i.e.* at the intersection of the shot-noise and backaction limits - defined below) remains outstanding. This challenging demonstration, arguably the Holy Grail of optomechanics, is now within experimental reach.

As discussed in Chapter 6 (see Eqs. 6.15–6.19), a mechanical element in a cavity optomechanical is susceptible to externally applied forces as well as perturbations from the optical probe and its surrounding thermal environment. In the context of force detection, using the common "signal-to-noise ratio" (SNR) terminology, the optomechanically imprinted response to an applied force, $S_{a_-a_-}^{(F)}(\omega)$, forms the "signal," while the additional response caused by incoherent perturbations, $S_{a_-a_-}^{(\text{pert})}(\omega)$, constitutes the "noise." If the element's native motion is dominantly driven by incoherent quantum fluctuations, $S_{a_-a_-}^{(\text{pert})}(\omega) = S_{a_-a_-}^{(\text{inh})}(\omega)$, then corresponding force measurements are said to be at the SQL.

As with any quantum-limited measurements, SQL force measurements have a SNR peaked at one particular optomechanical cooperativity, which sets the optomechanical sensor's optimal operating point. Below this optimal cooperativity, the mechanical
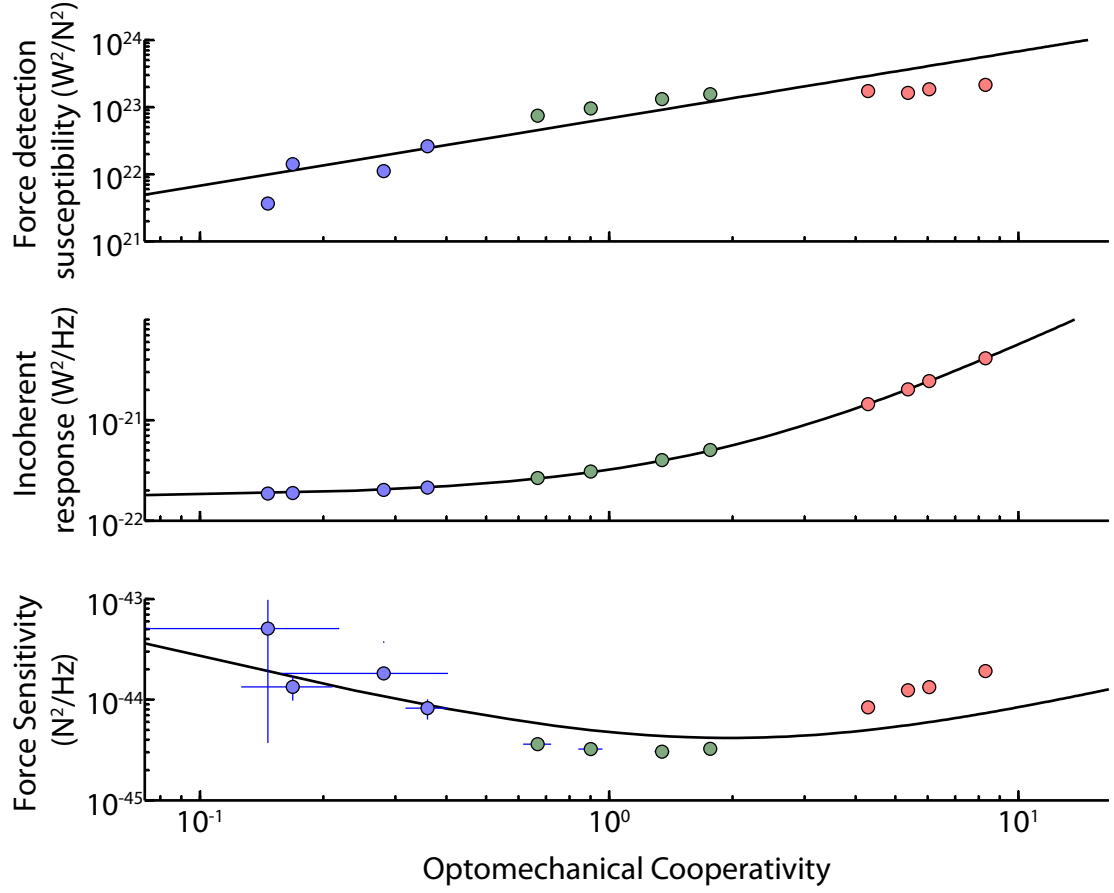
Figure 7.3: Standard-quantum-limited force sensing. Shown in the figure are the detection system's susceptibility to the applied force, $\chi(\omega_{\mathrm{dr}})$ (top panel), the measured atomic response to incoherent optical and mechanical noise, $S_{\mathrm{dem}}^{(\mathrm{het,inh})}(\omega_{\mathrm{dr}})$ (middle panel), and the detection system's overall noise-to-signal force measurement sensitivity $= S_{\mathrm{dem}}^{(\mathrm{het,inh})}(\omega_{\mathrm{dr}})/\chi(\omega_{\mathrm{dr}})$ (lower panel), as function of optomechanical cooperativities, C_{OM}. Each experimental condition's C_{OM} is determined from fits to the observed incoherent response in order to account for possible fluctuations in experimental conditions. Statistical uncertainties from these fits are used to derive error bars on the quoted force sensitivities. Three different probe detunings from atomic resonance were applied in order to cover a sufficient range of C_{OM}, : $\Delta_{\mathrm{ca}} = -70$ GHz (blue), $\Delta_{\mathrm{ca}} = -40$ GHz (green), $\Delta_{\mathrm{ca}} = -12$ GHz (red). The black line corresponds to the predicted force-sensing SQL based on linear optomechanical theory.

element's motion is too weakly sensed, leading to a sub-optimal $S_{a_- a_-}^{(F)}(\omega)$ that limits the attainable SNR. This measurement regime is known as the "shot-noise-dominated regime." Above the optimal cooperativity, the probe becomes the dominant incoherent drive; the signal ($S_{a_- a_-}^{(F)}(\omega) \propto C_{\mathrm{OM}}$) begins to scale less favorably than the

probe-induced noise ($S_{a-a-}^{\text{(inh)}}(\omega) \propto C_{\text{OM}}^2$), a measurement regime appropriately termed "backaction-dominated regime." Optimal detection thus sits at the intersection of both measurement regimes.

Recent work in the Stamper-Kurn group has provided an initial indication that quantum-limited force detection could be achieved using an atoms-based realization of cavity optomechanics. Preliminary results show that an applied force modulation, generated through intensity modulations of laser beam B in a two-color FORT (as described in Section 6.3) and nearly resonant with one distinguishable atomic oscillator, can be optomechanically sensed at the SQL across the transition from shot-noise-limited to backaction-dominated regimes using a single atomic oscillator (Fig. 7.3). The findings are based on measurements of the atoms' collective incoherent response, $S_{\text{dem}}^{\text{(het,inh)}}(\omega_{\text{dr}})$, and the detection system's susceptibility to the applied force, $\chi(\omega_{\text{dr}})$, at the modulation frequency, ω_{dr}, using a cavity-resonant probe ($\Delta = 0$):

$$S_{\text{dem}}^{\text{(het,inh)}}(\omega_{\text{dr}}) = \epsilon\hbar\omega_p \cdot 2\kappa S_{a-a-}^{\text{(inh)}}(\omega_{\text{dr}}) = \frac{\epsilon\hbar\omega_p}{2\pi}\frac{C_{\text{OM}}}{2}\frac{\Gamma_m^2(C_{\text{OM}} + 2\bar{\nu}_{\text{th}} + 1)}{(\omega_{\text{dr}} - \omega_m)^2 + (\Gamma_m/2)^2}, \quad (7.2)$$

$$\chi(\omega_{\text{dr}}) = \frac{S_{\text{dem}}^{\text{(het,F)}}(\omega_{\text{dr}}) \times \omega_{\text{BW}}}{F_{\text{RMS}}^2(\omega_{\text{dr}})} = \frac{\epsilon\hbar\omega_p \times 4\kappa S_{a-a-}^{(F)}(\omega_{\text{dr}}) \times \omega_{\text{BW}}}{\left(\bar{F}_B(z_{\text{min}})A_B\right)^2}, \quad (7.3)$$

$$= \frac{\epsilon\hbar\omega_p C_{\text{OM}}}{2\Gamma_m P_{\text{HO}}}\frac{(\Gamma_m/2)^2}{(\omega_{\text{dr}} - \omega_m)^2 + (\Gamma_m/2)^2}. \quad (7.4)$$

In Eqs. 7.2–7.4, the unresolved sideband limit, $\omega_{\text{dr}} \ll \kappa$ was applied: $\kappa^2 + \omega_{\text{dr}}^2 \sim \kappa^2$. Continued work to confirm these results and expand on the cavity's role during measurements (*e.g.* attempting such force measurements away from cavity resonance) is bound to have a profound impact on the optomechanics community and the quantum metrology community in general.

7.2.5 Longer-term experiments in a one-dimensional cavity-based lattice

The creation of an array of atomic ensembles with near-ground-state collective motion provided an important first exploration of quantum cavity optomechanics with multiple mechanical elements. Framing the realization in a larger picture, one that includes future applications of cavity optomechanics, such as tests of quantum mechanics at "macroscopic" scales and the development of quantum devices, the achievement was a relatively small step. As cavity optomechanics continues to make small important steps towards big-picture goals, it could no doubt benefit from longer-term involvement of cold-atoms-based constructions.

Examples of future experimental demonstrations that could potentially be achieved using cold atoms include the optical detection of a non-classical motional state (*e.g.* a motional Fock state), the ability to transfer quantum information between two

mechanical oscillators using light as a communication link, and the generation of entanglement between two "large size" mechanical objects, an important result for the field of quantum optics at large. Having a distributed series of cold atomic samples within an optical cavity, where light-mediated interactions are effectively infinite range, also enables optomechanics-type experiments relevant to atomic physics, in particular many-body physics. For instance, an atoms-based Newton's cradle could be experimentally examined. The idea here would be to apply a displacement on one collective atomic ensemble and examining the impact of this perturbation on other mechanically resonant ensembles. Moving further away from optomechanics, the infinite range interactions being considered need not be limited to the atoms' mechanical degree of freedom: they can include all fundamental aspects of the atoms, such as their spin and their fermionic/bosonic nature.

Regardless of the set goals of future experiments, the physics at play is likely to be completely different. After all, that is how the Stamper-Kurn group serendipitously started what is now nearly a decade-long series of fruitful investigations on cavity optomechanics.

Appendix A

Linear optomechanical amplifier model

The main text of the publication entitled "Linear amplifier model for optomechanical systems" (Ref. [40]) is included below. This work describes some of the fundamentals behind optomechanical interactions and complements the theory present in Chapter 2. The style format of the following appendix matches that the dissertation, not that of the published manuscript. However, the nomenclature, symbols and definitions used in the original publication are repeated here. In particular, the Fourier-transform and quadrature-operators definitions applied in this appendix are not normalized, contrary to the definitions used in the main body of the dissertation (see Section 2.2).

Cavity optomechanics [89, 90] describes the macroscale effects of radiation pressure on moveable reflective and refractive media [3, 6] with cavity-based optical feedback. Research in the field today is conducted on several fronts, from nano- [83, 91, 92] and micro-fabricated [55, 93, 94] devices to atomic gases [29, 30] to kilogram-size mirrors [95, 96], and from microwave to optical frequencies. Efforts to elucidate the classical and quantum nature of optomechanical systems have led to demonstrations of sideband cooling [25, 26, 27, 97, 98], amplification [25, 99] and backaction evasion [100], observations of the optical spring effect [101], quantum-sensitive force detection [31, 32], explorations of optical nonlinearity and bistability [54], and studies of ponderomotive squeezing [102] and classical analogs thereof [103, 104]. In the past year, further experimental advances also generated the first ground-state oscillators [34, 35] and led to the observation of mechanically induced optical transparency [59, 60].

To date, these varied research avenues have been modeled individually. Works highlighting a particular aspect of optomechanics are often prefaced by extensive derivations to set the context. This effectively isolates different aspects of the same optomechanical interaction, making it difficult to establish the connections between them.

Here, we present a framework that treats these disparate phenomena in a unified manner. Cavity-mediated interactions between a harmonic oscillator and a circulating light field are modeled as a feedback circuit. This allows the use of concepts from control theory. Optomechanical systems are therefore represented as linear optical and mechanical amplifiers with frequency-dependent gain. We study the amplifier response to optical and mechanical inputs for the general case of a two-sided cavity with losses. Results include a connection between ponderomotive squeezing [20, 102, 103, 104, 105, 106] and optomechanically induced transparency (OMIT) [59, 60, 107]. The amplifier model is also used to set quantum limits on the transduction of external mechanical drives.

A.1   Model of Optomechanical Interaction

We consider a two-sided optical cavity containing one optical element that is moveable and harmonically bound. The element may be one of the cavity mirrors, or an intracavity dispersive element placed at a linear gradient of the light field [108]. Light circulating inside the cavity couples parametrically with the position of the harmonic oscillator. The system is described by the Hamiltonian

$$H = \hbar\omega_c\hat{a}^\dagger\hat{a} + \hbar\omega_m\hat{b}^\dagger\hat{b} + \hbar\,g_{\mathrm{om}}\,\hat{z}\hat{a}^\dagger\hat{a} + \hat{H}_\kappa + \hat{H}_\gamma \;, \tag{A.1}$$

where ω_c (ω_m) and $\hat{a}$ ($\hat{b}$) are the resonant frequency and the annihilation operator of the cavity (oscillator) field, respectively. The first two terms of Eq. A.1 represent the energy stored in the photon and phonon fields. The final two terms, $\hat{H}_\kappa$ and $\hat{H}_\gamma$, contain the connections to external photon and phonon baths, respectively. Constant energy offsets are ignored.

The third term in Eq. A.1 captures the optomechanical interaction, where $\hat{z} = \hat{b}+\hat{b}^\dagger$ is the dimensionless position operator of the oscillator and g_{om} sets the coupling strength. The interaction has a clear signature of three-wave mixing, with intermodulation between two optical field operators and one mechanical field operator. This fundamentally nonlinear (three-wave) coupling can be linearized about an equilibrium position displacement z_0 caused by a dominant optical pump field $\hat{a}_0 e^{-i\omega_p t}$ rotating at frequency ω_p:

$$\begin{aligned}
\hat{z} &\rightarrow z_0 + \hat{z} \;, \\
\hat{a} &\rightarrow (a_0 + \hat{a})\,e^{-i\omega_p t} \;.
\end{aligned} \tag{A.2}$$

For simplicity, we set $a_0 = \sqrt{n}$ to be real, with n being the mean intracavity pump photon number. The resulting linearized optomechanical interaction energy can be written in two parts:

$$H_{\mathrm{static}} = \hbar g_{\mathrm{om}}\left(z_0 n + n\hat{z} + \sqrt{n}\,z_0(\hat{a} + \hat{a}^\dagger)\right) \;, \tag{A.3}$$

describing static changes in the cavity resonance frequency and the oscillator position, and

$$H_{\text{dyn}} = \hbar g_{\text{om}} \left(\sqrt{n}\, \hat{z}(\hat{a} + \hat{a}^\dagger) \right) \ , \tag{A.4}$$

corresponding to linearized dynamics. Eq. A.4 shows that the effective linear coupling between $\hat{z}$ and $\hat{a}$ is mediated by the pump field $\sqrt{n}$, with optical sidebands interpreted as signals and phonon modes as idlers.

The exchange of information between the circulating light field and the oscillator, captured by H_{dyn}, leads to dynamical backaction [90] or, in the language of control-systems engineering, feedback. To model this feedback, we introduce conjugate quadratures for both field fluctuation operators:

$$\hat{b}_+ = \hat{z} = \hat{b} + \hat{b}^\dagger \ , \qquad\qquad \hat{b}_- = \hat{p} = i(\hat{b} - \hat{b}^\dagger) \ , \tag{A.5}$$
$$\hat{a}_+ = \hat{a} + \hat{a}^\dagger \ , \qquad\qquad \hat{a}_- = i(\hat{a} - \hat{a}^\dagger) \ .$$

Operators $\hat{z}$ and $\hat{p}$ represent the dimensionless position and momentum fluctuation operators of the oscillator, while $\hat{a}_+$ and $\hat{a}_-$ are the amplitude modulation (AM) and phase modulation (PM) quadratures of the intracavity optical field. Time evolution of these operators is provided by the Heisenberg equations in a frame co-rotating with the pump field:

$$\begin{pmatrix} \dot{\hat{a}}_+ \\ \dot{\hat{a}}_- \\ \dot{\hat{z}} \\ \dot{\hat{p}} \end{pmatrix} = \mathbf{M} \begin{pmatrix} \hat{a}_+ \\ \hat{a}_- \\ \hat{z} \\ \hat{p} \end{pmatrix} + \begin{pmatrix} \sqrt{\gamma_T}\, \hat{\alpha}_{\text{in}+} \\ \sqrt{\gamma_T}\, \hat{\alpha}_{\text{in}-} \\ \sqrt{\Gamma_m}\, \hat{\eta}_{\text{in}+} \\ \sqrt{\Gamma_m}\, \hat{\eta}_{\text{in}-} \end{pmatrix} \ , \tag{A.6}$$

where

$$\mathbf{M} = \begin{pmatrix} \mathbf{M}_a & \mathbf{T} \\ \mathbf{T} & \mathbf{M}_b \end{pmatrix} = \left(\begin{array}{cc|cc} -\kappa & \Delta & 0 & 0 \\ -\Delta & -\kappa & g_{\text{C}} & 0 \\ \hline 0 & 0 & -\frac{\Gamma_m}{2} & -\omega_m \\ g_{\text{C}} & 0 & \omega_m & -\frac{\Gamma_m}{2} \end{array} \right) \ . \tag{A.7}$$

The frequency $\Delta = \omega_p - \omega_c'$ corresponds to the pump detuning from cavity resonance (ω_c' includes the static shift contained in H_{static}), while $g_{\text{C}} = 2g_{\text{om}}\sqrt{n}$ defines the effective optomechanical coupling rate. Photonic and phononic perturbative inputs (outputs) are symbolized by $\hat{\alpha}_{\text{in}}$ ($\hat{\alpha}_{\text{out}}$) and $\hat{\eta}_{\text{in}}$ ($\hat{\eta}_{\text{out}}$), respectively. Operator $\hat{\alpha}_{\text{in}}$ ($\hat{\alpha}_{\text{out}}$) groups inputs (outputs) from the left and right ends of the cavity, $\hat{\alpha}_{\text{in},L}$ ($\hat{\alpha}_{\text{out},L}$) and $\hat{\alpha}_{\text{in},R}$ ($\hat{\alpha}_{\text{out},R}$), respectively, as well as from loss channels $\hat{\alpha}_{\text{in},V}$ ($\hat{\alpha}_{\text{out},V}$):

$$\sqrt{\gamma_T}\, \hat{\alpha}_{\text{in}} = \sqrt{\gamma_L}\, \hat{\alpha}_{\text{in},L} + \sqrt{\gamma_R}\, \hat{\alpha}_{\text{in},R} + \sqrt{\gamma_V}\, \hat{\alpha}_{\text{in},V} \ . \tag{A.8}$$

The optical damping rates through each port, γ_L, γ_R and γ_V, collectively define the cavity half-linewidth κ as $2\kappa = \gamma_L + \gamma_R + \gamma_V$. Analogously, communication between the mechanical oscillator and its environment takes place at a rate Γ_m.

Eqs. A.6–A.7 show that the oscillator momentum is susceptible to fluctuations in the intracavity photon number, while the induced phase shift on circulating photons is dependent on the oscillator position. The mutual optomechanical transduction, captured by the off-diagonal block matrix $\mathbf{T}$, leads to closed-loop feedback. The standard formalisms from control theory thus provide appropriate means to construct a complete yet simple model for optomechanical systems.

First, Eqs. A.6–A.7 can be translated into a time-domain block diagram, as shown in Fig. A.1(a). Such representations are analogous to earlier flow-chart depictions of optomechanical interactions [109]. Optomechanical interactions are shown as vertical lines of communication in Fig. A.1, between the otherwise freely evolving optical and mechanical fields.

Second, insight into the gains of the optomechanical feedback loop can be obtained by studying the evolution of field operators in frequency space, translating Eq. A.6 into a pair of governing equations[1]:

$$
\begin{pmatrix} \hat{\tilde{a}}_+ \\ \hat{\tilde{a}}_- \end{pmatrix} = \mathbf{F}_a \left[\mathbf{T} \begin{pmatrix} \hat{\tilde{z}} \\ \hat{\tilde{p}} \end{pmatrix} + \sqrt{\gamma_T} \begin{pmatrix} \hat{\tilde{\alpha}}_{\mathrm{in}+} \\ \hat{\tilde{\alpha}}_{\mathrm{in}-} \end{pmatrix} \right] ,
$$

$$
\begin{pmatrix} \hat{\tilde{z}} \\ \hat{\tilde{p}} \end{pmatrix} = \mathbf{F}_b \left[\mathbf{T} \begin{pmatrix} \hat{\tilde{a}}_+ \\ \hat{\tilde{a}}_- \end{pmatrix} + \sqrt{\Gamma_m} \begin{pmatrix} \hat{\tilde{\eta}}_{\mathrm{in}+} \\ \hat{\tilde{\eta}}_{\mathrm{in}-} \end{pmatrix} \right] ,
$$

(A.9)

where

$$
\mathbf{F}_a = \frac{1}{(\kappa - i\omega)^2 + \Delta^2} \begin{pmatrix} \kappa - i\omega & \Delta \\ -\Delta & \kappa - i\omega \end{pmatrix} ,
$$

(A.10)

$$
\mathbf{F}_b = \frac{1}{(\frac{\Gamma_m}{2} - i\omega)^2 + \omega_m^2} \begin{pmatrix} \frac{\Gamma_m}{2} - i\omega & -\omega_m \\ \omega_m & \frac{\Gamma_m}{2} - i\omega \end{pmatrix} .
$$

In Eqs. A.9, the intracavity photon (phonon) field is the sum of an optomechanical transduction of the intracavity phonon (photon) field and a cavity- (oscillator-) induced filtering of the $+$ and $-$ optical (mechanical) input quadratures, captured by $\mathbf{F}_a$ ($\mathbf{F}_b$). Eqs. A.9 are collectively represented by the block diagram shown in Fig. A.1(b).

By virtue of our approximations, the optomechanical amplifier model considered here is entirely linear; amplifier inputs and outputs can be completely parametrized by a set of transfer matrices. In typical optomechanics systems, only the optical field is detectable, so we will only give those transfer matrices that connect the inputs to the optical output. A key result of this paper is that many of the salient features of optomechanics depend only on these transfer matrices, and not on the specific nature of the drive fields or, among other possibilities, on the assorted experimental configurations by which many phenomena of optomechanical systems have been uncovered.

---

[1]The following Fourier transform convention is used: $\tilde{f}(\omega) = \int_{-\infty}^{\infty} f(t)e^{i\omega t}dt$
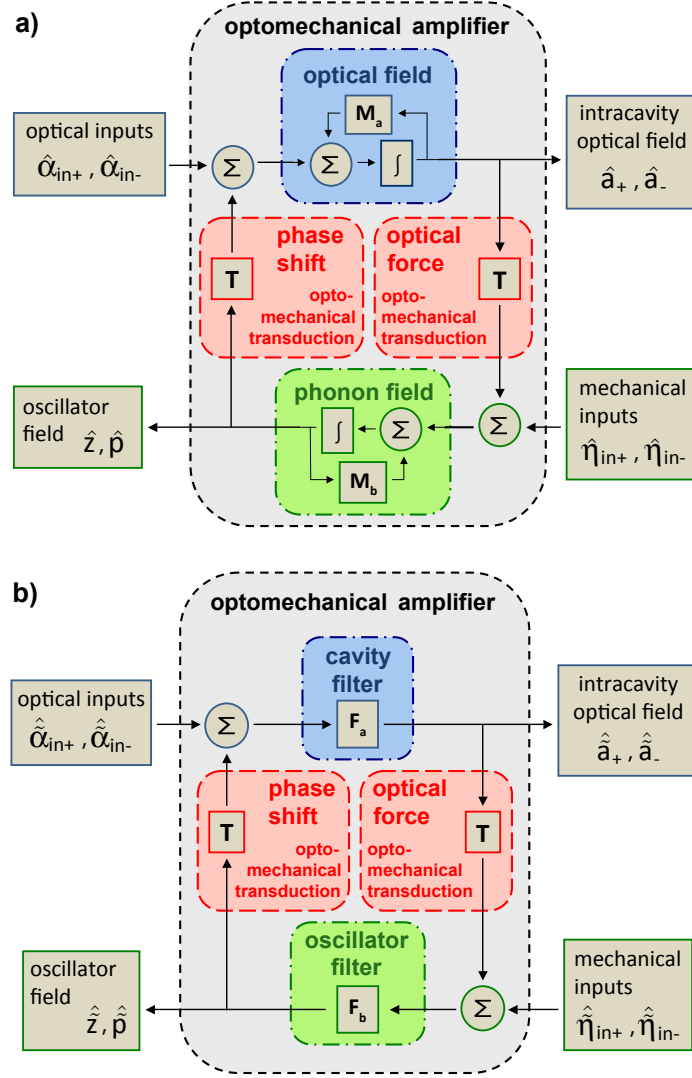
Figure A.1: Block diagram model of linear optomechanics in the (**a**) time domain and (**b**) frequency domain, as established in Eq. A.6 and Eq. A.9, respectively. The block matrices of Eq. A.6 and Eq. A.9 are shown in their respective circuit. Symbols $\sum$ and $\int$ represent the sum of two inputs and the time integral of an input, respectively. Linear optomechanical feedback takes place via the two center blocks (red), which connect the optical (blue) and mechanical (green) field evolution.

The optical output is

$$\begin{pmatrix} \hat{\tilde{a}}_+ \\ \hat{\tilde{a}}_- \end{pmatrix} = \mathbf{H}_\alpha \sqrt{\gamma_T} \begin{pmatrix} \hat{\tilde{\alpha}}_{\text{in}+} \\ \hat{\tilde{\alpha}}_{\text{in}-} \end{pmatrix} + \mathbf{H}_\eta \sqrt{\Gamma_m} \begin{pmatrix} \hat{\tilde{\eta}}_{\text{in}+} \\ \hat{\tilde{\eta}}_{\text{in}-} \end{pmatrix}. \tag{A.11}$$

The transfer matrices $\mathbf{H}_\alpha$ and $\mathbf{H}_\eta$ have units of inverse frequency, and can be calculated by solving Eq. A.9. The result is

$$\mathbf{H}_\alpha = \begin{pmatrix} 1 + H_{+\alpha} & 0 \\ H_{-\alpha} & 1 \end{pmatrix} \mathbf{F}_a, \tag{A.12}$$

$$\mathbf{H}_\eta = \begin{pmatrix} H_{+\alpha} & 0 \\ H_{-\alpha} & 0 \end{pmatrix} \begin{pmatrix} H_{+\eta} & H_{-\eta} \\ 0 & 0 \end{pmatrix}. \tag{A.13}$$

The individual matrix elements can be related to a common optomechanical gain G. For systems with high mechanical quality factors, where the damping-induced frequency pulling of the oscillator may be neglected, one finds:

$$G = \frac{-s(\omega)}{\omega_m^2 + s(\omega) - \omega^2 - i\omega(\Gamma_m + \Gamma_{\mathrm{opt}}(\omega))}, \tag{A.14}$$

$$H_{+\alpha} = G, \qquad\qquad H_{-\alpha} = G\,\frac{\kappa - i\omega}{\Delta}, \tag{A.15}$$

$$H_{+\eta} = -\frac{1}{g_C}\frac{\Gamma_m/2 - i\omega}{\omega_m}, \qquad\qquad H_{-\eta} = \frac{1}{g_C}. \tag{A.16}$$

In the above, $s(\omega)$ represents the stiffening of the oscillator due to optomechanics, and $\Gamma_{\mathrm{opt}}(\omega)$ represents an optomechanically induced damping rate:

$$s(\omega) = \frac{\omega_m \Delta g_C^2}{\kappa^2 + \Delta^2 - \omega^2}, \tag{A.17}$$

$$\Gamma_{\mathrm{opt}}(\omega) = \frac{2\kappa}{\kappa^2 + \Delta^2 - \omega^2}(\omega_m^2 - \omega^2). \tag{A.18}$$

The stiffening shifts the oscillator's resonant frequency to a value

$$\begin{aligned}\omega_{\mathrm{eff}}^2 &= \frac{1}{2}(\kappa^2 + \Delta^2 + \omega_m^2) - \frac{1}{2}\sqrt{(\kappa^2 + \Delta^2 - \omega_m^2)^2 - 4\omega_m \Delta g_C^2} \\ &\approx \omega_m^2 + s(\omega_m),\end{aligned} \tag{A.19}$$

where the approximation holds for small shifts of ω_{eff} from ω_m.

The properties of the amplifier can be parameterized by the optomechanical cooperativity, defined as $C_{\mathrm{opt}} = g_C^2/(\kappa\Gamma_m)$. The cooperativity allows comparison between optomechanical systems over a broad range of parameters. However, C_{opt} does not contain information about the detuning from cavity resonance. To draw comparison between systems operating away from cavity resonance, it is more convenient to adopt an "optomechanical damping parameter", defined as $D_{\mathrm{opt}} = \Gamma_{\mathrm{opt}}(\omega_{\mathrm{eff}})/\Gamma_m$.

In line with our earlier assumptions, Eq. A.11 holds only for linear and stable systems. In optomechanics, this condition is always satisfied when the optomechanically induced cavity resonance shift is small compared to the cavity linewidth ($g_C < \kappa$)

and when pumping to the red of cavity resonance ($\Delta \leq 0$), where backaction cooling dominates [19, 110, 111]; parametric instability can occur when pumping to the blue of cavity resonance [22, 25, 112, 111]. Eq. A.11 is consequently invalid under optical bistability, where the pump detuning can spontaneously transition between negative and positive values due to changes in the instantaneous cavity resonance frequency.

Eq. A.11 represents cavity optomechanics as a phase-sensitive amplifier [113, 114]. The amplifier has intrinsic quantum noise due to zero-point optical and mechanical fluctuations entering into the cavity. Furthermore, the amplifier can exhibit gain below unity in certain quadratures and frequency bands. This feature leads to a reduction of optical shot-noise below the level of Poissonian statistics [20, 105, 106], as shown in following sections.

A.2 Intracavity Response

The amplifier model developed above is applied here to study the response of the intracavity field to both optical and mechanical drives. Since the amplifier is linear, its susceptibility to each input type is completely decoupled, and we therefore treat the response to each input separately. In Section A.2.1, we consider the transduction of the optical field, and show that OMIT and ponderomotive squeezing both arise from the same physics. In Section A.2.2, we examine the transduction of mechanical inputs onto the optical field.

A.2.1 Response to Optical Inputs - Ponderomotive Attenuation and OMIT

The amplifier's response to optical inputs is characterized by the optical transfer matrix $\mathbf{H}_\alpha$, given in Eqs. A.12–A.15. This transfer matrix can be used to predict experimental outcomes. Here, we consider two types of experiments. In the first, modulation is applied to the pump (this applied modulation may be a coherent drive, classical noise, or quantum fluctuations), and the response of the optomechanical system is detected in the resulting amplitude or phase modulation of the optical field. Such experiments have demonstrated both ponderomotive squashing [103, 104] (attenuation of classical noise) and squeezing [102] (attenuation of quantum noise), as well as the transduction of coherent signals [102, 104]. In the second type of experiment, a weak probe at a single frequency accompanies the pump into the cavity and is detected, yielding observations of OMIT and optomechanically induced amplification [59, 60, 115, 116]. We show that both types of experiments are related via a simple unitary rotation of the transfer matrix.

The first type of experiment is characterized by the transduction of AM and PM from an optical input to the intracavity optical field. Because the static field a_0 is real, amplitude and phase modulation quadratures correspond identically to the $\hat{a}_\pm$
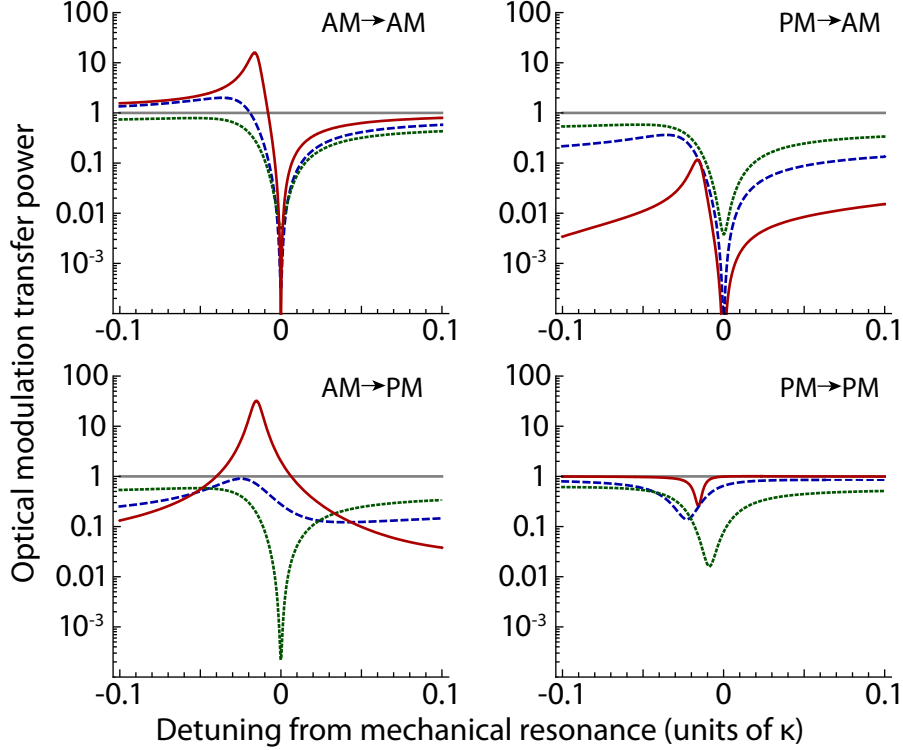
Figure A.2: Square magnitude of the elements of the optical modulation transfer matrix. The elements describe the transduction of amplitude and phase modulation from input to output. Powers are normalized by the total intracavity attenuation in the absence of optomechanics $(G = 0)$. Each element is plotted for the unresolved $(\omega_m/\kappa = 0.2$, solid red), intermediate $(\omega_m/\kappa = 1$, dashed blue), and resolved $(\omega_m/\kappa = 5$, dotted green) sideband cases, with the anti-Stokes mechanical sideband $(\Delta + \omega_m)$ fixed at $-0.5\ \kappa$ from cavity resonance. Ponderomotive attenuation is observed in the vicinity of $\omega = \omega_m$, while ponderomotive amplification is prevalent only for the unresolved sideband case, in the vicinity of $\omega = \omega_{\rm eff}$. For all plots, $D_{\rm opt} = 30$ and $Q = 1000$.

observables. However, because of the cavity phase rotation, the input field $\alpha_{\rm in,0}$ has a complex phase $\psi_c = \arctan(\Delta/\kappa)$, and the observables corresponding to AM and PM are

$$\begin{pmatrix} \hat{\tilde{\alpha}}_{\rm in,A} \\ \hat{\tilde{\alpha}}_{\rm in,P} \end{pmatrix} = \mathbf{R}(-\psi_c) \begin{pmatrix} \hat{\tilde{\alpha}}_{\rm in+} \\ \hat{\tilde{\alpha}}_{\rm in-} \end{pmatrix} \ , \tag{A.20}$$

where $\mathbf{R}$ is a rotation matrix defined as

$$\mathbf{R}(\theta) = \begin{pmatrix} \cos\theta & -\sin\theta \\ \sin\theta & \cos\theta \end{pmatrix} \ . \tag{A.21}$$
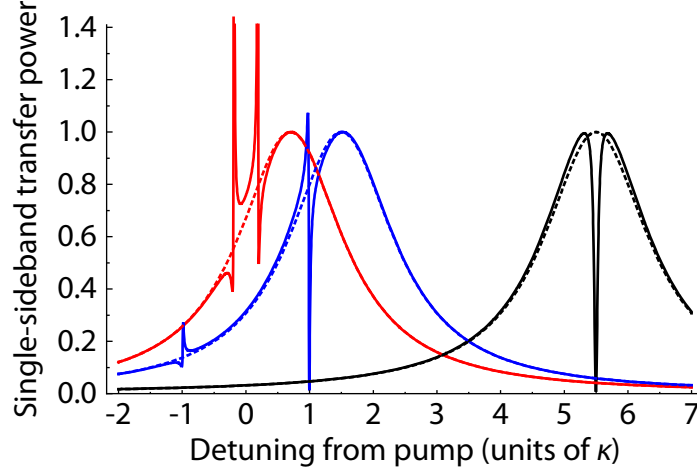
Figure A.3: Sum of the square magnitude of the $\hat{\tilde{\alpha}}(\omega) \to \hat{\tilde{a}}(\omega)$ term in the single-sideband spectral transfer matrix $\mathbf{H}_\alpha^{\mathrm{SS}}$. Probe frequencies ω are quoted in units of κ relative to the pump frequency at $\omega = 0$. Three cases are considered: unresolved ($\omega_m/\kappa = 0.2$, red), intermediate ($\omega_m/\kappa = 1$, blue) and resolved ($\omega_m/\kappa = 5$, black) sideband regimes, with the anti-Stokes mechanical sideband ($\Delta + \omega_m$) fixed at $-0.5\,\kappa$ from cavity resonance for the first two cases, and fixed on cavity resonance for the resolved sideband case. Solid lines indicate responses in the presence of an oscillator, while dashed lines apply to empty cavities. No normalization is performed (1 represents unity gain). For all plots, $D_{\mathrm{opt}} = 30$ and $Q = 1000$.

The input-output relation is thus given by the modulation transfer matrix $\mathbf{H}_\alpha^{\mathrm{MT}}$ as

$$\begin{pmatrix} \hat{\tilde{a}}_+ \\ \hat{\tilde{a}}_- \end{pmatrix} = \mathbf{H}_\alpha \mathbf{R}(\psi_c) \sqrt{\gamma_T} \begin{pmatrix} \hat{\tilde{\alpha}}_{\mathrm{in},A} \\ \hat{\tilde{\alpha}}_{\mathrm{in},P} \end{pmatrix} , \tag{A.22}$$

$$= \mathbf{H}_\alpha^{\mathrm{MT}} \sqrt{\gamma_T} \begin{pmatrix} \hat{\tilde{\alpha}}_{\mathrm{in},A} \\ \hat{\tilde{\alpha}}_{\mathrm{in},P} \end{pmatrix} .$$

Fig. A.2 shows the power (square magnitude) of each element of $\mathbf{H}_\alpha^{\mathrm{MT}}$. For a pump beam detuned to the red of cavity resonance, one sees an attenuation of modulation in the vicinity of $\omega = \omega_m$ in the output AM spectra, caused by the destructive interference of the input fluctuations with the mechanically transduced fluctuations. When the system is driven by optical shot noise, this attenuation gives ponderomotive squeezing of the optical field (see Section A.4.1). In the unresolved sideband case ($\omega_m \ll \kappa$), one also observes amplification of transduced AM near $\omega = \omega_{\mathrm{eff}} < \omega_m$ due to constructive feedback. As ω_m is increased above κ, the optomechanical damping in the vicinity of ω_{eff} increases, broadening and attenuating the amplified peak.

For the second experiment, we calculate the transduction of a single-tone probe $\hat{\tilde{\alpha}}(\omega)$. The single-sideband transfer matrix relates the input and output of pure tones

at $\pm\omega$:

$$\begin{pmatrix} \hat{\tilde{a}}(\omega) \\ \hat{\tilde{a}}^\dagger(-\omega) \end{pmatrix} = \mathbf{H}_\alpha^{\mathrm{SS}} \sqrt{\gamma_T} \begin{pmatrix} \hat{\tilde{\alpha}}(\omega) \\ \hat{\tilde{\alpha}}^\dagger(-\omega) \end{pmatrix} \ , \tag{A.23}$$

$$\mathbf{H}_\alpha^{\mathrm{SS}} = \mathbf{U}\mathbf{H}_\alpha\mathbf{U}^{-1} \ , \qquad\qquad \mathbf{U} = \frac{1}{\sqrt{2}} \begin{pmatrix} 1 & -i \\ 1 & i \end{pmatrix} \ .$$

Fig. A.3 shows the sum of the square magnitude of the $\mathbf{H}_\alpha^{\mathrm{SS}}$ terms that link the pure tone input $\hat{\tilde{\alpha}}(\omega)$ to the corresponding intracavity field $\hat{\tilde{a}}(\omega)$. It reflects the total intensity transduced in this single optical sideband (*i.e.* quadrature-insensitive detection). In the resolved-sideband limit, with the pump anti-Stokes mechanical sideband centered on the cavity resonance ($\omega_m = -\Delta$), a prominent dip at ω_m is visible. This feature is the hallmark of OMIT [59, 60].

This resolved-sideband probe spectrum changes when transitioning to the unresolved-sideband limit and detuning the pump anti-Stokes sideband from cavity resonance ($\omega_m < -\Delta$), with increased amplification at the effective oscillation frequency ω_{eff} and decreased attenuation at ω_m.

Our linear feedback model reveals clearly that ponderomotive attenuation and OMIT originate from the same physical phenomenon. Moreover, the model highlights that OMIT can be reinterpreted as a classical analog of ponderomotive squeezing, in that it demonstrates that certain matrix elements of the optical-to-optical transfer matrix have magnitude well below unity.

A.2.2 Response to Mechanical Inputs

Next, the transduction of mechanical inputs onto the circulating light field is studied. Fig. A.4 shows the power in each element of the mechanical to optical transduction matrix $\mathbf{H}_\eta$, multiplied by the input phonon coupling Γ_m. Expressed in this manner, the matrix elements give the optomechanical conversion of flux of phonon quanta into quanta of optical modulation. Transduction of η_- into PM follows a Breit-Wigner function, with response peaked at the effective oscillation frequency ω_{eff}. The AM response to η_- is scaled by $\Delta/(\kappa - i\omega)$ relative to that of PM, and the transduction of η_+ into AM/PM carries an additional factor of $(i\omega - \Gamma_m/2)/\omega_m$ relative to η_-.

A.3 Post-Cavity Detection

We now extend the model developed in section A.1 to consider the cavity output field. Photons exiting the cavity through the right and left mirrors form the new outputs of the optomechanical amplifier.
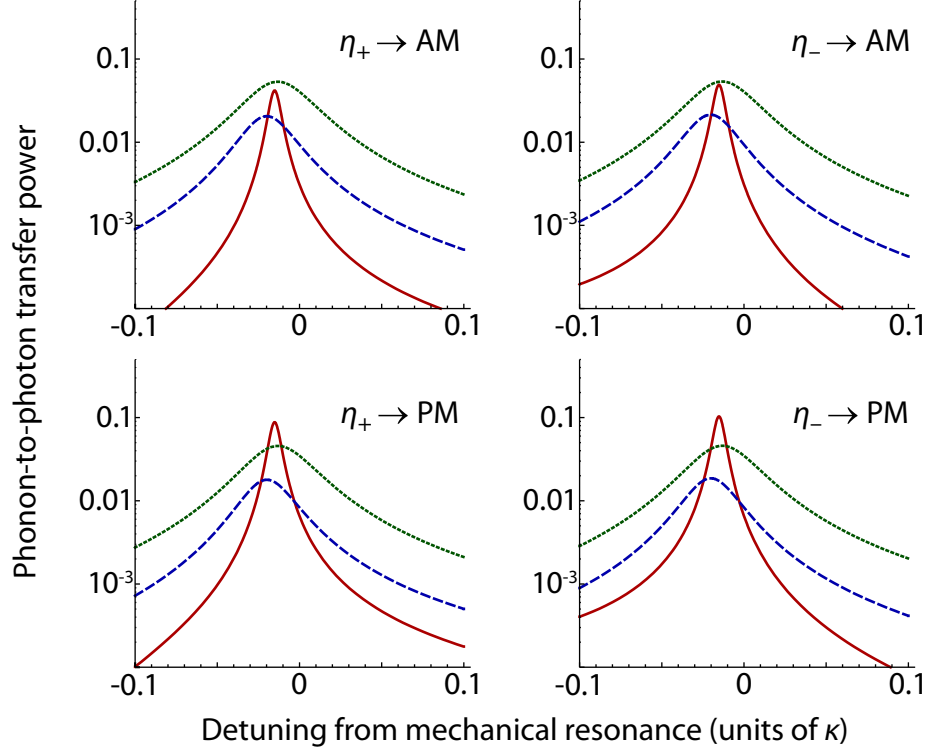
Figure A.4: Square magnitude of elements of the mechanical $\to$ optical modulation transduction matrix $\sqrt{\Gamma_m}\mathbf{H}_\eta$. The ordinate axis is in units of square modulation quanta of the intracavity field $\hat{a}$ per square flux quanta of the mechanical input field $\hat{\eta}$. Each element is plotted for the unresolved ($\omega_m/\kappa = 0.2$, solid red), intermediate ($\omega_m/\kappa = 1$, dashed blue), and resolved ($\omega_m/\kappa = 5$, dotted green) sideband cases, with the anti-Stokes mechanical sideband ($\Delta + \omega_m$) fixed at $-0.5\,\kappa$ from cavity resonance. For all plots, $D_{\text{opt}} = 30$ and $Q = 1000$.

Transfer functions connecting optical and mechanical inputs to the optomechanically colored cavity output light follow from Eq. A.11 according to cavity boundary conditions [117]. For any of the ports $l = L$, R, or V, the boundary condition is

$$\hat{\alpha}_{\text{in},l} + \hat{\alpha}_{\text{out},l} = \sqrt{\gamma_l}\,\hat{a}. \tag{A.24}$$

The boundary condition leads to expressions for the transfer matrix connecting any input $\hat{\alpha}_{\text{in},k}$ (where $k = L$, R, V, or η) to light in output field $\hat{\alpha}_{\text{out},j}$ (where $j = L$ or R):

$$\mathbf{H}_{j\,k}\underset{j \neq k}{=} \sqrt{\gamma_j \gamma_k}\,\mathbf{H}_k, \qquad\qquad \mathbf{H}_{j\,j} = \gamma_j \mathbf{H}_\alpha - \mathbf{1}, \tag{A.25}$$

where $\mathbf{H}_k = \mathbf{H}_\alpha$ or $\mathbf{H}_\eta$ for $k = L, R, V$ or η, respectively, and $\mathbf{1}$ is the identity matrix.

An optical signal measured in reflection thus includes beats between the exiting intracavity field and the reflected input beam. In contrast, both the optical signals from transmitted light and from the mechanical input are determined by scaling the intracavity field (see Section A.2). Both amplifier output ports can consequently carry distinct signatures of a common optomechanical interaction.

Let us apply these results to determine the output field response in reflection to applied pump modulations. As noted in Section A.2.1, the entering and exiting fields carry separate complex phases relative to the static intracavity field a_0 due to cavity rotation. Both phase angles are linked by the cavity boundary condition. For a one-sided, lossless cavity, the phase angles differ by $\phi_c = -\arctan\left(2\kappa\Delta/\left(\kappa^2 - \Delta^2\right)\right)$. Input AM and PM at port j are transduced into observable AM and PM at the output of that same port according to

$$\begin{pmatrix} \hat{\tilde{\alpha}}_{\text{out},jA} \\ \hat{\tilde{\alpha}}_{\text{out},jP} \end{pmatrix} = \mathbf{H}_{jj}^{\text{MT}} \begin{pmatrix} \hat{\tilde{\alpha}}_{\text{in},jA} \\ \hat{\tilde{\alpha}}_{\text{in},jP} \end{pmatrix} , \tag{A.26}$$

$$\mathbf{H}_{jj}^{\text{MT}} = \mathbf{R}(-\psi_c)\mathbf{R}(-\phi_c)\mathbf{H}_{jj}\mathbf{R}(\psi_c) .$$

Fig. A.5 shows the power (magnitude square) of each element of $\mathbf{H}_{jj}^{\text{MT}}$ for a one-sided, lossless cavity. The results are considerably different from those measured in transmission or intracavity (see Fig. A.2). The differences are due to the combined effect of cavity-induced phase rotation of the exiting intracavity field and its interference with light reflecting off the input/output mirror.

A.4   Specific input conditions

We now turn to the optomechanical amplifier response to specific inputs: quantum fluctuations of the mechanical and optical fields, a thermal mechanical bath, and external forces.

To characterize the response, we determine the power spectral density (PSD) of an output field quadrature $\hat{X}_{\theta j}$. The quadrature is defined by:

$$\hat{X}_{\theta j} \equiv \hat{\alpha}_{\text{out},j+} \cos\theta + \hat{\alpha}_{\text{out},j-} \sin\theta . \tag{A.27}$$

The PSD is defined as

$$S_{\theta j}(\omega) \equiv \left\langle \left| \hat{\tilde{X}}_{\theta j} \right|^2 \right\rangle \tag{A.28}$$

$$= \left\langle \left| \sum_k \begin{pmatrix} \cos\theta & \sin\theta \end{pmatrix} \mathbf{H}_{jk} \begin{pmatrix} \hat{\tilde{\zeta}}_{\text{in},+} \\ \hat{\tilde{\zeta}}_{\text{in},-} \end{pmatrix} \right|^2 \right\rangle ,$$

where $\zeta = \alpha$ or η for $k = L, R, V$ or η, respectively. If the inputs are incoherent, such that $\langle \hat{\tilde{\zeta}}_{\text{in}1}^\dagger \hat{\tilde{\zeta}}_{\text{in}2} \rangle = 0$ along two distinct input ports k_1 and k_2, the PSD can be rewritten
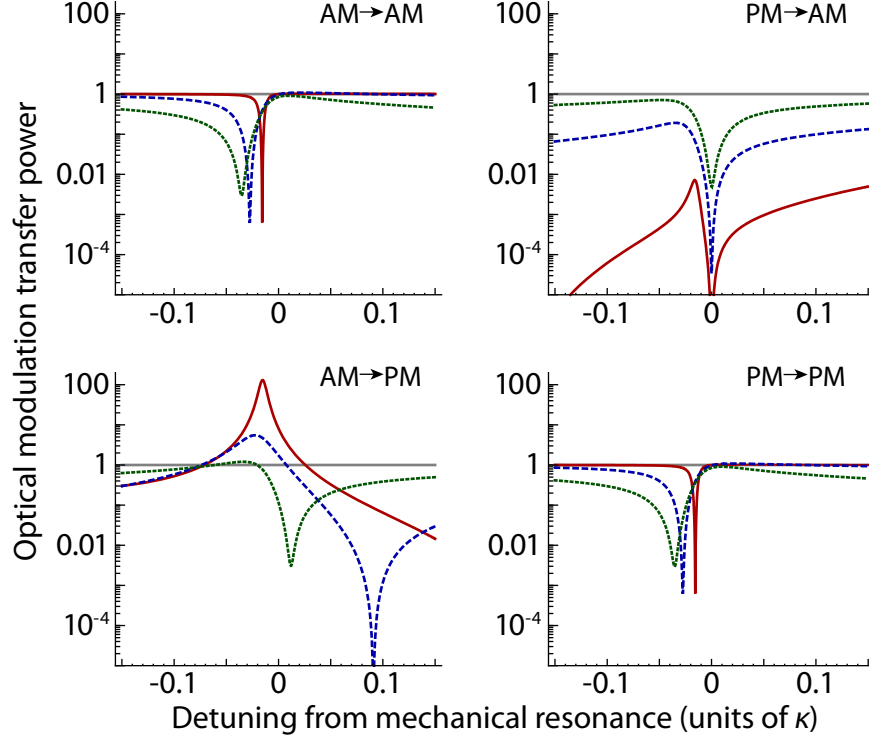
Figure A.5: Square magnitude of the elements of $\mathbf{H}_{jj}^{\mathrm{MT}}$, the optical modulation matrix connecting inputs and outputs in reflection. The elements describe the transduction of amplitude and phase modulation. Each element is plotted for the unresolved ($\omega_m/\kappa = 0.2$, solid red), intermediate ($\omega_m/\kappa = 1$, dashed blue), and resolved ($\omega_m/\kappa = 5$, dotted green) sideband cases, with the anti-Stokes mechanical sideband ($\Delta + \omega_m$) fixed at $-0.5\,\kappa$ from cavity resonance. For all plots, $D_{\mathrm{opt}} = 30$ and $Q = 1000$.

as a sum of transduced powers:

$$S_{\theta j}(\omega) = \sum_k \left\langle \left| \begin{pmatrix} \cos\theta & \sin\theta \end{pmatrix} \mathbf{H}_{jk} \begin{pmatrix} \hat{\tilde{\zeta}}_{\mathrm{in},+} \\ \hat{\tilde{\zeta}}_{\mathrm{in},-} \end{pmatrix} \right|^2 \right\rangle \tag{A.29}$$

(assuming incoherent inputs) .

Finally, the PSD of a real observable (*e.g.* X_θ) is necessarily symmetric in frequency, so we quote the symmetrized PSD

$$S_{\theta j,S}(\omega) \equiv \frac{1}{2}\left(S_{\theta j}(\omega) + S_{\theta j}(-\omega)\right) . \tag{A.30}$$

A.4.1 Optical and Mechanical Vacuum Fluctuations

Applying quantum perturbations to drive the oscillator allows the quantum nature of optomechanics to be probed. We study the case of quantum drives here by consid-
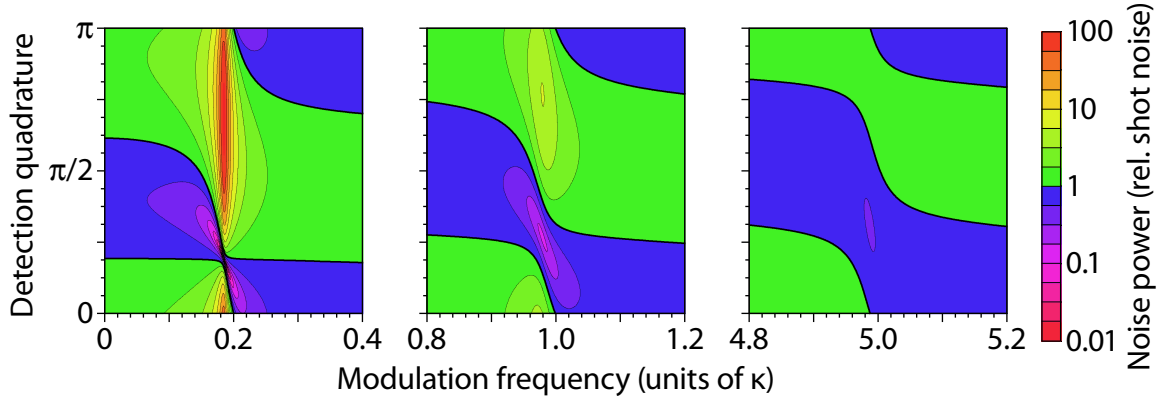
Figure A.6: Ponderomotive amplification and squeezing. Each panel shows the noise power (relative to shot-noise) of the optical field vs. frequency and quadrature for a one-sided lossless cavity. Quadrature angles refer to θ in Eq. A.27 ($\theta = 0, \pi/2$ correspond to $+,-$ quadrature, respectively). Columns show, respectively, the unresolved ($\omega_m/\kappa = 0.2$), intermediate ($\omega_m/\kappa = 1$), and resolved ($\omega_m/\kappa = 5$) sideband cases, with the anti-Stokes mechanical sideband ($\Delta + \omega_m$) fixed at $-0.5\,\kappa$ from cavity resonance. For all plots, $D_{\text{opt}} = 30$ and $Q = 1000$.

ering a shot-noise-limited pump input, where the cavity noise spectrum is dominated by optical and mechanical vacuum fluctuations. Under such a premise, optomechanical interactions imprint these zero-point fluctuations on the circulating light field with gain. Regions where the resulting fluctuations drop below the standard quantum limit (SQL) yield quadrature-squeezed light, *i.e.* ponderomotive squeezing [20]. Such squeezing is particularly important for gravitational-wave detectors, such as LIGO, where squeezed light sources provide enhanced detection sensitivity [12, 118]. Ponderomotive squeezing serves as an in-situ means to produce squeezed light at low frequencies, where detectors are sensitive to gravitational-wave perturbations [119]. A first experimental observation of ponderomotive squeezing has recently been reported [102].

We start with the noise spectrum of light reflected from a one-sided lossless cavity ($\gamma_R = 2\kappa$, $\gamma_L = \gamma_V = 0$). The general expression for the symmetrized PSD relative to shot-noise in this ideal case is

$$\bar{S}_{\theta R,S}^{\text{ideal}}(\omega) = \sum_{k=R,\eta} \left\| \begin{pmatrix} \cos\theta & \sin\theta \end{pmatrix} \mathbf{H}_{Rk} \right\|^2 . \tag{A.31}$$

The overbar on $\bar{S}_{\theta R,S}^{\text{ideal}}$ specifies that the symmetrized PSD is normalized by shot-noise and is therefore dimensionless. In addition, $\| \ldots \|^2$ represents the vector inner product.

$\bar{S}_{\theta R,S}^{\text{ideal}}$ is shown in Fig. A.6 for the case of sideband cooling ($\Delta < 0$). With the anti-Stokes mechanical sideband ($\Delta + \omega_m$) held fixed at $-0.5\,\kappa$, ponderomotive squeezing

is found to be largest near the $\theta = \pi/4$ quadrature at frequencies around ω_{eff}. For each sideband regime, the maximum squeezing quadrature and frequency are set by the competition of optomechanically squeezed vacuum inside the cavity and uncorrelated vacuum reflecting off the transmissive mirror. The suppression of quantum noise below the SQL results from the oscillator responding out of phase to vacuum perturbations above its effective mechanical resonance ω_{eff}. Quantum optical fluctuations are also mechanically transduced between uncorrelated conjugate quadratures (*e.g.* AM $\leftrightarrow$ PM). This leads to shot-noise amplification at all frequencies in the conjugate quadrature to that of maximum squeezing (near $\theta = 3\pi/4$ in Fig. A.6).

For a two-sided or lossy cavity, shot noise reflecting off the output port adds incoherently with vacuum fluctuations entering the cavity from other input ports. In addition, loss channels replace colored vacuum exiting the cavity with uncorrelated vacuum. Defining the relative photon extraction efficiency through the output port as ε_{out} ($\gamma_R = 2\kappa\,\varepsilon_{\text{out}}$, $\gamma_L + \gamma_V = 2\kappa\,(1 - \varepsilon_{\text{out}})$), and expressing the fraction of cavity output field detected as ε_{det}, one finds that the detected spectrum of noise relative to shot-noise is [117]

$$\bar{S}^{\text{obs}}_{\theta R, S}(\omega) = \varepsilon_{\text{tot}} \bar{S}^{\text{ideal}}_{\theta R, S}(\omega) + 1 - \varepsilon_{\text{tot}} \ , \tag{A.32}$$

where $\varepsilon_{\text{tot}} = \varepsilon_{\text{out}} \cdot \varepsilon_{\text{det}}$. If measurements are to be made on only one output port, any departure from the ideal one-sided case therefore results in a reduction of observable squeezing.

A.4.2 Mechanical Drive

Several noise models for mechanical disturbances have been proposed [120, 121, 122]. As done in earlier works [20, 105], here we study the Caldeira-Leggett model [122] under the Markov approximation, where

$$\langle \hat{\eta}^{\dagger}_{\text{in}}(t)\hat{\eta}_{\text{in}}(t') \rangle = n_{\text{th}}\delta(t - t') \ , \tag{A.33}$$

and Γ_m is constant across frequencies. The term $n_{\text{th}} = [e^{\hbar\omega_m/(k_{\text{B}}T)} - 1]^{-1}$ corresponds to the mean phonon number, determined by the mechanical bath temperature T. This model is appropriate for oscillators with high mechanical quality factor $Q = \omega_m/\Gamma_m$. Under this model, the total output noise due to mechanical fluctuations relative to mechanical shot-noise is

$$S^{\text{mech}}_{\pm R, S} = \frac{2\varepsilon_{\text{tot}}}{C_{\text{opt}}f_{\text{BW}}} \frac{\omega_m^2 + \omega^2}{\omega_m^2}(2n_{\text{th}} + 1)|H_{\pm\alpha}|^2, \tag{A.34}$$

where f_{BW} is the Fourier-transform bandwidth.

The drive source may also be an external force acting on the oscillator (*e.g.* a weak force that one wishes to detect via optomechanics). Since forces impart a change in momentum, a coherent force acting on the oscillator $\tilde{F}_{\text{ext}} = F_{\text{ext}}/f_{\text{BW}}$ is only related
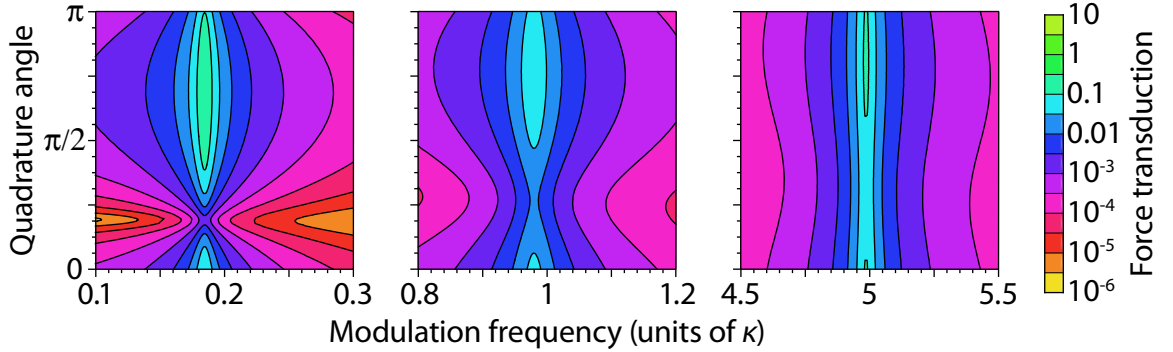
Figure A.7: External force sensitivity. Figure shows the optical power spectrum from external force transduction normalized by the drive power vs. frequency and quadrature. Quadrature angles refer to θ in Eq. A.27 ($\theta = 0, \pi/2$ correspond to $+,-$ quadrature, respectively). Columns show, respectively, the unresolved ($\omega_m/\kappa = 0.2$), intermediate ($\omega_m/\kappa = 1$), and resolved ($\omega_m/\kappa = 5$) sideband cases, with the anti-Stokes mechanical sideband ($\Delta + \omega_m$) fixed at $-0.5\,\kappa$ from cavity resonance. For all plots, $D_{\text{opt}} = 30$ and $Q = 1000$.

to the quadrature input term $\hat{\tilde{\eta}}_{\text{in}-}$ as

$$\sqrt{\Gamma_m} \left\langle \hat{\tilde{\eta}}_{\text{in}-} \right\rangle = \frac{\tilde{F}_{\text{ext}}}{p_{\text{ho}}} \ . \tag{A.35}$$

The term $p_{\text{ho}} = \sqrt{\hbar M \omega_m/2}$ symbolizes the harmonic oscillator momentum of the mechanical resonator, where M is the resonator's mass.

The push provided by $\tilde{F}_{\text{ext}}$ is imprinted on the optical pump field via the mechanically-applied phase shift (see Fig. A.1): optical sidebands at the drive frequencies are promoted. The optical power spectrum on the cavity output field arising from an external force, in units of square optical quanta per square force quanta, is given by

$$\frac{S_{\theta R,S}^{\text{ext}}}{|F_{\text{ext}}|^2} = \frac{2\varepsilon_{\text{tot}}}{C_{\text{opt}}} \left| \cos\theta + \frac{\kappa - i\omega}{\Delta} \sin\theta \right|^2 \frac{|G|^2}{\Gamma_m f_{\text{BW}}^2 p_{\text{HO}}^2} \tag{A.36}$$

Fig. A.7 shows that the force transduction is peaked at the same frequency ($\omega = \omega_{\text{eff}}$) and quadrature (near $\theta = 3\pi/4$ when $\Delta + \omega_m$ is fixed at $-0.5\,\kappa$) as that of maximum shot-noise amplification (see Section A.4.1). The maximization of force detection signal and quantum noise at the same point in parameter space motivates the question of optimal force sensing quadrature and condition.

Temperature and force sensing have standard quantum limits (SQL) set by two competing optomechanical effects: the transduction of external forces onto the light field and the optomechanical gain of zero-point fluctuations. SQLs for the canonical experiment of detection at $\Delta = 0$, $\omega = \omega_m$, $\theta = \pi/2$ and $\varepsilon_{\text{tot}} = 1$ have previously
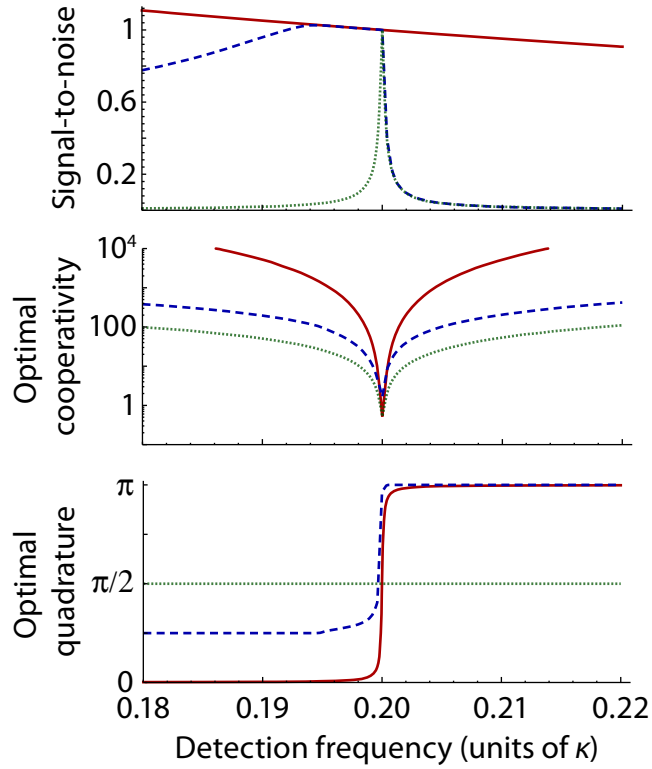
Figure A.8: Optimal force sensing with and without ponderomotive squeezing. The top panel shows the prefactor for the optimal signal-to-noise (relative to that of Eq. A.37) vs. force frequency, the middle panel shows C_{opt} necessary to obtain optimal force sensing, and the bottom panel shows the necessary quadrature angle. Each plot shows the case without squeezing ($\Delta = 0$, solid red line) and with squeezing ($\Delta = -\kappa$, dashed blue line). The optimal signal-to-noise ratio for the canonical force detection experiment at $\Delta = 0$ and $\theta = \pi/2$ is included for reference (*i.e.* extension of Eqs. A.37–A.38 over all frequencies, dotted green line). For all plots, $\omega_m/\kappa = 0.2$ and $Q = 1000$.

been derived [113, 123]. The quantum limit on signal-to-noise ratio (SNR) for external force detection is reached when the cooperativity is tuned such that the noise arising from backaction (transduction of optical noise along the $\theta = 0$ quadrature) is equal in magnitude to optomechanically colored optical shot noise along the $\theta = \pi/2$ quadrature. Rederived using the linear amplifier model, the SNRs for sensing of thermal motion and sensing of coherent external forces under these conditions are given

as

$$R_{\text{SQL}}^{\text{therm}} = \left(1 + \frac{3}{64}\frac{1}{Q^2} + \mathcal{O}(Q^{-4})\right) n_{\text{th}} \ , \tag{A.37}$$

$$R_{\text{SQL}}^{\text{ext}} = \left(\frac{1}{4} - \frac{5}{256}\frac{1}{Q^2} + \mathcal{O}(Q^{-4})\right) \frac{F_{\text{ext}}^2}{\Gamma_m f_{\text{BW}} p_{\text{HO}}^2} , \tag{}$$

obtained using an optomechanical cooperativity of

$$C_{\text{opt}}^{\text{SQL}} = \frac{1}{2}\left(1 + \frac{\omega_m^2}{\kappa^2}\right) + \mathcal{O}(Q^{-2}). \tag{A.38}$$

An adapted form of Eqs. A.37–A.38 is shown in Fig. A.8.

We now extend this work to consider force detection at frequencies away from the mechanical resonance. The maximum SNR attainable in this case is given by

$$R_{\text{max}}^{\text{ext}} = \frac{1}{(\frac{1}{2Q})^2 + \left(1 + \left|\frac{\omega}{\omega_m}\right|\right)^2} \frac{F_{\text{ext}}^2}{\Gamma_m f_{\text{BW}} p_{\text{HO}}^2} \ , \tag{A.39}$$

using the quadrature angle and optomechanical cooperativity

$$\theta^{\text{max}} = \arctan\left(\frac{\frac{1}{Q}\left|\frac{\omega}{\omega_m}\right|}{(\frac{1}{2Q})^2 + \left(1 - \frac{\omega^2}{\omega_m^2}\right)}\right) \tag{A.40}$$

$$C_{\text{opt}}^{\text{max}} = \frac{(1 + \frac{\omega^2}{\kappa^2})\left|\omega_m^2 + \Gamma_m^2/4 - \omega^2 - i\,\Gamma_m\omega\right|^2}{2\,\Gamma_m^2\omega_m\left|\omega\right|} ,$$

These optimal solutions are shown in Fig. A.8. Results indicate that the optimal cooperativity quickly diverges to experimentally unrealistic values as the measurement frequency shifts away from mechanical resonance. In addition, we point out that these optimal solutions are extremely fragile to optical losses; $R_{\text{max}}^{\text{ext}}$ is significantly reduced at frequencies away from ω_m for $\varepsilon_{\text{tot}} \lesssim 1$.

Can we improve on the force transduction SNR by detuning off cavity resonance and benefitting from ponderomotive squeezing [124, 125, 126]? We provide an answer to this question by applying a numerical optimization routine to identify $C_{\text{opt}}^{\text{max}}$, θ^{max} and $R_{\text{max}}^{\text{ext}}$ for $\omega_m/\kappa = 0.2$ (unresolved sideband case) and various pump detunings Δ, ranging from $-0.5\,\kappa$ to $-6\,\kappa$. The results under $\omega_m/\kappa = 0.2$ and $\Delta/\kappa = -1$ are shown in Fig. A.8. When comparing the signal to the total noise in the reflected optical field, we find that squeezing and detuning off cavity resonance *do not* increase the signal-to-noise ratio above the maximum SNR found for $\Delta = 0$. However, results also indicate that there is a range of frequencies ($\omega \lesssim \omega_m$) for which the optimal level of force sensitivity is attainable off cavity resonance with realistic cooperativities.

A.5 Conclusion

We have shown that linearized optomechanical systems can be modeled as linear optical amplifiers with mechanical and optical inputs. In this new context, ponderomotive squeezing, an entirely quantum effect, and OMIT are shown to be related: the latter is a classical manifestation of the former. The optomechanical amplifier model was extended to predict observable power spectra in cavity output field under different drives. Our work indicates that ponderomotive squeezing is most visible in the unresolved-sideband limit. It also highlights that optical squeezing cannot be harnessed to surpass the maximum SNR for external force measurements on cavity resonance.

The amplifier model offers a simple picture of optomechanical systems with insights into the sources of gain and lines of communication between the mechanical and optical degrees of freedom. As research in the field continues to diversify, we hope it may serve as a tool to model different setups under a common language and bridge separate concepts.

Bibliography

[1] Peter Lebedew. Untersuchungen über die Druckkräfte des Lichtes. *Annalen der Physik*, 311(11):433–458, 1901.

[2] E. F. Nichols and G. F. Hull. A Preliminary Communication on the Pressure of Heat and Light Radiation. *Phys. Rev. (Series I)*, 13:307–320, 1901.

[3] V.B. Braginskii and A.B. Manukin. Ponderomotive Effects of Electromagnetic Radiation. *Soviet Physics JETP*, 25:653, 1967.

[4] V.B. Braginsky, A.B. Manukin, and M.Yu. Tikhonov. Investigation of dissipative ponderomotive effects of electromagnetic radiation. *Soviet Physics JETP*, 31:829, 1970.

[5] Rainer Weiss. Electromagetically Coupled Broadband Gravitational Antenna. *Quarterly Progress Report, Research Laboratory of Electronics, MIT*, 105:54, 1972.

[6] Vladimir B Braginski and Yurii I Vorontsov. Quantum-mechanical limitations in macroscopic experiments and modern experimental technique. *Soviet Physics Uspekhi*, 17:644–650, 1975.

[7] R. P. Giffard. Ultimate sensitivity limit of a resonant gravitational wave antenna using a linear motion detector. *Phys. Rev. D*, 14:2478–2486, 1976.

[8] Kip S. Thorne, Ronald W. P. Drever, Carlton M. Caves, Mark Zimmermann, and Vernon D. Sandberg. Quantum Nondemolition Measurements of Harmonic Oscillators. *Phys. Rev. Lett.*, 40:667–671, 1978.

[9] Vladimir B. Braginsky, Yuri I. Vorontsov, and Kip S. Thorne. Quantum Nondemolition Measurements. *Science*, 209(4456):547–557, 1980.

[10] W. G. Unruh. Quantum nondemolition and gravity-wave detection. *Phys. Rev. D*, 19(10):2888–2896, May 1979.

[11] Carlton M. Caves, Kip S. Thorne, Ronald W. P. Drever, Vernon D. Sandberg, and Mark Zimmermann. On the measurement of a weak classical force coupled

to a quantum-mechanical oscillator. I. Issues of principle. *Rev. Mod. Phys.*, 52:341–392, 1980.

[12] Carlton M. Caves. Quantum-mechanical noise in an interferometer. *Phys. Rev. D*, 23(8):1693–1708, 1981.

[13] J. Weber. Observation of the Thermal Fluctuations of a Gravitational-Wave Detector. *Phys. Rev. Lett.*, 17:1228–1230, 1966.

[14] A. Dorsel, J. D. McCullen, P. Meystre, E. Vignes, and H. Walther. Optical Bistability and Mirror Confinement Induced by Radiation Pressure. *Phys. Rev. Lett.*, 51:1550–1553, 1983.

[15] William D. Phillips and Harold Metcalf. Laser Deceleration of an Atomic Beam. *Phys. Rev. Lett.*, 48:596–599, 1982.

[16] Steven Chu, J. E. Bjorkholm, A. Ashkin, and A. Cable. Experimental Observation of Optically Trapped Atoms. *Phys. Rev. Lett.*, 57:314–317, 1986.

[17] Paul D. Lett, Richard N. Watts, Christoph I. Westbrook, William D. Phillips, Phillip L. Gould, and Harold J. Metcalf. Observation of Atoms Laser Cooled below the Doppler Limit. *Phys. Rev. Lett.*, 61:169–172, 1988.

[18] G. Binnig, C. F. Quate, and Ch. Gerber. Atomic Force Microscope. *Phys. Rev. Lett.*, 56:930–933, 1986.

[19] P. F. Cohadon, A. Heidmann, and M. Pinard. Cooling of a Mirror by Radiation Pressure. *Phys. Rev. Lett.*, 83(16):3174–3177, 1999.

[20] C. Fabre, M. Pinard, S. Bourzeix, A. Heidmann, E. Giacobino, and S. Reynaud. Quantum-noise reduction using a cavity with a movable mirror. *Phys. Rev. A*, 49(2):1337–1343, 1994.

[21] D. K. Armani, T. J. Kippenberg, S. M. Spillane, and K. J. Vahala. Ultra-high-Q toroid microcavity on a chip. *Nature*, 421(6926):925–928, 2003.

[22] T. J. Kippenberg, H. Rokhsari, T. Carmon, A. Scherer, and K. J. Vahala. Analysis of Radiation-Pressure Induced Mechanical Oscillation of an Optical Microcavity. *Phys. Rev. Lett.*, 95(3):033901, 2005.

[23] Robert G. Knobel and Andrew N. Cleland. Nanometre-scale displacement sensing using a single electron transistor. *Nature*, 424:291–293, 2003.

[24] M. D. LaHaye, O. Buu, B. Camarota, and K. C. Schwab. Approaching the Quantum Limit of a Nanomechanical Resonator. *Science*, 304:74–77, 2004.

[25] O. Arcizet, P.-F. Cohadon, T. Briant, M. Pinard, and A. Heidmann. Radiation-pressure cooling and optomechanical instability of a micromirror. *Nature*, 444:71–74, 2006.

[26] S. Gigan, H. R. Bohm, M. Paternostro, F. Blaser, G. Langer, J. B. Hertzberg, K. C. Schwab, D. Bauerle, M. Aspelmeyer, and A. Zeilinger. Self-cooling of a micromirror by radiation pressure. *Nature*, 444:67–70, 2006.

[27] A. Schliesser, P. Del'Haye, N. Nooshi, K. J. Vahala, and T. J. Kippenberg. Radiation Pressure Cooling of a Micromechanical Oscillator Using Dynamical Backaction. *Phys. Rev. Lett.*, 97(24):243905, 2006.

[28] Subhadeep Gupta, Kevin L. Moore, Kater W. Murch, and Dan M. Stamper-Kurn. Cavity Nonlinear Optics at Low Photon Numbers from Collective Atomic Motion. *Physical Review Letters*, 99(21):213601, 2007.

[29] Ferdinand Brennecke, Stephan Ritter, Tobias Donner, and Tilman Esslinger. Cavity Optomechanics with a Bose-Einstein Condensate. *Science*, 322(5899):235–238, 2008.

[30] K.W. Murch, K.L. Moore, S. Gupta, and D.M. Stamper-Kurn. Observation of quantum-measurement backaction with an ultracold atomic gas. *Nature Physics*, 4:561–564, 2008.

[31] G. Anetsberger, O. Arcizet, Q. P. Unterreithmeier, R. Rivire, A. Schliesser, E. M. Weig, J. P. Kotthaus, and T. J. Kippenberg. Near-field cavity optomechanics with nanomechanical oscillators. *Nature Physics*, 5:909–914, 2009.

[32] J. D. Teufel, T. Donner, M. A. Castellanos-Beltran, J. W. Harlow, and K. W. Lehnert. Nanomechanical motion measured with an imprecision below that at the standard quantum limit. *Nat Nano*, 4(12):820–823, 2009.

[33] Xiaoshun Jiang, Qiang Lin, Jessie Rosenberg, Kerry Vahala, and Oskar Painter. High-Q double-disk microcavities for cavity optomechanics. *Opt. Express*, 17(23):20911–20919, 2009.

[34] A. D. OConnell, M. Hofheinz, M. Ansmann, Radoslaw C. Bialczak, M. Lenander, Erik Lucero, M. Neeley, D. Sank, H. Wang, M. Weides, J. Wenner, John M. Martinis, and A. N. Cleland. Quantum ground state and single-phonon control of a mechanical resonator. *Nature*, 464:697–703, 2010.

[35] J. D. Teufel, T. Donner, Dale Li, J. W. Harlow, M. S. Allman, K. Cicak, A. J. Sirois, J. D. Whittaker, K. W. Lehnert, and R. W. Simmonds. Sideband cooling of micromechanical motion to the quantum ground state. *Nature*, 475:359, 2011.

[36] Jasper Chan, T. P. Mayer Alegre, Amir H. Safavi-Naeini, Jeff T. Hill, Alex Krause, Simon Groblacher, Markus Aspelmeyer, and Oskar Painter. Laser cooling of a nanomechanical oscillator into its quantum ground state. *Nature*, 478(7367):89–92, 2011.

[37] Daniel W. C. Brooks, Thierry Botter, Sydney Schreppler, Thomas P. Purdy, Nathan Brahms, and Dan M. Stamper-Kurn. Non-classical light generated by quantum-noise-driven cavity optomechanics. *Nature*, 488(7412):476–480, 2012.

[38] Nathan Brahms, Thierry Botter, Sydney Schreppler, Daniel W. C. Brooks, and Dan M. Stamper-Kurn. Optical Detection of the Quantization of Collective Atomic Motion. *Phys. Rev. Lett.*, 108:133601, 2012.

[39] Thierry Botter, Daniel W. C. Brooks, Sydney Schreppler, Nathan Brahms, and Dan M. Stamper-Kurn. Optical read-out of the quantum motion of an array of atoms-based mechanical oscillators. arXiv:1210.5218.

[40] Thierry Botter, Daniel W. C. Brooks, Nathan Brahms, Sydney Schreppler, and Dan M. Stamper-Kurn. Linear amplifier model for optomechanical systems. *Phys. Rev. A*, 85:013812, Jan 2012.

[41] E.T. Jaynes and F.W. Cummings. Comparison of quantum and semiclassical radiation theories with application to the beam maser. *Proceedings of the IEEE*, 51(1):89–109, 1963.

[42] Michael Tavis and Frederick W. Cummings. Exact Solution for an N-Molecule¯Radiation-Field Hamiltonian. *Phys. Rev.*, 170:379–384, 1968.

[43] Christopher Gerry and Peter Knight. *Introductory Quantum Optics*. Cambridge University Press, 2004.

[44] Marlan O. Scully and M. Suhail Zubairy. *Quantum Optics*. Cambridge University Press, 1997.

[45] D.F. Walls and Gerard J. Milburn. *Quantum Optics*. Springer, 2010.

[46] Serge Haroche and Jean-Michel Raimond. *Exploring the Quantum: Atoms, Cavities, and Photons*. Oxford University Press, 2006.

[47] Rodney Loudon. *The Quantum Theory of Light*. Oxford University Press, 2000.

[48] Sergio M. Dutra. *Cavity Quantum Electrodynamics: The Strange Theory of Light in a Box*. Wiley-Interscience, 2004.

[49] Kater W. Murch. *Cavity Quantum Optomechanics with Ultracold Atoms*. PhD thesis, University of California, Berkeley, 2008.

[50] Thomas P. Purdy. *Cavity QED with Ultracold Atoms on an Atom Chip.* PhD thesis, University of California, Berkeley, 2009.

[51] Monika H. Schleier-Smith, Ian D. Leroux, Hao Zhang, Mackenzie A. Van Camp, and Vladan Vuletić. Optomechanical Cavity Cooling of an Atomic Ensemble. *Phys. Rev. Lett.*, 107:143005, 2011.

[52] Dan M. Stamper-Kurn. Cavity optomechanics with cold atoms. arxiv.org/abs/1204.4351, 2012.

[53] C. J. Foot. *Atomic Physics.* Oxford University Press, 2005.

[54] T. P. Purdy, D. W. C. Brooks, T. Botter, N. Brahms, Z.-Y. Ma, and D. M. Stamper-Kurn. Tunable Cavity Optomechanics with Ultracold Atoms. *Phys. Rev. Lett.*, 105(13):133602, 2010.

[55] J. C. Sankey, C. Yang, B. M. Zwickl, A. M. Jayich, and J. G. E. Harris. Strong and Tunable Nonlinear Optomechanical Coupling in a Low-Loss System. *Nature Physics*, 6:707–712, 2010.

[56] C. J. Hood, T. W. Lynn, A. C. Doherty, A. S. Parkins, and H. J. Kimble. The Atom-Cavity Microscope: Single Atoms Bound in Orbit by Single Photons. *Science*, 287:1447–1453, 2000.

[57] P. W. H. Pinkse, T. Fischer, P. Maunz, and G. Rempe. Trapping an atom with single photons. *Nature*, 404:365–368, 2000.

[58] T. Fischer, P. Maunz, P. W. H. Pinkse, T. Puppe, and G. Rempe. Feedback on the Motion of a Single Atom in an Optical Cavity. *Phys. Rev. Lett.*, 88:163002, 2002.

[59] A. H. Safavi-Naeini, T. P. Mayer Alegre, J. Chan, M. Eichenfield, M. Winger, Q. Lin, J. T. Hill, D. E. Chang, and O. Painter. Electromagnetically induced transparency and slow light with optomechanics. *Nature*, 472:69, 2011.

[60] Stefan Weis, Rmi Rivire, Samuel Delglise, Emanuel Gavartin, Olivier Arcizet, Albert Schliesser, and Tobias J. Kippenberg. Optomechanically Induced Transparency. *Science*, 330:1520–1523, 2010.

[61] Roy J. Glauber. The Quantum Theory of Optical Coherence. *Phys. Rev.*, 130:2529–2539, 1963.

[62] L. Mandel and E. Wolf. *Optical coherence and quantum optics.* Cambridge University Press, 1995.

[63] Mark Fox. *Quantum Optics: An Introduction.* Oxford University Press, 2006.

[64] Roy Glauber. *Quantum Theory of Optical Coherence.* Wiley-VCH, 2007.

[65] Hannes Risken. *The Fokker-Planck Equation: Methods of Solutions and Applications.* Springer, 1996.

[66] Anthony E. Siegman. *Lasers.* University Science Books, 1986.

[67] Christina J. Hood, H. J. Kimble, and Jun Ye. Characterization of high-finesse mirrors: Loss, phase shifts, and mode structure in an optical cavity. *Phys. Rev. A*, 64:033804, Aug 2001.

[68] Toptica Photonics. *Tunable Diode Lasers.*

[69] L. Ricci, M. Weidemller, T. Esslinger, A. Hemmerich, C. Zimmermann, V. Vuletic, W. Knig, and T.W. Hnsch. A compact grating-stabilized diode laser system for atomic physics. *Optics Communications*, 117(56):541 – 549, 1995.

[70] Eric D. Black. An introduction to Pound–Drever–Hall laser frequency stabilization. *American Journal of Physics*, 69(1):79–87, 2001.

[71] A. Ashkin and J. M. Dziedzic. Optical Trapping and Manipulation of Viruses and Bacteria. *Science*, 235:1517–1520, 1987.

[72] A. Ashkin, J. M. Dziedzic, and T. Yamane. Optical trapping and manipulation of single cells using infrared laser beams. *Nature*, 330(6150):769–771, 1987.

[73] Steven M. Block, David F. Blair, and Howard C. Berg. Compliance of bacterial flagella measured with optical tweezers. *Nature*, 338(6215):514–518, 1989.

[74] J. McKeever, J. R. Buck, A. D. Boozer, A. Kuzmich, H.-C. Nägerl, D. M. Stamper-Kurn, and H. J. Kimble. State-Insensitive Cooling and Trapping of Single Atoms in an Optical Cavity. *Phys. Rev. Lett.*, 90:133602, 2003.

[75] Peter van der Straten Harold J. Metcalf. *Laser Cooling and Trapping.* Springer, 1999.

[76] Claude Cohen-Tannoudji and David Guery-Odelin. *Advances in Atomic Physics: An Overview.* World Scientifc Publishing Corp., 2011.

[77] Rudolf Grimm, Matthias Weidemuller, and Yurii B. Ovchinnikov. *Optical Dipole Traps for Neutral Atoms*, volume 42 of *Advances In Atomic, Molecular, and Optical Physics.* Academic Press, 2000.

[78] Daniel A. Steck. Rubidium 87 D Line Data. Theoretical Division Los Alamos National Laboratory.

[79] D. Jaksch, C. Bruder, J. I. Cirac, C. W. Gardiner, and P. Zoller. Cold Bosonic Atoms in Optical Lattices. *Phys. Rev. Lett.*, 81:3108–3111, 1998.

[80] Dan Brooks. *Atomic cavity optomechanics: classical to quantum regime.* PhD thesis, Berkeley, 2013.

[81] Igor Bargatin and M. L. Roukes. Nanomechanical Analog of a Laser: Amplification of Mechanical Oscillations by Stimulated Zeeman Transitions. *Phys. Rev. Lett.*, 91:138302, 2003.

[82] Ivan S. Grudinin, Hansuek Lee, O. Painter, and Kerry J. Vahala. Phonon Laser Action in a Tunable Two-Level System. *Phys. Rev. Lett.*, 104:083901, 2010.

[83] Qiang Lin, Jessie Rosenberg, Darrick Chang, Ryan Camacho, Matt Eichenfield, Kerry J. Vahala, and Oskar Painter. Coherent mixing of mechanical excitations in nano-optomechanical structures. *Nature Photonics*, 4:236–242, 2010.

[84] Mian Zhang, Gustavo Wiederhecker, Sasikanth Manipatruni, Arthur Barnard, Paul L. McEuen, and Michal Lipson. Synchronization of Micromechanical Oscillators Using Light. arXiv:1112.3636, 2011.

[85] Francesco Massel, Sung Un Cho, Juha-Matti Pirkkalainen, Pertti J. Hakonen, Tero T. Heikkilä, and Mika A. Sillanpää. Multimode circuit optomechanics near the quantum limit. *Nat Commun*, 3:987, 2012.

[86] Quirin P. Unterreithmeier, Thomas Faust, and Jörg P. Kotthaus. Damping of Nanomechanical Resonators. *Phys. Rev. Lett.*, 105:027205, 2010.

[87] Garrett D. Cole, Ignacio Wilson-Rae, Katharina Werbach, Michael R. Vanner, and Markus Aspelmeyer. Phonon-tunnelling dissipation in mechanical resonators. *Nat Commun*, 2:231, 2011.

[88] V Bouchiat, D Vion, P Joyez, D Esteve, and M H Devoret. Quantum coherence with a single Cooper pair. *Physica Scripta*, 1998:165, 1998.

[89] T.J. Kippenberg and K.J. Vahala. Cavity Opto-Mechanics. *Optics Express*, 15(25):17172, 2007.

[90] T. J. Kippenberg and K. J. Vahala. Cavity Optomechanics: Back-Action at the Mesoscale. *Science*, 321:1172–1176, 2008.

[91] G. Anetsberger, E. Gavartin, O. Arcizet, Q. P. Unterreithmeier, E. M. Weig, M. L. Gorodetsky, J. P. Kotthaus, and T. J. Kippenberg. Measuring nanomechanical motion with an imprecision below the standard quantum limit. *Phys. Rev. A*, 82:061804, Dec 2010.

[92] M. Eichenfield, R. Camacho, J. Chan, K. J. Vahala, and O. Painter. A picogram- and nanometer-scale photonic crystal opto-mechanical cavity. *Nature*, 459:550, 2009.

[93] J. Hofer, A. Schliesser, and T. J. Kippenberg. Cavity optomechanics with ultrahigh-Q crystalline microresonators. *Phys. Rev. A*, 82(3):031804, 2010.

[94] D. J. Wilson, C. A. Regal, S. B. Papp, and H. J. Kimble. Cavity Optomechanics with Stoichiometric SiN Films. *Phys. Rev. Lett.*, 103(20):207204, 2009.

[95] Thomas Corbitt, Yanbei Chen, Edith Innerhofer, Helge Müller-Ebhardt, David Ottaway, Henning Rehbein, Daniel Sigg, Stanley Whitcomb, Christopher Wipf, and Nergis Mavalvala. An All-Optical Trap for a Gram-Scale Mirror. *Phys. Rev. Lett.*, 98(15):150802, 2007.

[96] Thomas Corbitt, David Ottaway, Edith Innerhofer, Jason Pelc, and Nergis Mavalvala. Measurement of radiation-pressure-induced optomechanical dynamics in a suspended Fabry-Perot cavity. *Phys. Rev. A*, 74(2):021802, 2006.

[97] Florian Elste, S. M. Girvin, and A. A. Clerk. Quantum Noise Interference and Backaction Cooling in Cavity Nanomechanics. *Phys. Rev. Lett.*, 102(20):207209, 2009.

[98] Florian Marquardt, Joe P. Chen, A. A. Clerk, and S. M. Girvin. Quantum Theory of Cavity-Assisted Sideband Cooling of Mechanical Motion. *Phys. Rev. Lett.*, 99(9):093902, 2007.

[99] Max Ludwig, Bjrn Kubala, and Florian Marquardt. The optomechanical insta- bility in the quantum regime. *New Journal of Physics*, 10:095013, 2008.

[100] J. B. Hertzberg, T. Rocheleau, T. Ndukum, M. Savva, A. A. Clerk, and K. C. Schwab. Back-action-evading measurements of nanomechanical motion. *Nature Physics*, 6:213–217, 2010.

[101] Benjamin S. Sheard, Malcolm B. Gray, Conor M. Mow-Lowry, David E. Mc- Clelland, and Stanley E. Whitcomb. Observation and characterization of an optical spring. *Phys. Rev. A*, 69(5):051801, 2004.

[102] D. W. C. Brooks, T. Botter, N. Brahms, T. P. Purdy, S. Schreppler, and D. M. Stamper-Kurn. Observation of Ponderomotive Squeezing. arXiv:1107.5609, 2011.

[103] Francesco Marino, Francesco S. Cataliotti, Alessandro Farsi, Mario Siciliani de Cumis, and Francesco Marin. Classical Signature of Ponderomotive Squeez- ing in a Suspended Mirror Resonator. *Phys. Rev. Lett.*, 104(7):073601, 2010.

[104] P. Verlot, A. Tavernarakis, T. Briant, P.-F. Cohadon, and A. Heidmann. Back-action Amplification and Quantum Limits in Optomechanical Measurements. *Phys. Rev. Lett.*, 104(13):133602, 2010.

[105] K. Bjorkje, A. Nunnenkamp, B. M. Zwickl, C. Yang, J. G. E. Harris, and S. M. Girvin. Observability of radiation-pressure shot noise in optomechanical systems. *Phys. Rev. A*, 82(1):013818, 2010.

[106] A. Heidmann, Y. Hadjar, and M. Pinard. Quantum nondemolition measurement by optomechanical coupling. *Applied Physics B: Lasers and Optics*, 64:173–180, 1997.

[107] J. D. Teufel, Dale Li, M. S. Allman, K. Cicak, A. J. Sirois, J. D. Whittaker, and R. W. Simmonds. Circuit cavity electromechanics in the strong-coupling regime. *Nature*, 471:204–208, 2010.

[108] J. D. Thompson, B. M. Zwickl, A. M. Jayich, Florian Marquardt, S. M. Girvin, and J. G. E. Harris. Strong dispersive coupling of a high finesse cavity to a micromechanical membrane. *Nature*, 452:72–75, 2008.

[109] Mankei Tsang and Carlton M. Caves. Coherent Quantum-Noise Cancellation for Optomechanical Sensors. *Phys. Rev. Lett.*, 105(12):123601, 2010.

[110] Stefano Mancini, David Vitali, and Paolo Tombesi. Optomechanical Cooling of a Macroscopic Oscillator by Homodyne Feedback. *Phys. Rev. Lett.*, 80(4):688–691, 1998.

[111] Florian Marquardt, J. G. E. Harris, and S. M. Girvin. Dynamical Multistability Induced by Radiation Pressure in High-Finesse Micromechanical Optical Cavities. *Phys. Rev. Lett.*, 96(10):103901, 2006.

[112] V. B. Braginsky, S. E. Strigin, and S. P. Vyatchanin. Analysis of parametric oscillatory instability in power recycled LIGO interferometer. *Physics Letters A*, 305(3-4):111 – 124, 2002.

[113] Carlton M. Caves. Quantum limits on noise in linear amplifiers. *Phys. Rev. D*, 26(8):1817–1839, 1982.

[114] H. A. Haus and J. A. Mullen. Quantum Noise in Linear Amplifiers. *Phys. Rev.*, 128(5):2407–2413, 1962.

[115] Sumei Huang and G. S. Agarwal. Electromagnetically induced transparency with quantized fields in optocavity mechanics. *Phys. Rev. A*, 83(4):043826, 2011.

[116] Sumei Huang and G. S. Agarwal. Electromagnetically induced transparency from two-phonon processes in quadratically coupled membranes. *Phys. Rev. A*, 83(2):023823, 2011.

[117] D.F. Walls and G.J. Milburn. *Quantum Optics*. Springer, 1995.

[118] Jan Harms, Yanbei Chen, Simon Chelkowski, Alexander Franzen, Henning Vahlbruch, Karsten Danzmann, and Roman Schnabel. Squeezed-input, optical-spring, signal-recycled gravitational-wave detectors. *Phys. Rev. D*, 68(4):042001, 2003.

[119] Thomas Corbitt, Yanbei Chen, Farid Khalili, David Ottaway, Sergey Vyatchanin, Stan Whitcomb, and Nergis Mavalvala. Squeezed-state source using radiation-pressure-induced rigidity. *Phys. Rev. A*, 73(2):023801, 2006.

[120] I. Wilson-Rae. Intrinsic dissipation in nanomechanical resonators due to phonon tunneling. *Phys. Rev. B*, 77(24):245418, 2008.

[121] B. L. Hu, Juan Pablo Paz, and Yuhong Zhang. Quantum Brownian motion in a general environment: Exact master equation with nonlocal dissipation and colored noise. *Phys. Rev. D*, 45(8):2843–2861, 1992.

[122] A. O. Caldeira and A. J. Leggett. Quantum tunnelling in a dissipative system. *Annals of Physics*, 149(2):374 – 456, 1983.

[123] A. A. Clerk, M. H. Devoret, S. M. Girvin, Florian Marquardt, and R. J. Schoelkopf. Introduction to quantum noise, measurement, and amplification. *Rev. Mod. Phys.*, 82(2):1155–1208, 2010.

[124] Thomas Corbitt and Nergis Mavalvala. Review: Quantum noise in gravitational-wave interferometers. *Journal of Optics B: Quantum and Semiclassical Optics*, 6(8):S675–S683, 2004.

[125] H. J. Kimble, Yuri Levin, Andrey B. Matsko, Kip S. Thorne, and Sergey P. Vyatchanin. Conversion of conventional gravitational-wave interferometers into quantum nondemolition interferometers by modifying their input and/or output optics. *Phys. Rev. D*, 65(2):022002, 2001.

[126] O. Arcizet, T. Briant, A. Heidmann, and M. Pinard. Beating quantum limits in an optomechanical sensor by cavity detuning. *Phys. Rev. A*, 73(3):033819, 2006.